RESILIENT MONITORING AND ROBUST CONTROL TOWARDS BLACKOUT

PREVENTION IN MODERN POWER GRIDS

A Dissertation
Submitted to the Graduate Faculty
of the
North Dakota State University
of Agriculture and Applied Science

By

Abhishek Banerjee

In Partial Fulfillment of the Requirements
for the Degree of
DOCTOR OF PHILOSOPHY

Major Department:
Electrical and Computer Engineering

February 2020

Fargo, North Dakota

NORTH DAKOTA STATE UNIVERSITY

Graduate School

Title

RESILIENT MONITORING AND ROBUST CONTROL TOWARDS

BLACKOUT PREVENTION IN MODERN POWER GRIDS

By

Abhishek Banerjee

The supervisory committee certifies that this dissertation complies with North Dakota State University's regulations and meets the accepted standards for the degree of

DOCTOR OF PHILOSOPHY

SUPERVISORY COMMITTEE:

Dr. Rajesh Kavasseri

Chair

Dr. Nilanjan Ray Chaudhuri

Dr. Dong Cao

Dr. Majura Selekwa

Approved:

27 February 2020

Date

Dr. Benjamin D. Braaten

Department Chair

ABSTRACT

This dissertation embodies a comprehensive approach towards resilient monitoring of frid events using Structure Preserving Energy Functions (SPEFs) and introduces a novel control architecture in Multi Terminal Direct Current (MTDC) grids, for inter-area oscillation damping and achieving robustness to AC as well as DC side, post-contingency events in the modern power grid. This work is presented as a collection of several publications which investigate and address the proposed research topics.

At first, SPEFs are derived for multi-machine IEEE benchmark models with the help of the Wide-Area Measurements (WAMs). A physics-based hybrid approach to develop one-to-one mapping between properties of energy function components with respect to the type of fault in the system is introduced. The proposed method is tested offline on a IEEE-39 bus, New England Test System (NETS), with particular interest in monitoring the most sensitive energy functions during relay misoperations. Such events can be precipitated by zone 3 trips in distance relays due to load encroachment during stressed conditions. These might include a genuine misoperation, a false trip due to cyber-attacks, or a load encroachment, all of which are undesirable under normal operating circumstances. An online monitoring scheme is introduced in an actual blackout simulation in the Western Electricity Coordinating Council (WECC) to examine what further indications these energy function components can provide, especially during a cascading sequence, and how they could supervise critical tripping decisions by distance relays. Next, a futuristic grid comprised of Voltage Source Converter (VSC) based AC-MTDC is considered due to its recent proliferation in integrating offshore wind farms to onshore grids, and additionally improving strength of weak AC grids. A robust control is designed using the converter station poles as actuators to provide damping support to the surrounding AC grid. Further, a design problem is envisioned and implemented that introduces disturbance rejection into control architecture by designing a novel explicitly modeled disturbance plant in the Linear Matrix Inequality (LMI) framework. Finally, a novel robust inter-area oscillation damping controller is designed that proves its effectiveness in inter-area mode settling times, and provides robustness to (n-1) contingencies in the AC as well as the DC side of the meshed AC-MTDC grid.

ACKNOWLEDGEMENTS

First and foremost, I would like to thank almighty for the blessings, my parents, and brother for their encouragement and constant mental support all these years. It was not easy to be away from them, however, they have always encouraged me in rain and sunshine to achieve what I wanted in my career.

I would like to thank my advisor Dr. Rajesh Kavasseri for his patience, knowledge and wisdom to guide me through the last five years. For all the support I have received from him during my doctoral study, not just in terms of academic advising but also in personal interactions which has certainly transformed me into an individual researcher and a better human being. I thank him for all his patience, guidance, cutting-edge ideas on present state-of-art of power systems, and his very rigorous approach towards quality of work. It is worthwhile to mention a few courses taught by Dr. Kavasseri like Linear Systems Theory, Neural Networks and Power Systems Protection, which had very interesting content and helped me build a deep insight into current research topics in power systems resilience.

I would like to equally thank my co-advisor Dr. Nilanjan Ray Chaudhuri for accepting me as a graduate student under his patronage and helping me develop skills in advance control on inverter based resources. It would have not been possible for me to get a broader picture of the power and controls research world without his guidance. He was there for me on every occasion whenever I required any kind of assistance, and he has motivated me to better performer in all circumstances. His technological prowess combined with his strong hold on his subject areas always inspired me to follow his footsteps. I cannot have found a better supervisor than Dr. Chaudhuri in my doctoral life.

I would like to thank the following people for contributing to my success in the endeavors: Professors and fellow students at NDSU for creating a favorable academic environment and their kind support. I would want to thank the remaining members of the dissertation committee, Dr. Dong Cao, and Dr. Majura Selekwa for their valuable comments and suggestions on improving this work. Especially, Dr. Majura Selewka for his guidance on the topic of robust and advanced controls and for the extra-ordinary course that he offered during the spring of 2016. I would also like to

DEDICATION

This dissertation is dedicated to my parents who have supported me in all endeavors of my life and my late grandmother who provided me constant motivation, and always wished for me to usher as a successful scientist. I am sure wherever she is is today, she would be very proud of my achievements and keep blessing me.

TABLE OF CONTENTS

LIST OF TABLES

LIST OF FIGURES

LIST OF APPENDIX TABLES

LIST OF APPENDIX FIGURES

1. INTRODUCTION

The modern power grid is now more interconnected with new technologies comprising of thousands of individual components, making it increasingly complex in nature [1, 2, 3]. One of the major concerns that threaten the stable operation of a modern grid is a sequence of equipment outages, termed as cascading failure [4, 5]. A cascading failure is a sequence of outages to an initiating event or events [6]. These outages originate from strong inter-dependencies within the components of the grid and typically occur in rapid succession [7]. Cascading failures are normally caused by initiating events, such as an overloading on a weak part of the grid leading to relay misoperation, and through fast propagation, they can lead to the most severe large-scale blackouts in modern complex power systems [8, 9, 10, 11].

The Northeast blackout on November 9, 1965 led to the formation of the North American Electric Reliability Council (NERC) [12] in 1968 and power pools such as the New York Power Pool (NYPP) [13]. The obejctive was to develop industry standards for equipment testing and reserve generation capacity, as well as preventative measures governing interconnection and reliability, to prevent such failures. In the past decade, the US has experienced thousands of blackouts in many of the states, and has affected millions of people [14, 15]. The Northeast blackout of 2003, a wide-area power failure in the northeastern US and central Canada, affected an estimated 10 million people in Ontario and 45 million people in eight states in the USA, with 30 billion dollars of economic loss in this incident [6, 16]. In a recent blackout report by Eaton, the total number of outages experienced in the US in the year 2017 are shown in Fig. 1.1, and the total number of people affected that year was a staggering $36,179,833$ [17]. The statistics clearly indicate the severity of these events on the modern grids showing how frequent they have impacted the grid and the detrimental affects that have followed . Similar blackouts have been witnessed all over the world [18, 19, 20], including the 2012 power blackout in India [21], so far the biggest power failure in history affecting over 400 million people [22]. Ample research has evolved around understanding the dynamics of the grids during blackouts but most of them being conducted post blackout stages. Many studies have tried to model the dynamics of the failure based on the power system normal operations regime like optimal power flow algorithms, while others proposed stochastic formulations [23, 24] and data
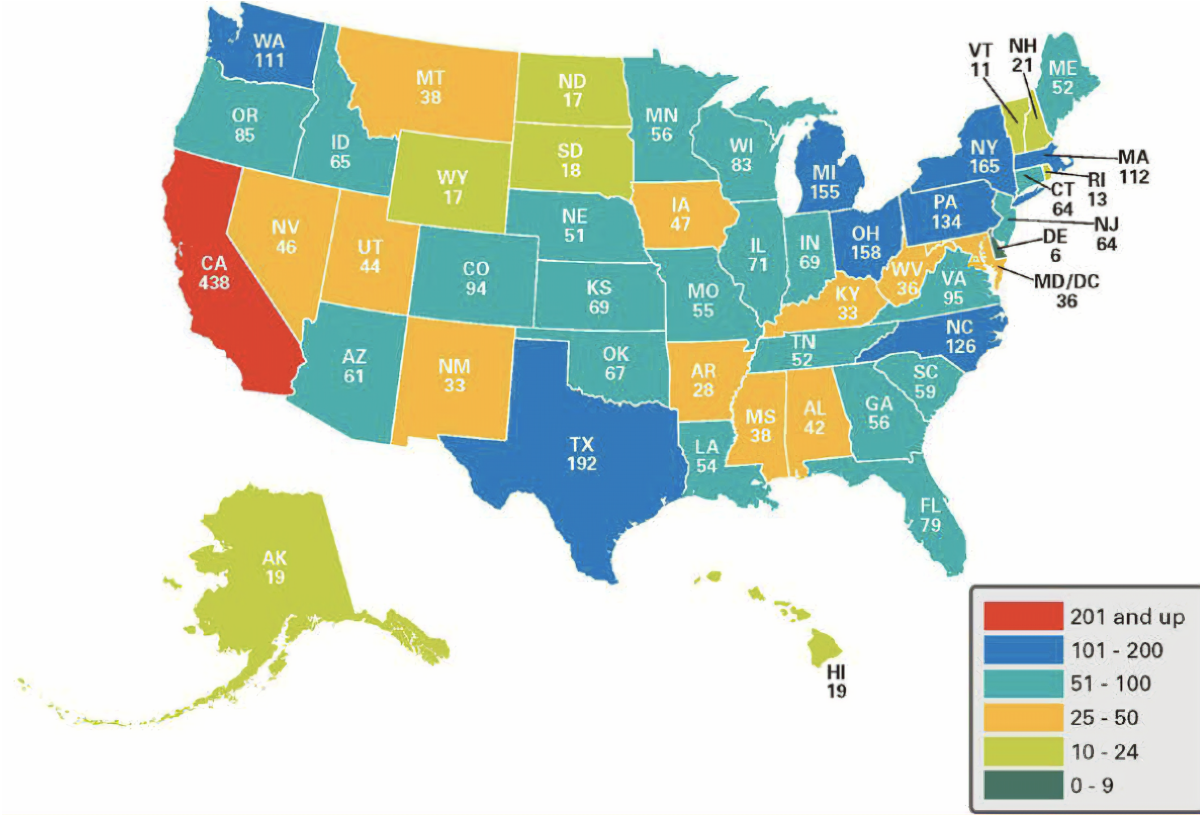
Figure 1.1. Number of reported power outages in US by state, in the year 2017, (credit: Eaton)
.

driven approaches [25, 26] to consider randomness in the evolution of the failures. In order to attack this problem in real-time it is very important to understand the dynamics of the grid pre, during, and post fault stages in a cascade. In recent literature, attempts have been made to link transient stability analysis with cascading failures [27, 28], with increased focus on sensitivity analysis of the power grids [29] towards cascading failures. With the proliferation of Phasor Measurement Units (PMU's) in the modern power grid, Wide Area Monitoring, Protection and Control (WAMPAC) has received much attention [30, 31, 32], enabling us to access the voltage and current phasors, frequency and its rate of change, and power flows at any point in time. To that context, with the help of the wide-area measurements from PMUs, coupled with state estimation to generate energy functions have shown promising aspects [33, 34]. Every component of the Structure Preserving Energy Functions (SPEFs) [35] in a multi-machine power system can be derived [33], providing complete knowledge of the system energy.

Thus, motivated, this dissertation addresses resilient monitoring of several events that might contribute to cascading failure by the use of a physics based -Structure Preserving Energy Function (SPEF) approach. A systematic approach to develop one-to-one mapping between properties of energy function components to the type of fault in the system is proposed. This renders the approach based on the physical properties and energies of the system - the most fundamental aspect of power engineering, thus eliminating tedious statistical analysis based approach for studying such events. Monitoring in real time is possible with the help of mapping sensitivities of the energy functions in the pre, during and post fault stages. Moreover, during heavy system loading conditions, relay misoperations are possible when load encroachments are misinterpreted as faults. This motivates us to examine what further indications these energy function components can provide, especially during stressed conditions, and how they may by used to supervise critical tripping decisions by distance relays. There are many additional causes for such initiating events in case of cascading failures like instabilities in the grid that include rotor angle, voltage and frequency instability. In power systems, frequency, voltage and rotor angle of synchronous generating units are most pivotal quantities and should be properly controlled in order to maintain the power system stability [36]. The triggering event for the 1996 WECC system blackout [37] in the US was angle instability in the rotors of SG's and voltage collapse that precipitated in the cascading sequence. The blackouts that happened all over the world have drawn considerable attention to study the cascading failure mechanism and investigate the robustness and vulnerability of power grids. In order to understand the mechanism of cascading failures in power systems, it is necessary to comprehend the rotor angle behavior as it is representative of the stability and synchronism in the whole power system [38, 39, 40]. This serves as motivation for the continuity of this dissertation where rotor angle instability problem faced as inter-area oscillations in AC power systems embedded in a Multi Terminal Direct Current (DC) grid has been addressed.

We have witnessed a re-evolving landscape of power systems in the recent decade, with increased penetration of renewable energy, resource adequacy and the increase modeling and development of Distributed Energy Resources (DERs). In future grids, the number of inverter-based devices could be more than 50% of the rated power at any time, thereby forming an inverter-dominated grid. Variable renewable energy (VRE), such as wind and solar photovoltaic (PV) systems, are being considered as major contributors, and with the reduction in costs for these tech-

U.S. energy consumption by energy source, 2018

total = 101.3 quadrillion British thermal units (Btu)

total = 11.5 quadrillion Btu

petroleum 36%

natural gas 31%

coal 13%

nuclear electric power 8%

renewable energy 11%

2% - geothermal
6% - solar
21% - wind
4% - biomass waste
21% - biofuels
biomasss 45%
19% - wood
25% - hydroelectric
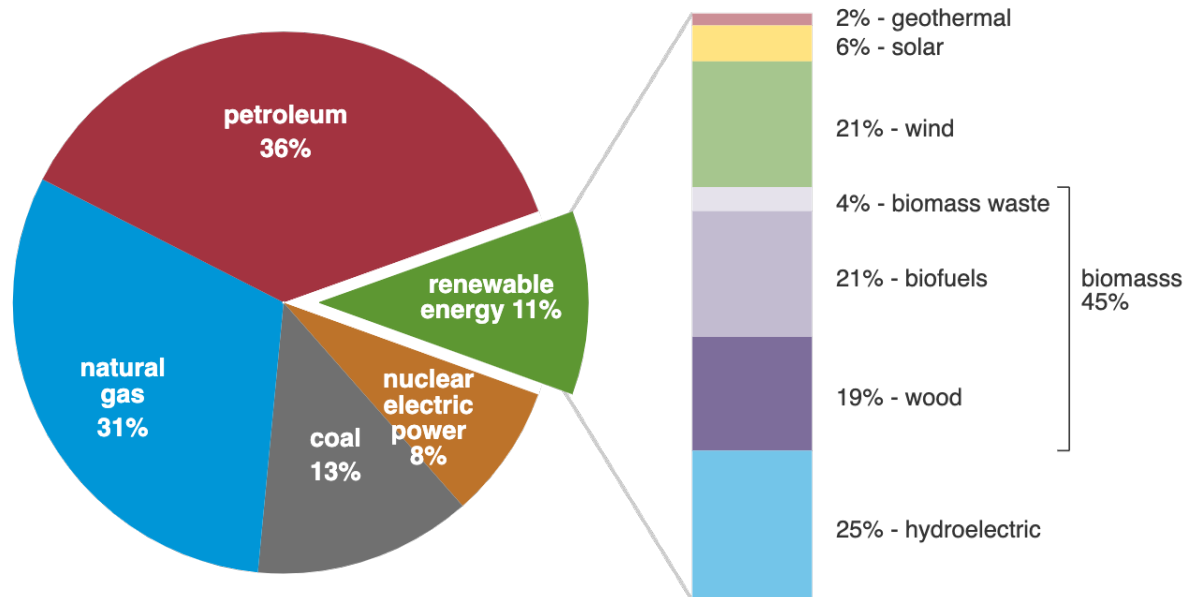
Note: Sum of components may not equal 100% because of independent rounding.
Source: U.S. Energy Information Administration, *Monthly Energy Review*, Table 1.3 and 10.1, April 2019, preliminary data

Figure 1.2. U.S. energy consumption by energy source, 2018 (credit: EIA).

nologies during the last decade, large-scale production and installations are happening around the world. According to the U.S. Department of Energy (DOE) report [41], there was a 1.4% growth in the the US offshore pipeline growth in 2018, increasing from $25,464$ MW to $25,824$ MW , where global offshore wind annual generating capacity installed in 2018 set a new record of $5,652$ MW. Figure 1.2 depicts the growing potential of wind energy by illustrating the energy consumption by energy sources, of which wind comprises of 21% of the total renewable energy produced. As per the report [42], most of these wind resources have been identified as offshore and onshore wind potential in the United States, see Fig. 1.3. However, most of the onshore wind is located in the mid-western regions of the United States and proper harnessing of this wind potential requires long haul transmission distances where High Voltage DC deems to be a better fit than High Voltage AC grids [43] due to several governing factors. Most of this wind potential can be harnessed either by Line Commutated Converter (LCC) technology - for onshore wind farms or by Voltage Source Converters (VSCs) for offshore wind farms connected to onshore grids. MTDC grids are meshed DC

4

U.S Potential Wind Capacity in Megawatts (MW) at 80 Meters
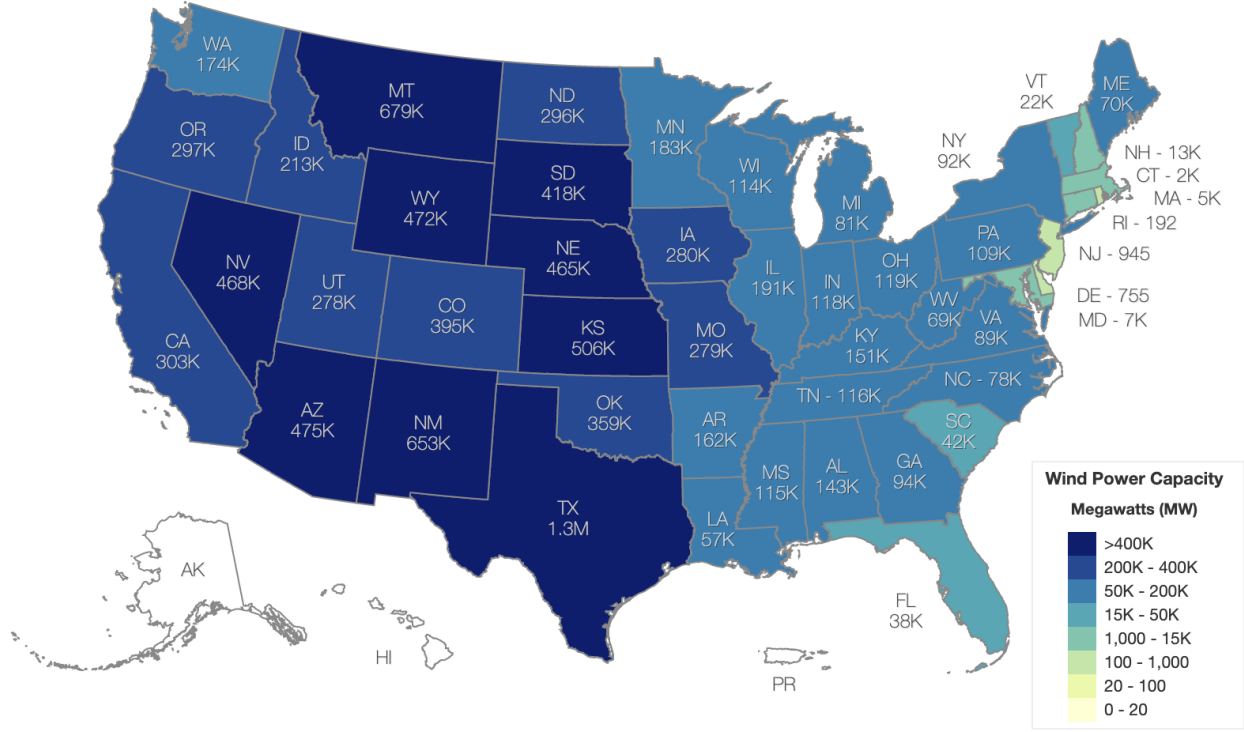
Total Potential Wind Capacity: 10,640,080 MW

Figure 1.3. U.S. onshore and offshore wind energy potential at 80m (credit: National Renewable Energy Laboratory).

grids that have significant advantages over point-to-point connected traditional High Voltage Direct Current (HVDC) grids; which include multiple corridors for power flow during the event of collapse in any one converter station. MTDC grids posses great potential in harnessing the VSC technology due to its ability of fast acting power modulation [44]. There has been a significant research in the recent years where VSCs have been deployed for its ability to provide additional support the grid. Increased penetration of renewable energy require complex power engineering modeling, analysis and control design for mixed AC-DC system level interactions [45, 46]. This calls for the need of newer abstractions for control architecture of power electronic interfaced traditional AC generation in the upcoming years, with a futuristic yet of 100% inverter dominated grids.

This next part of this dissertation is concerned with robust control design of hybrid inter-connected AC-MTDC power grids taking into consideration, the disturbances that could occur in such grids during a contingency, which in turn could affect system stability and introduce inter-area

oscillations. Modern power systems include more distributed generation and increased penetration and are prone to increased disturbance inputs due to cyber-physical processes that offer a wide range of operating conditions and uncertain behavior [47, 48]. For instance, the load demands at a certain bus can vary gradually, or even sharply, every hour throughout a day; disturbances of differing extents of severity could happen during the normal operation; and the topology of the system could change over time. The existence of disturbances and uncertainties in the modern grid require more details, and attention to newer control abstractions for attaining robustness in the control design. A robust control system is insensitive to differences between the actual system and the model of the reduced order system that was used to design the controller [49, 50, 51]. These differences are referred to as model/plant mismatch or simply as model uncertainty. In the present state of art of modern interconnected power systems, the robust control system [52] will have to regulate the system under diverse operating conditions; it must have the ability to tolerate perturbations, suppress potential instability in both AC as well as DC connected subsystems, and damp the modal oscillations that might threaten system stability when the system is operating under stressed conditions when interfaced to increased renewable energy integration. The concept of robust damping of inter-area oscillations using MTDC converter stations as actuators is relatively new at the time of writing the research articles.

This dissertation examines several fundamental questions:

- Can we develop resiliency in the grid using energy functions based on wide area monitoring by introducing newer algorithms ?

- If so, could these reduce the search space and decrease complexity than existing statistical approaches for monitoring power system behavior during stressed conditions ?

- On the other hand, can MTDC converter stations be used as actuators to develop a supplementary controller that is capable of ensuring damping support to the AC-MTDC interconnected grid?

- Can these controllers inherit properties of robustness to disturbances in both AC as well as DC sides that might perturb system stability ?

- If so, can the proposed controller be validated against other existing robust control design in terms of their dependability and improved performance measure?

This dissertation proposes and demonstrates a detailed wide area based resilient monitoring approach using the richly embedded system-wide information in the SPEFs of the individual components of the grid. SPEF based monitoring is implemented on both offline and online simulations to ascertain the most important energy function component that is indicative of zone 3 behavior of the distance relays, and could be used to model supervisory action for preventing cascading failures. It emphasizes on the dynamics of the grid due to rotor angle instability with increased penetration of renewable energy in future grids, and their uncertain behavior that could induce disturbances into the grid. A novel control architecture for developing robust supplementary controllers in AC-MTDC grid framework is proposed, which enhances damping performance of the inter-area oscillations, while increasing the measures of robustness towards AC as well as DC side contingencies - an aspect that has been less pondered upon in recent literature. Disturbance modeling aided control design has been implemented - replacing the trivial use of identity matrices for representing disturbance in robust control design formulation of power systems.

1.1. Fault Mapping in Multi-machine Power Systems by Principal Component Sensitivity -An Energy Function Perspective

This chapter envisages the mapping of particular faults associated with their real time occurring corresponding events in a large scale power system by exploring the underlying rich information embedded in their Structure Preserving Energy Function (SPEF) components. A sliding window algorithm based prediction is employed to continuously monitor the change in the SPEF components in pre-fault, during-fault and post-fault stages. A Stacked Potential Energy (SPE) matrix is introduced and subjected to Principal Component Sensitivity (PCS) using a singular value decomposition technique to discern the effect of events by analyzing the upper and lower dimensional sub-spaces. The effectiveness of the proposed sequence of classification can be observed from the results on a IEEE 4-machine, 2-area test system. A highly coherent and correlated response can be observed between different types of events and the corresponding mappings in the respective SPEFs. Highly correlated energy functions can be sought-after by pointing at different events which

7

may trigger some specific components of interconnected power systems at the time of unexpected events and changes in the system.

1.2. Towards Supervisory Protection Using Energy Functions for Relay Misoperations in a Stressed Power System During Blackout

Relay misoperations in power systems, especially during stressed conditions can initiate a cascade potentially leading towards a blackout. A typical event that aggravates a cascade is a trip decision by distance relays to faults in zone 3. We examine the use of energy functions as a discriminant in such scenarios to supervise the action of distance relays, in particular, to distinguish between load encroachment and zone 3 faults. The scenarios are tested on two individual test beds, the 39 bus New-England Test System (NETS) and a portion of the Western Electricity Coordinating Council (WECC) system. NETS is used to analyze and assess the choice of energy functions for protection, whereas the WECC system is used for an actual blackout simulation in the South Western United States corridor. Analysis on these test systems depict on how energy functions can help in detecting and potentially avert costly relay misoperations.

1.3. Robust Damping of Inter-area Oscillations in AC-MTDC Grids Using H_∞ Mixed-Sensitivity Approach

This chapter involves the novel systematic approach, underlying assumptions, derivations, and control formulations required to design a robust supplementary controller based on the Linear Matrix Inequality (LMI) framework for an integrated AC-MTDC grid. This controller will be responsible for damping inter-area oscillations following major contingencies like the outage of a converter pole and line outage. The damping controller, as shown in Fig. 1.4 employs the converter stations positive and negative poles as actuators. The design is based on H_∞ mixed-sensitivity formulation in the LMI framework. In addition to providing ancillary support, emphasis has been placed on achieving robustness in the design by incorporating proper weighing filters for disturbance rejection and control energy minimization; the two measures of mixed-sensitivity namely disturbance sensitivity and control sensitivity that are being addressed in the following contribution. Weight selection is very important in achieving the goals in robust control design and is carried out in the frequency domain using maximum and minimum singular value based sensitivity gain approach. The proposed controller uses feedback signals from remote locations and modulates the real power reference of two converter poles in a converter station of the asymmetric bipolar MTDC grid, which

8

Asymmetric Bipolar MTDC Converter Stations

AC GRID #1

AC GRID #2

*Output feedback signals
(power flows from AC grid)*

$y_1, y_2, ...y_m$

*Output feedback signals
(power flows from AC grid)*

$y_1, y_2, ...y_m$

MIMO
Supplementary
controller

K_∞

P^{p*}_{pcck}

Inner current control
loop of kth converter
station

Droop gain

β_k

$+$

P^p_{mod}

u_1, u_2

Control inputs

$-$

P^p_{pcck}

u_1, u_2

Control inputs

P^p_{mod}

$+$

P^{p*}_{pcck}

Droop gain

β_k

Inner current control
loop of kth converter
station

$-$

P^p_{pcck}

Outer Voltage Control loop of kth converter station

Outer Voltage Control loop of kth converter station

Figure 1.4. Supplementary damping controller with converter station poles as actuators.

is integrated with AC systems. The controller was tested on a 6-machine 3-area AC-MTDC test system and a 16-machine, 5-area AC-MTDC test system. Robustness in damping performance in case of converter outage and AC line outage was successfully achieved by the designed controllers in both the test systems.

1.4. A Novel Explicit Disturbance Model-based Robust Damping of Inter-Area Oscillations Through MTDC Grids Embedded in AC Systems

This paper presents a novel approach to damp inter-area oscillations by designing a robust multi-input multi-output (MIMO) supplementary controller for MTDC grids embedded in AC systems. The key idea to achieve robustness lies in explicitly modeling the MTDC current injection as disturbances, Fig. 1.5 using an $\mathcal{H}_\infty$ mixed-sensitivity formulation in the LMI framework.
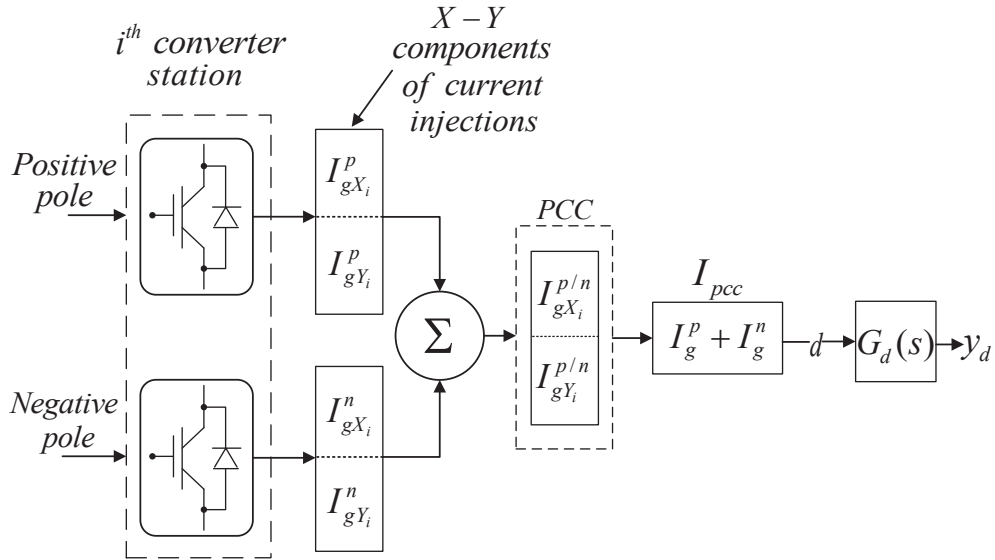
Figure 1.5. DC-side contingencies modeled as a disturbance plant $G_d(s)$ using current injections I_{pcc} as input and feedback signals y_d used for damping control as output.

Control directions are established by selecting wide-area feedback signals and the Relative Gain Array computation. Robustness is assessed through dynamic simulations for scenarios including: (a) disturbances on the AC side, (b) disturbances on the DC-side such as loss of a converter pole including actuator, (c) partial loss of feedback signal, and (d) communication latencies. The performance of the proposed controller is compared against the conventional $\mathcal{H}_\infty$ based design, using a

4-terminal DC grid embedded within the New England-New York test system. The results suggest that the proposed approach demonstrates superior performance following DC-side disturbances, actuator outages, and latency.

1.5. Dissertation Organization

This dissertation is organized as follows: the background for wide area resilient monitoring and the concept of fault mapping using energy function based approach, considering detailed models for synchronous generators in a multi-machine setting are introduced in the first chapter; the second chapter involves a two stage monitoring process for identifying the cascading failures using an offline IEEE multi-machine model and an online actual blackout simulation model; the third chapter introduces a novel robust supplementary inter-area oscillation damping control architecture for Multi-terminal Direct Current grids embedded in AC test systems. The fourth chapter develops a novel explicit disturbance rejection model based inter-area oscillation damping and demonstrates effectiveness towards robust performance in the onset of actuator outages, communication loss and other severe outages, and the last chapter concludes this dissertation.

2. FAULT MAPPING IN MULTI-MACHINE POWER SYSTEMS BY PRINCIPAL COMPONENT SENSITIVITY- AN ENERGY FUNCTION PERSPECTIVE

This chapter is based on the work "Fault Mapping in Multi-machine Power Systems by Principal Component Sensitivity-An Energy Function Perspective," *2018 North American Power Symposium (NAPS)*, Fargo, ND, 2018, pp. 1-6. (doi: 10.1109/NAPS.2018.8600648) [53]. The authors of the paper are Abhishek Banerjee [1], Manisha Maharjan and Rajesh G. Kavasseri.

2.1. Introduction

Real time detection of events in large scale multi-machine power systems has been an important topic of investigation for power system operations and contingency measures [54], [55]. Recent works on transient post-fault stability have shown approaches that are completely based on artificial neural networks [25], [56] and decision trees [26]. Analysis has been done on end data collected from various post-fault archived databases, like a Phasor Data Concentrator (PDC). These units store system wide data, including event data that might have eventually lead to a major failure in power system operation. These approaches consider the entire system as a "black-box" problem neglecting the physical attributes of the system wide properties of the system during a transient. The use of many statistical approaches have been commonplace in recent literature [57, 58, 59], where albeit, the predictions of faults can be done, there is no consideration on the loss of such data. Moreover, it is computationally difficult to exploit such huge data in real-time to view the nature of faults occurring during system wide operation. These data driven methods are prone to failure with the loss of data and is not reliable for contingency planning and operations of large scale interconnected power systems.

On the contrary, complete knowledge of system wide changes during fault occurrence by mapping it to its event is necessary to understand the underlying physics of the problem. Now with the proliferation of the Phasor Measurement Units (PMUs), it has become increasingly possible

---

[1]Abhishek Banerjee was the first author and responsible for writing the manuscript and applying simulation tests with additional results from Manisha Maharjan. Dr. Rajesh G. Kavasseri served as the proofreader and gave recommendations and guidance on drafting the paper.

to establish Wide-Area Monitoring, Protection, and Control (WAMPAC) [30], [31], enabling us to access the voltage and current phasors, frequency and its rate of change, and power flows at any point in time. To that context, with the help of the wide-area measurements from PMUs, coupled with state estimation to generate energy functions have shown promising aspects [33], [34]. Every component of the Structure Preserving Energy Functions (SPEFs) [35] in a multi-machine power system can be derived [33], providing complete knowledge of the system energy. Thus, motivated, our goal is to provide a systematic approach to develop one-to-one mapping between properties of energy function components and the occurrence of the type of fault in the system. This approach encapsulates physical overview with a Sliding Window Prediction (SWP) and the mapping is structured by performing Principal Component Analysis (PCA) on individual potential energy components of the SPEFs. After the potential energy components have been constructed from a dynamic simulation, the individual components are subjected to a SWP process to identify similarity in the nature of faults.

This chapter provides a detailed algorithm and computational procedure to identify and map the correlation between the principal components (PCs) and the potential energy functions of an interconnected power system. Significant PCs in case of events are chosen on the basis of percentage co-variance of each dimension. By this approach, meaningful information from events get relayed selectively to a few PCs, reducing the search-space to develop protection measures for limiting cascading events in the future. The chaptre is further organized with SWP process described in Sec. 2.2, background on PCA in Sec. 2.3, test system in Sec. 2.4, results and discussions in Sec. 2.5, and summary in Sec. 2.6.

2.2. Sliding Window Prediction Algorithm

The total energy contained in the a power system can be derived as kinetic energy (W_{KE}) and potential energy (W_{PE}). Extracting useful information embedded in the SPEFs require the full knowledge of the properties it encapsulates. For that purpose, a sliding window based approach is used to determine the characteristics of the SPEF's when subject to different faulted scenarios. It is well known from [33], that the different types of faults will leave different signatures on the wide area measurement system (WAMs). The sliding window approach is designed to detect the sensitivity of the different energy function components to various types of faults. After the energy function components are calculated, the total length of individual components is used to determine the

$$W_{Tot} = W_{KE} + W_{PE}$$

$$W_{KE} = \frac{1}{2}\sum_{i=1}^{M} M_i \varpi_i^2 \qquad W_{PE} = \sum_{i=1}^{11} W_{2i}$$

| Generator 1 | $\to W_{11}$ |

| Loads | $\to W_{22}(t)$ $W_{23}(V)$ |

| Generator 2 | $\to W_{12}$ |

| Transmission lines | $\to W_{25}$ |

| Generator 3 | $\to W_{13}$ |

| Generators | $\to W_{21}(y),\ W_{24}(x,y)$ $W_{26}(y),\ W_{27}(x,y)$ |

| Generator 4 | $\to W_{14}$ |

$W_{28}(y),\ W_{29}(x)$
$W_{210}(y),\ W_{211}(x)$
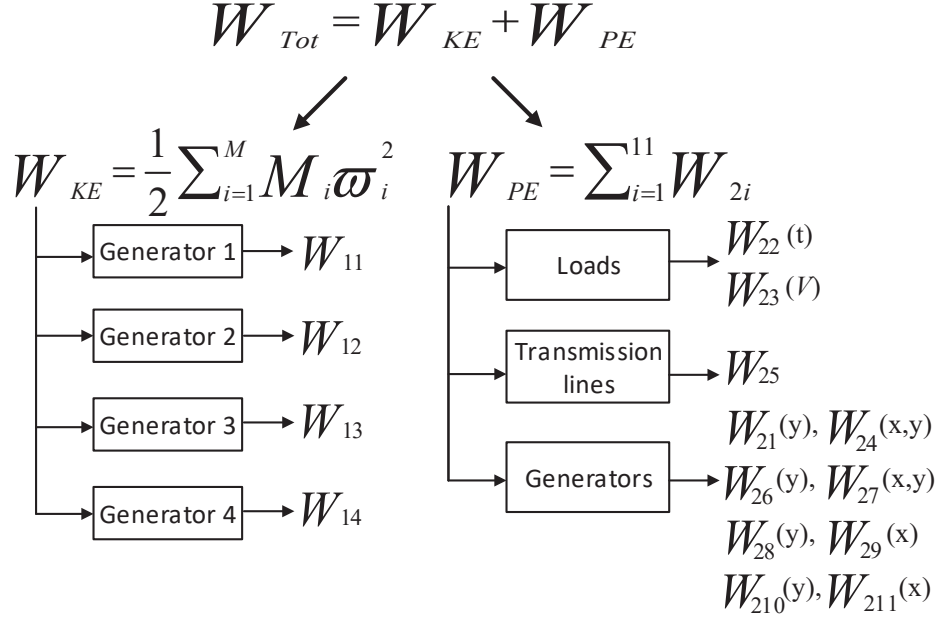
Figure 2.1. Block diagram of the SPEF components

number of sliding windows. An appropriate selection of window width needs to be done in order to capture maximum information from the trajectories of the individual energy function components. The total number of windows is calculated as

$$n_w = \frac{l_w - \varepsilon}{\Delta} \tag{2.1}$$

where,

l_w = length of each component of W_1, $\sum_{i=1}^{11} W_{2i}$

ε = window width, Δ = slide increment

After the total number of windows are determined, the window span is calculated using

$$\sum_{j=1}^{n_w} j : (j + \varepsilon) \tag{2.2}$$

In each window span, each energy component, as shown in Fig. 2.1 is subjected to a singular value decomposition, $\Phi_W = U\Sigma V^T$, where $\sum$ is an n-by-p rectangular diagonal matrix of positive numbers $\sigma(k)$, called the singular values of Φ_W; U is an n-by-n matrix, the columns of which are

orthogonal unit vectors of length n called the left singular vectors of Φ_W; and V is a p-by-p whose columns are orthogonal unit vectors of length p and called the right singular vectors of Φ_W.

2.3. Principal Component Analysis

Principal Component Analysis (PCA) has been a widely used tool in many fields of sciences [60], including power system studies [61]. It helps reduce dimensions and group or categorize objects in the form of linearly independent principal components which are orthogonal to each other [62]. Although many techniques have been proposed for the calculation of PCA [63], the SVD based approach deems perfect for our case, where the sensitivity of the energy functions is a major look out.
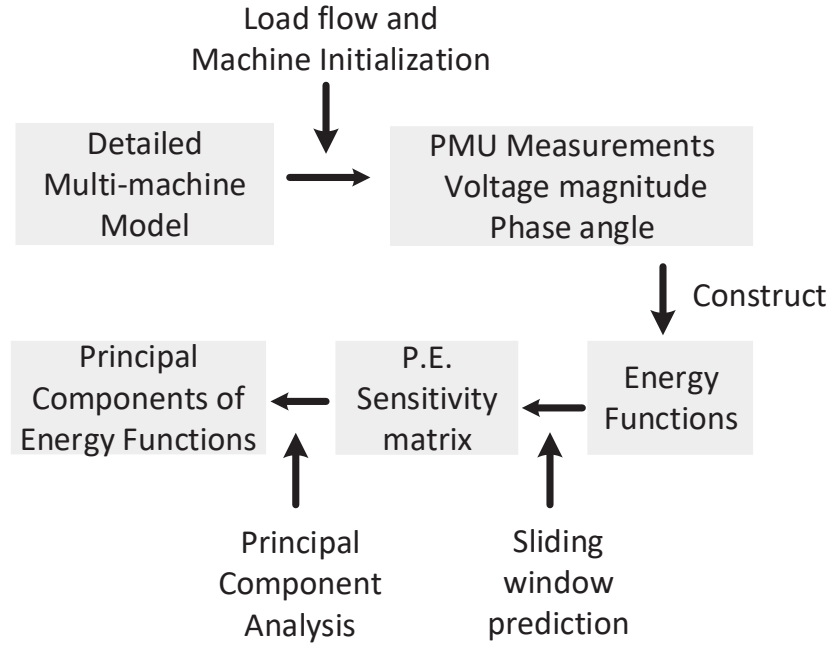
Figure 2.2. Methodology for computing principal components of energy functions.

2.3.1. Procedure of Computation

Different fault scenarios are created to investigate the change in the principal components of the individual SPEF's. To broaden the fault set, different types of faults were simulated such as a temporary 6-cycle fault between the transmission line connecting buses 7 and 8, generator 1 excitation failure and others as mentioned in Table 2.1 and Table 2.2.

Table 2.1. Events Comprising Dataset I

Events Occurring	Fault Location	Total dominant PC's	% variance
Temporary 3ph fault	bus 7/8	4	≥95%
Load change	bus 8	2	≥95%
Permanent 3ph fault	bus 7/8	4	≈90%
Excitation failure	generator 1	2	≈95%

Table 2.2. Events Comprising Dataset II

Events Occurring	Fault Location	Total dominant PC's	% variance
Temporary 3ph fault	bus 5/6	4	≥91%
Load change	bus 7	2	≥95%
Permanent 3ph fault	bus 7/8	4	≈90%
Generation loss	generator 4	2	≥93%

Organization of the simulated data with respect to the SPEF's is carried out by simultaneously simulating the non-linear test model and also generating the SPEF's routine. Individual SPEF's are calculated one by one. This process, as depicted in Fig. 2.2, is done for individual events one by one to generate all energy functions pertaining to all the fault scenarios. Once the SPEF's have been obtained, the potential energy terms are stacked up in a matrix represented as

$$W_{SPE} = [W_{21} \ W_{22} \ \ldots \ W_{2i}], \ where \ i = 1, 2, 3, \ldots, 11 \tag{2.3}$$

where, W_{SPE} stands for the Stacked Potential Energy and $[W_{21}, W_{22}, ..., W_{211}]$ represent individual P.E. components as shown in Fig. 2.1. The matrix obtained here is normalized, as explained in the next part for performing further calculations.

2.3.2. Normalization of Data

Normalizing bounds the data and provides a range over which the analyzing tools can be deployed for proper meaningful output. The data obtained from the dynamic simulation are pre-processed using (2.4), a priori the PCA routine is carried out. The individual P.E. components are normalized as;

$$\forall \, n \in W_{SPE},$$

$$W_N(n,j) = \sum_{j=1}^{11} \frac{W_{SPE}(j) - \min(W_{SPE}(j))}{\max(W_{SPE}(j)) - \min(W_{SPE}(j))} \qquad (2.4)$$

where,

n: number of rows of W_{SPE} matrix corresponding to observations

j: number of columns of W_{SPE} matrix corresponding to each P.E. component

W_n: Normalized stacked P.E. matrix

A PCA is performed on this matrix by the singular value decomposition algorithm as mentioned in Sec. 2.3.

2.3.3. Selecting Contributing Components

The PCA routine of the sliding window gives us eleven PC's with different variance and significance. It is necessary to choose the a few most effective PC's to reduce the dimesionality of the data and to visualize activity in the principal directions of the individual EF's. An elbow-scree plot was used for this selection procedure. It derives its name from the typical shape of the accumulation of loose rubble or scree at the foot of the mountain slope. It is a very effective way to screen high fidelity data. The method to interret the scree plot as suggested originally by [64, 65] involves analyzing a plot of the variance (V_k) of the kth PC from the correlation matrix. The selection of the number of PC's depends on the steepness to the left and the right side of the scree plots [66, 67]. The effective screening criteria can be described as $[V_{k-1} - \& \ V_k]$, where the effective PC after which the remaining PC's form a straight line is determined. This scree plot was done for all the four cases of the simulated fault events as shown in Fig. 2.3.

2.3.4. Component Burden

Figure 2.3 (a),(b) shows the percentage variance of each principal component for the two data sets of events as mentioned in Section2.5.1. In both the plots, it can be seen that the 1st and 2nd PC's of the load event and the generator event contain more than 90% of the variance whereas for the line faults they contain about 60% variance for the permanent 3ϕ fault, and 70% for the temporary 3ϕ fault. Thus, the 1st and 2nd PC's can account for most of the changes in the case of the load and generator event but for the line events we need more than two components to facilitate
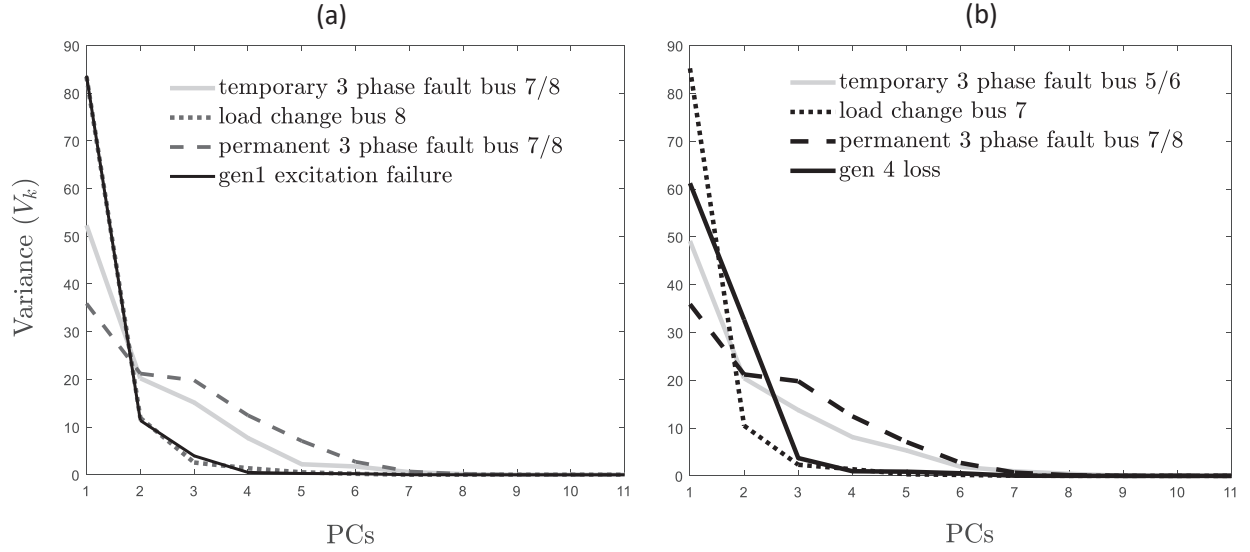
Figure 2.3. Elbow-scree plot for the faults, (a) Dataset 2.1 and (b) Dataset 2.2 simulated on the test system.

maximum capturing of information during such faults. As a result, the 3rd and 4th components for the permanent and temporary 3ϕ line faults have to be taken into consideration which comprise of about 20% more variance.

2.3.5. Detection Evaluation Criteria

In order to determine the effectiveness of the classification approach, a confusion matrix based analysis, as shown in fig. 2.4, is performed on the test system. The confusion matrix [68]
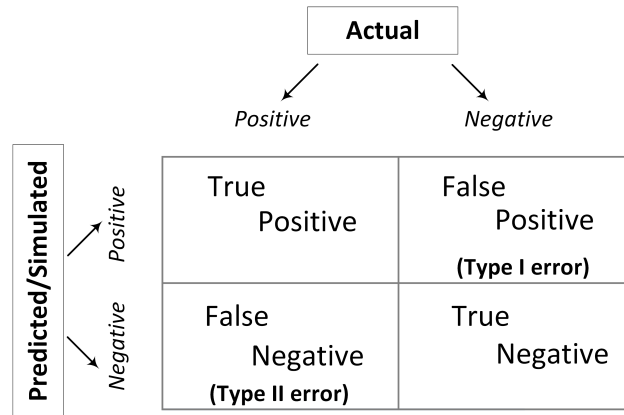
Figure 2.4. Confusion matrix representation

is a very useful tool to decipher the positive and negative outcomes from a series of combinations of actual versus expected outcomes. This statistical measure has been deployed in various fields of science and engineering [69, 70, 71, 72] to understand the coupling between a set of data, and their mutual correlations. More recently, the use of confusion matrices for data classification has been commonplace in artificial neural network(ANN) related studies [73] and for statistical analysis based classification techniques in power systems [74, 75, 76]. Figure 2.4 depicts the structure of the confusion matrix, and all the possibilities that can be the result of particular scenarios. A statistical approach is used to determine the correctness of the event classifications for sensitivity analysis. The classification accuracy is calculated by taking the number of correctly identified samples and dividing by the total number of actual simulation samples into the test data set, as represented in the Confusion Matrix (CM) in Table 2.3, 2.4. Percentage efficiency for the classification of the type of fault is presented which is a significant indicator of the performance of the approach. The scenarios are labeled according to the following convention:

S1: Actual fault detected

S2: Actual fault not detected

S3: Non-faults mistakenly detected

S4: Non-faults not detected

where, for two-class scenarios and the fault detection algorithms, CM is a 2×2 matrix defined as:

$$CM = \left[\begin{array}{c|c} S1 & S2 \\ \hline S3 & S4 \end{array} \right] \tag{2.5}$$

As shown in Table 2.3, twelve emulations of different line events on the grid were simulated and the following outcomes were noted for changes in the line energy function W_{25}. Out of the twelve total events, ten were actual fault events and two were non-faults events simulated to test the confusion matrix outcomes. The confusion matrix in Table 2.3 depicts that nine out of the ten line events simulated were identified as actual faults showing an efficiency of 90%, whereas only one line fault is remains undetected by the line energy function. Similarly, both the instances of non-fault are classified correctly giving it 100% efficiency. The overall efficiency for identifying a line fault using W_{25} was found to be 95.83%.

Table 2.3. Confusion Matrix for Line Fault Indicator-W_{25}

Line Events				
Scenario/ Outcome	S1	S2	S3	S4
S1	9			
S2	1	0		
S3			0	
S4				2
Efficiency %	90	0	0	100
Overall Efficiency %		95.83		

A similar approach was adopted to test the effectiveness of the proposed generator event classifier during fault scenarios simulated on the grid. A total of ten generator faults were simulated on the test system, which include generator real power loss, field excitation loss in generators and generator outage scenarios. Out of these, W_{21} classified eight out of ten actual generator faults with an efficiency of 80%. Two instances of actual faults were classified as non-detected as shown in Table 2.4. In addition to that four non-fault events were simulated, which are correctly classified with 100% efficiency.

Table 2.4. Confusion Matrix for Generator Fault Indicator-W_{21}

Generation Events				
Scenario/ Outcome	S1	S2	S3	S4
S1	8			
S2	1	1		
S3			0	
S4				4
Efficiency %	80	90	0	100
Overall Efficiency %		90		

The Accuracy (Acc) can be calculated to embark on the all-scenario based performance of the method, by dividing the number of right scenarios by the overall total number of scenarios

$$Acc = \frac{S1 + S4}{S1 + S2 + S3 + S4} \tag{2.6}$$

20

The Reliability(R) illustrates the ability of the method to detect and isolate the correct associated components to the simulated faults. This metric can be calculated by the ratio of the number of detected faults to the actual number of the simulated faults

$$R = \frac{S1}{S1 + S2} \tag{2.7}$$

Based on the grid outages simulated on the test system as shown in fig. 2.5, the accuracy and reliability is summarized in Table 2.5. The overall performance very accurately reflects the behavior of the simulated grid.

Table 2.5. Metrics Derived from CM

Metrics	Line events	Generator events
Acc %	91.67	85.71
R %	90	80

2.4. Test System Description

A 4-machine, 2-area system Fig. 2.5 [36] was considered as the test system. A positive sequence fundamental frequency phasor model of the test system was developed in MATLAB/Simulink. The detailed model of the generators are represented as in 1.1 generator model of [35] with the IEEE type one excitation system, and a steam turbine model for the prime mover control system. In steady state, approximately 400 MW flows from area 1 to area 2 over the 220 km transmission line connecting buses 7 & 8. The measurements collected at all the buses are sampled at a rate of 1 sample per cycle to represent the PMU data rate.

2.5. Results and Discussion

In this section, some results of applying the SWP based PCA analysis to the test system subject to different fault scenarios is presented. Non-linear simulations were performed for 60 secs on the test system in MATLAB/Simulink [77] for each event as mentioned below.
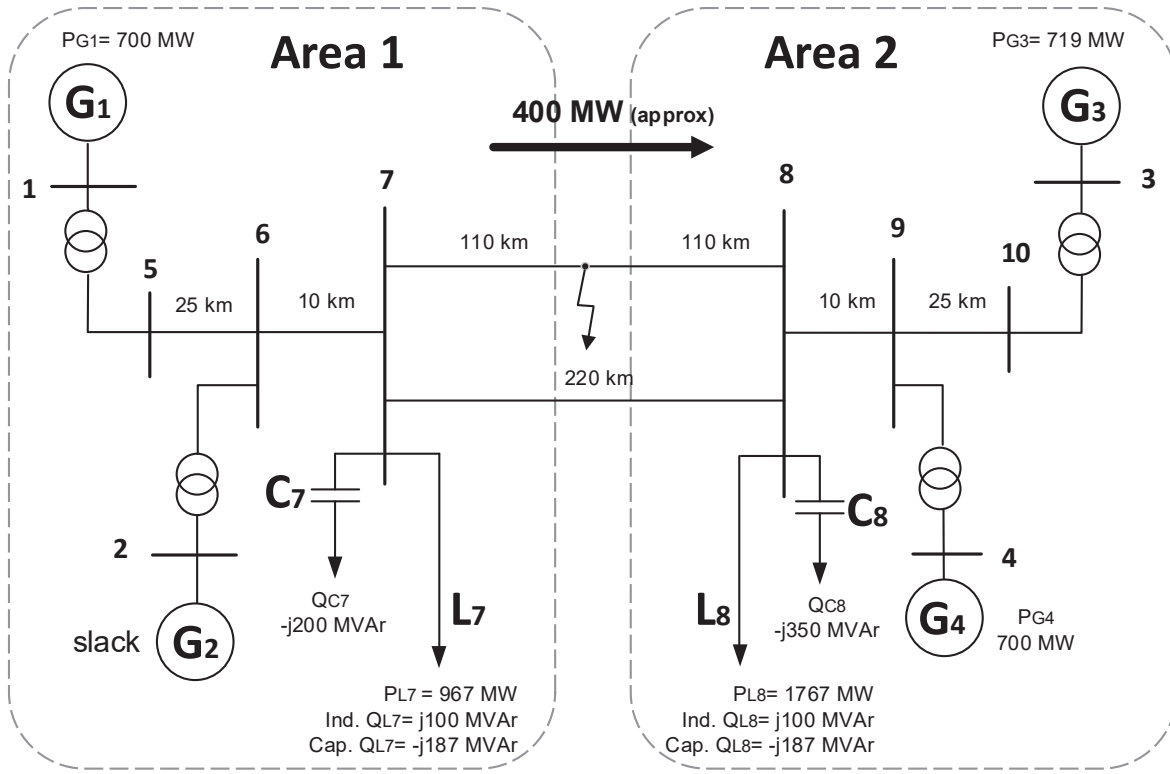
Figure 2.5. Two-area, four-machine system.

2.5.1. Simulated Faults

In order to understand how the PC's of the potential energy functions respond, a set of fault events were simulated one at a time. These events cover overall fault scenarios that may occur in real-time in a multi-machine power system. The events considered are listed below.

- Excitation failure of a generator in Area #1

- Complete loss of a generator in Area #2

- Step change in reference power of a generator in Area #1

- 6-cycle, temporary 3ϕ to ground fault in lines connecting buses (7-8) and (5-6) at $t = 1.0$ s

- Permanent 3ϕ to ground fault in the midpoint of the line connecting buses (7-8) followed by permanent loss of line, at $t = 5.0$ s

- Active and reactive power addition in bus #7 and #8

22

The location of the events mentioned above can be found in the test system in Fig. 2.5. The events are grouped into two data sets, each representing 4 event sets as shown in Tables 2.1 and 2.2.

The machine excitation failure was mimicked at $t = 5.0$ s for 6-cycles, by introducing a step change in the field voltage of generator #1. Also, generator #4 power loss is simulated at at $t = 5.0$ s, when the real power output of the machine drops to zero.

2.5.2. Component Screening for Line Event

A detailed evaluation of all energy function components was carried out with respect to each event mentioned in Tables 2.1 and 2.2. Fig. 2.6 shows the response of the energy component W_{25} subject to all the four events for each dataset. It can be observed that the permanent 3ϕ fault and the temporary 6-cycle, 3ϕ fault affect the 1st and 2nd PC of W_{25} component which captures the relative change in magnetic energies stored in transmission lines. It should be noted in Fig. 2.6, the load change event and the generator events do not affect this component significantly. This gives us an insight to consider W_{25} as an input for designing transmission line protection like relaying protocols. It can also be observed from Fig. 2.6(b), the generator reference power change shows considerable change on it 2nd PC, but it should be understood that the 2nd PC contains only about 11% of the total variance and is hence insignificant.

□ *Note:*

Figures 2.6, 2.8, and 2.9 show crosses on the bars of generator event and load event, 3rd and 4th PC. This was inserted manually to depict that only the first two PC's contain most information as shown in Fig, 2.3, and that the crossed bars signify zero change and was inserted to only accomplish the 3-D plots.

2.5.3. Component Screening for Generator Event

Figure 2.7 depicts the change in the W_{21} component subject to both set of events. This component captures the sensitivity of the change in P.E. due to mechanical input to the machine relative to its centre of inertia. It can be seen that the generator events show maximum variation for this component in the 1st and 2nd PC's compared to the other events. Moreover, it can be inferred that the generator #4 loss renders W_{21} to deviate more than the generator #1 excitation failure event. This leads to a very intuitive understanding of the component W_{21}, and any changes in this component can be directly linked to ongoing real-time changes in the generating units of a power system.

23
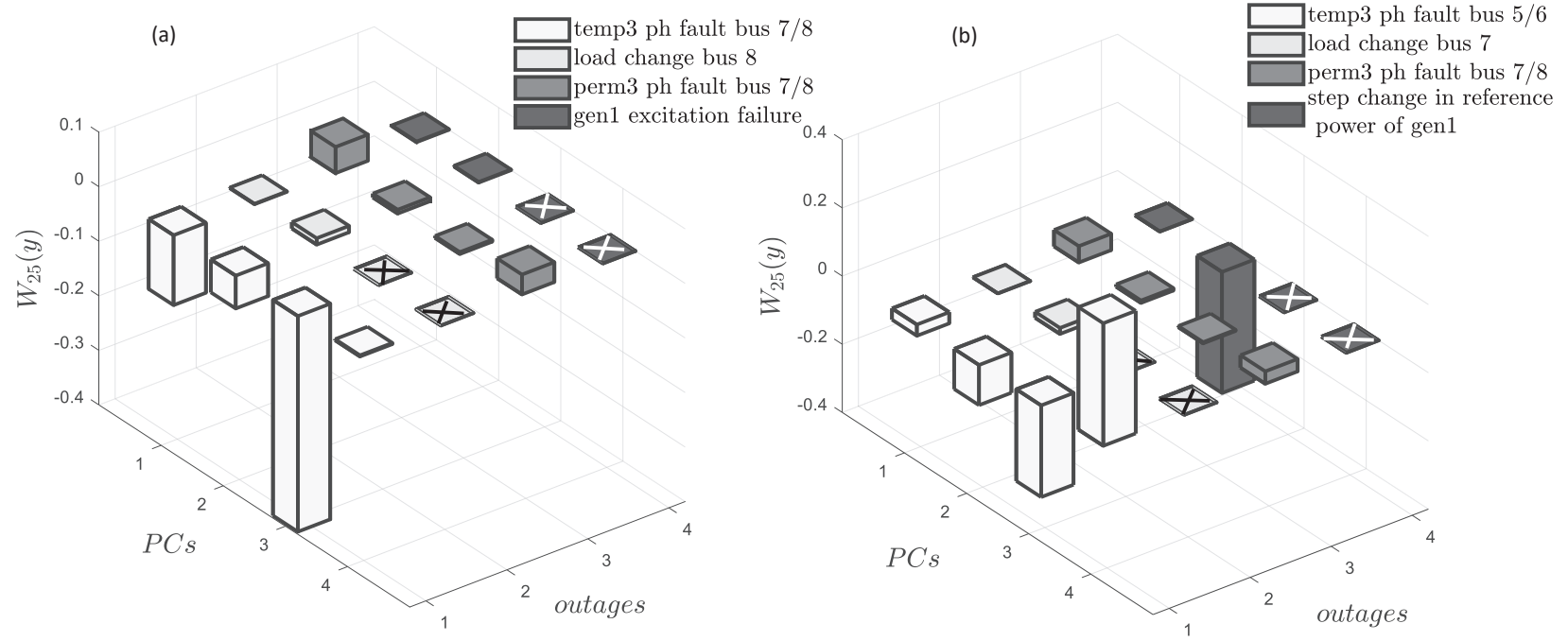
Figure 2.6. Change in energy component W_{25} with respect to the events in (a) Dataset 2.1 and (b) Dataset 2.2 for the $(1^{st} - 4^{th})$ PCs.
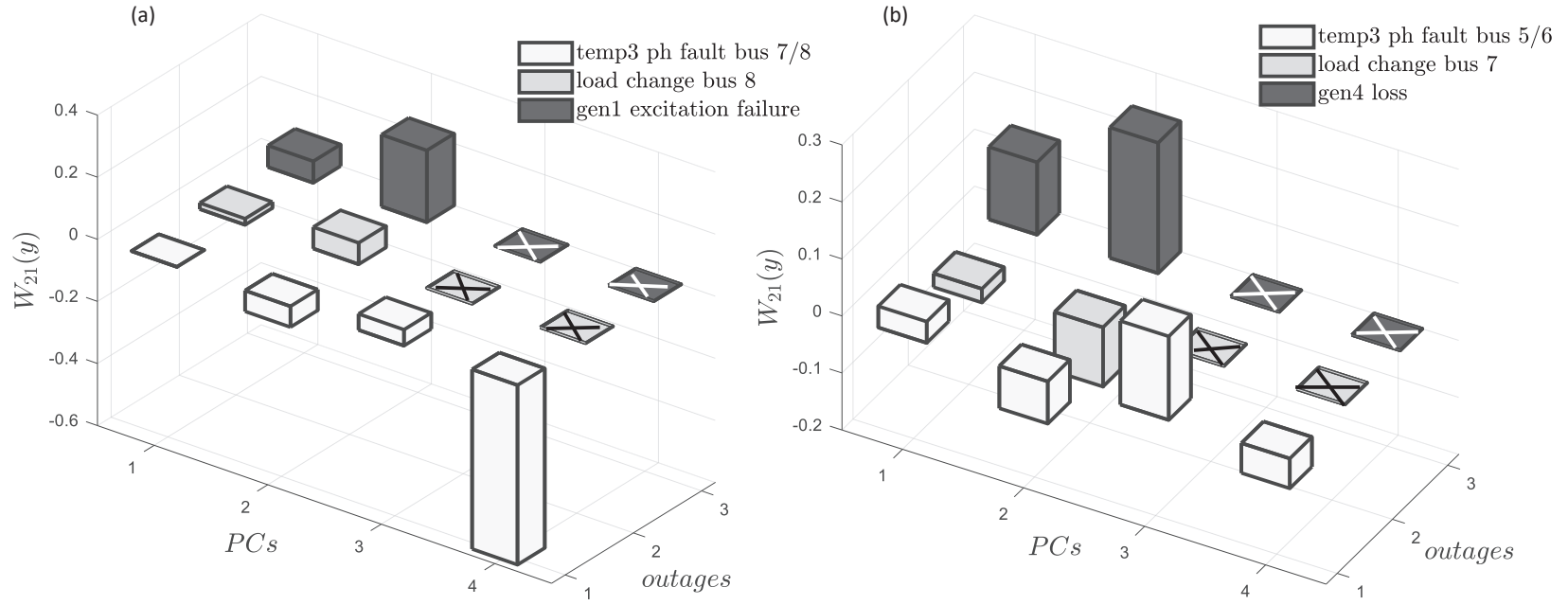
Figure 2.7. Change in energy component W_{21} with respect to the events in (a) Dataset 2.1 and (b) Dataset 2.2 for the $(1^{st} - 4^{th})$ PCs.
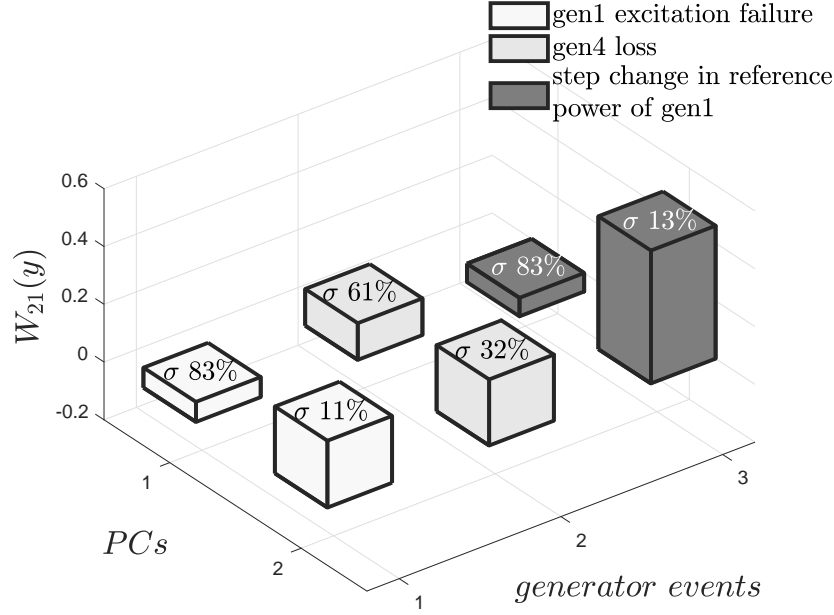
Figure 2.8. Change in W_{21} energy component in case of different generator events for the 1st and 2nd PC.

All the generator events simulated has been plotted in Fig. 2.8, which shows the dominant PC's, with PC percentage variances denoted by σ . The percentage variation in each PC for generator #4, makes it the most severe fault, whereas the other events show most variation in the 2nd PC which has negligible contribution.

2.5.4. Component Screening for Load Event

At $t = 5s$, a constant impedance load of 200 MW active and 100 var reactive power was added to bus 7 in Fig. 2.5. Figure 2.9 depicts the change in the energy function component W_{22}. This component accounts for the relative (i.e., with respect to a steady state operating condition) changes in P.E. due to active and reactive loads. The first principal component carries here about 85% variance for load change, and it can be seen that it has the highest change with respect to the load event, signifying the importance of the 1st PC of W22 in case of high active loading at bus 7 in the test system.

2.5.5. Analysis Using Biplot

A biplot is a graph that represents points and vectors of a data structure in a single plot. Fig. 2.10 shows biplot of W_{SPE} matrix generated from energy functions after applying generator #1
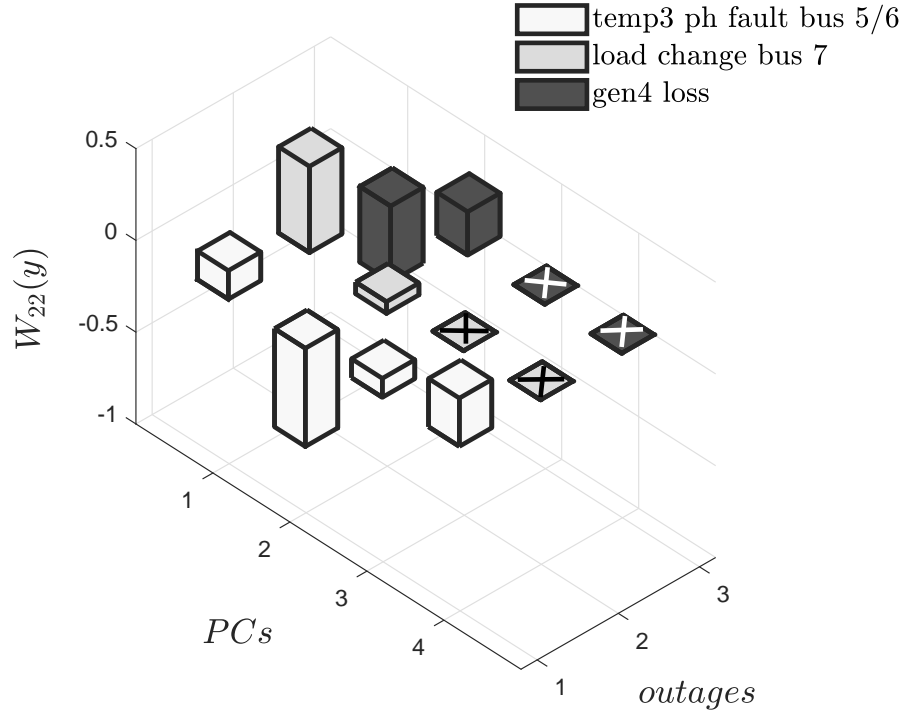
Figure 2.9. Change in W_{22} energy component in case of Dataset 2.2 for the $(1^{st} - 4^{th})$ PCs.

excitation failure in the test system. As in case of PCA, the axes of biplot are principal components, which are labeled PC 1, PC 2, and PC 3. The points in the biplot represent the scores of the observations corresponding to the PCs, and the vectors represent the coefficients of the P.E. components on the PCs. The orientation of vector projection displays the relationship between the P.E. components and the PCs. It can be noticed that W_{23}, W_{25}, and W_{28} all project in same direction and line up completely with 3rd PC, indicating that they load heavily on PC 3 in the positive direction. W_{23} relates to P.E. term due to reactive component of load, W_{25} indicates towards transmission lines (which are reactive in nature), and W_{28} relates to the q axis of damper windings. Hence, it makes sense when these components align in the same direction in the biplot, indicating that they are highly correlated for this particular data. Similar finding can be applied to W_{210} and W_{211}, but negatively correlated with 3rd PC.

Further, the vectors that point in the same direction can be said to have similar response with respect to the data provided. W_{22}, W_{26}, and W_{27} all point in same direction towards the scores

27

as these are all dependent on terminal voltage at generator bus. These components will have large effect on the scores because generator excitation failure is being emulated in this scenario.
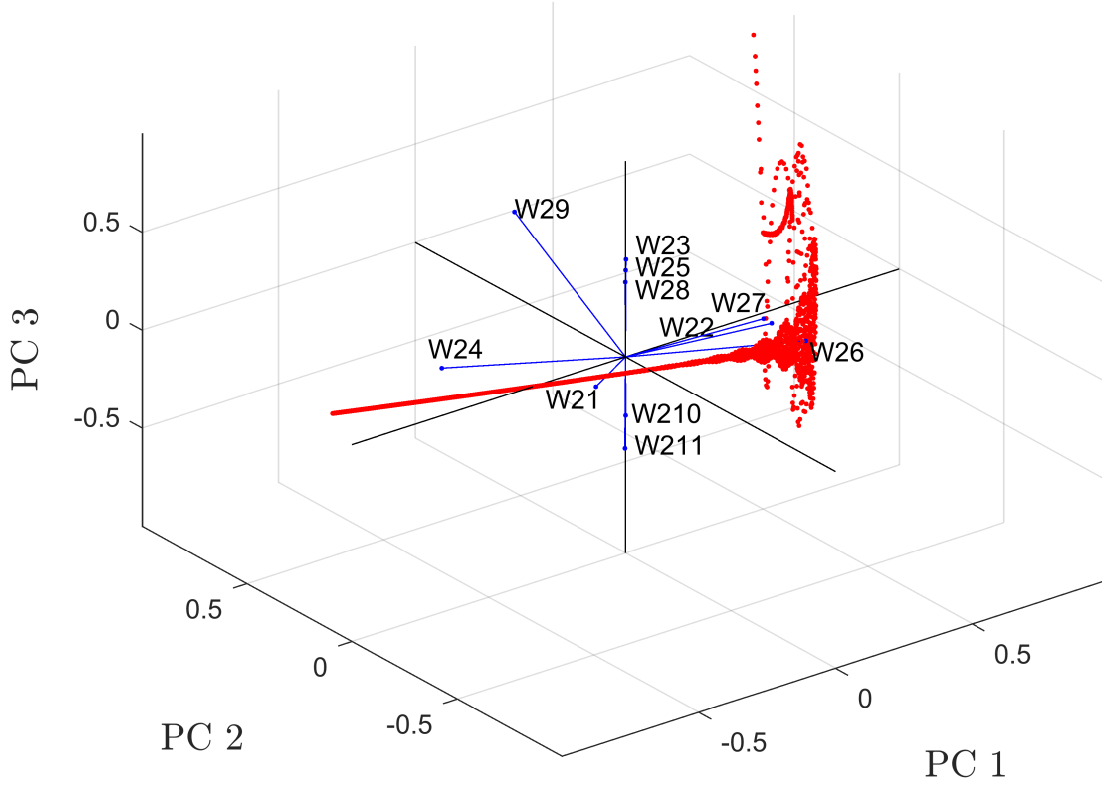
Figure 2.10. Biplot of principal component coefficients and scores of energy functions.

2.6. Summary

This chapter presents an alternate method of fault detection by exploring the principal components of the potential energy functions, in turn avoiding the hectic computational burden and time complexities imposed by other pertaining methods. By taking the energy function components into mainstream calculations, we delve more into the physical aspects of event occurrences and their effects on the interconnected system components. The results indicate that certain PCs of individual energy functions are highly affected by different events, lessening the search-space by reducing dimension, and aiding in faster on-line calculations. Using energy components as supplementary

data in other existing procedures of event detection might increase the chances of detection and isolation of the triggering components. This serves as motivation for protection of components in power system and preventing black-outs by identifying cascading events. In the next chapter, this work is extended to a larger IEEE New England 39-bus system, where we expect to notice more interesting interactions between the energy functions and event occurrences.

3. TOWARDS SUPERVISORY PROTECTION USING ENERGY FUNCTIONS FOR RELAY MISOPERATIONS IN A STRESSED POWER SYSTEM DURING BLACKOUT

This chapter is based on the work "Towards Supervisory Protection Using Energy Functions for Relay Misoperations in a Stressed Power System During Blackout," *2019 IEEE Milan PowerTech*, Milan, Italy, 2019, pp. 1-6. (doi:10.1109/PTC.2019.8810539) [78]. The authors of the paper are A. Banerjee [1], R. G. Kavasseri, M. B. Gani and S. Brahma.

3.1. Introduction

Distance relays with zonal protection often operate during stressed conditions with the potential to eventually initiate a cascade. Such events can be precipitated by zone 3 trips by distance relays due to load encroachment. Such operations in bulk power systems during stressed conditions, especially in the absence of actual faults, can be undesirable from a systems stability standpoint. These might include a genuine misoperation, a false trip due to cyber attacks, or a load encroachment, all of which are undesirable under these circumstances. The works in [79, 80] have analyzed the sensitivity of zone 3 of distance relays under various operating conditions while abstaining from a large number of power flow studies. Solutions to relay misoperations have been explored in [81, 82, 83], which suggest using support vector machines (SVMs) for offering supervisory control in conventional relays. In [84, 85] the authors propose blocking zone 3 of certain distance relays ahead of time based on offline simulations for preventing cascading events. Unlike these works, we present a solution to supervise distance relay actions using measured data from phasor measurement units (PMU) and the concept of energy functions. The *key idea* in our work is that energy function components, rich in dynamic state information are intrinsically tied to the physical sub-systems. These components can provide more specific clues in identifying critical system events, than methods that utilize purely algebraic variables.

---

[1]Abhishek Banerjee was the first author and responsible for writing the manuscript and applying simulation tests with additional results from Munim Bin Gani. Dr. Rajesh G. Kavasseri and Dr. Sukumar M. Brahma served as the proofreader and gave recommendations and guidance on drafting the paper.

Lyapunov-like energy functions have been described in [35], where kinetic and potential energy functions have been derived which account for machines, loads, lines and other components of a power system. Complete construction of all the sub-components of the energy function require information on the dynamic states. The availability of PMU data combined with estimation techniques which include Kalman-based [86, 87], or nonlinear particle filter-based methods [33], the dynamic states can be computed accurately. The estimated states and PMU data assist to synthesize energy functions that can be used for event detection as proposed in [33] and [53]. This motivates us to examine what further indications these energy function components can provide, especially during stressed conditions, and how they may by used to supervise critical tripping decisions by distance relays.

During heavy system loading conditions, relay operations are possible when load encroachments are misinterpreted as faults. Based on our recent works [33, 53, 88] that examines energy function sensitivity during faults, we propound monitoring the energy function sub-component (W_{25}), to supervise distance relay operations. We also use insights from recent work [88] which was successful in reconstructing a blackout sequence that occurred in 2011, in the Pacific Southwest area spanning Arizona, southern Califorina, and Baja California, Mexico under WECC [89], using actual field data and GE's positive sequence Power system load flow (PSLF) tool. Two test beds provide encouraging results, NETS model being the selection model and the WECC model being the stressed system on which the selected component is tested in real-time. The chapter is further organized with proposed approach for energy component selection in Sec.3.2, test system descriptions in Sec.3.3, 3.4, results and observations in Sec.3.5, 3.6, and conclusions in Sec.3.7.

3.2. Proposed Approach for Energy Component Selection

Energy functions in power systems can be divided into kinetic energy (W_{KE}) and potential energy (W_{PE}) components. Fig. 3.1 shows the different components of the energy functions linked to the elements which they are associated with. We consider the models for the system dynamics as (3.1) and measurements in the form (3.2).

$$x_{k+1} = f_k(x_k, w_k) \tag{3.1}$$

$$y_k = h_k(x_k, v_k) \tag{3.2}$$

where w_k and v_k are white independent noise processes with known pdf (N(0,R)), used for the particle filter design, refer to [33]. The dynamic model states are defined in (3.1), which represent generator states like

$$x_g = (\delta, \omega, E_q', E_d', E_{fd}) \tag{3.3}$$

that are estimated using the particle filter approach as in [33]. The measurements y_k in (3.2) include the real and reactive powers at the generators. It should be noted that the estimation process is only required for energy components linked to the generators. For the components associated with the transmission lines (W_{25}) and loads (W_{22}, W_{23}), shown in Fig. 3.1, estimation is not required since all the measurements are available through the PMU's. It is shown in [33] using a (2-area, 4-machine) test system, how specific system events can be attributed to changes in specific energy function component traces. Also, by introducing a new approach of principal component sensitivity of potential energy (P.E.) functions, [53] demonstrated how the effects of different events could be

$$W_{Tot} = W_{KE} + W_{PE}$$

$$W_{KE} = \frac{1}{2}\sum_{i=1}^{M} M_i \varpi_i^2 \qquad W_{PE} = \sum_{i=1}^{11} W_{2i}$$

Generator 1	$\rightarrow W_{11}$
Generator 2	$\rightarrow W_{12}$
Generator 3	$\rightarrow W_{13}$
⋮	⋮
Generator M	$\rightarrow W_M$

Loads	W_{22} (t) $\quad W_{23}$ (V)
Transmission lines	W_{25}
Generators	W_{21}(y), W_{24}(x,y) $\quad W_{26}$(y), W_{27}(x,y) $\quad W_{28}$(y), W_{29}(x) $\quad W_{210}$(y), W_{211}(x)
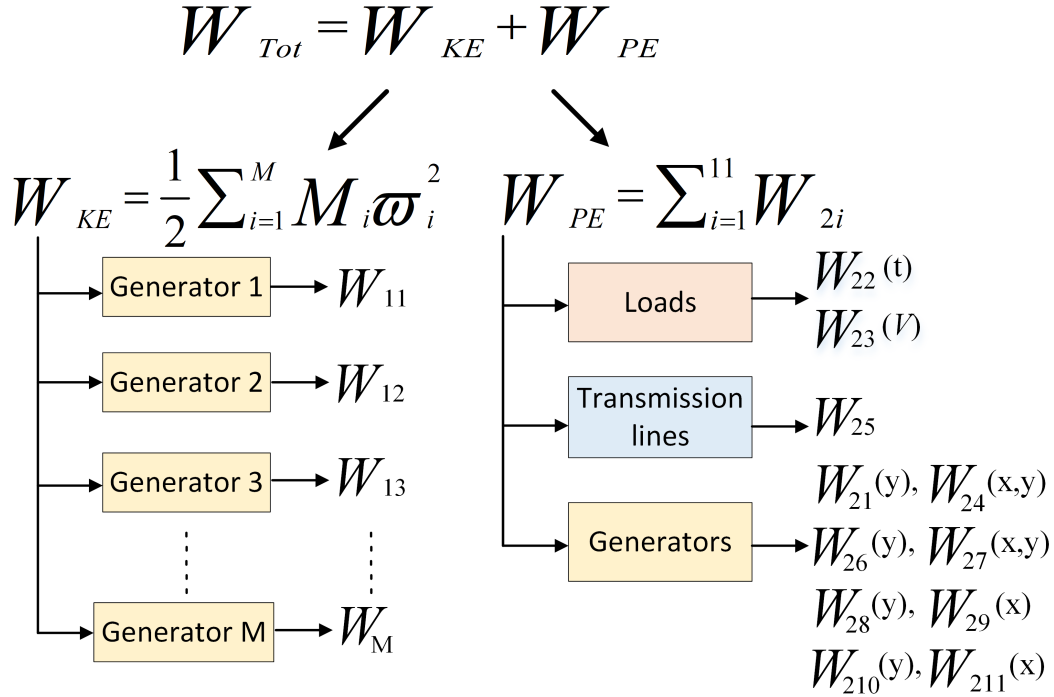
Figure 3.1. Energy functions components for all components

mapped to the individual energy functions. Here, we explore and extend these methods on larger multi-machine power systems where we expect to observe more complex dynamics. Therefore, the NETS is chosen for offline study and the WECC model is considered an online test system replicating an actual blackout sequence. This poses a greater challenge to identify and validate the choice of the key component that could be in used in the future to mitigate a cascade, among all the other energy function components that are accessible in accordance to [33].

3.2.1. Constructing W_{25}

The relative change in magnetic energies stored in the transmission lines is captured by the P.E. component W_{25} [35]. This component can be calculated using (3.4),

$$W_{25} = -\tfrac{1}{2} \sum_{i=1}^{N} \sum_{j=1}^{N} B_{ij} \left(V_i V_j \cos\left(\phi_{ij}\right) - V_{i0} V_{j0} \cos\left(\phi_{ij0}\right) \right) \tag{3.4}$$

where,

$Y_{ij} =$ the system bus admittance matrix

$B_{ij} = Imag(Y_{ij})$,

$\phi_{ij} = \phi_i - \phi_j$.

The subscript "0" here denotes the pre-fault values. It should be mentioned that the particle filter is not required for calculating this energy function as it only requires the system wide measurements observable through the PMUs.

3.2.2. Two Stage Monitoring

The proposed method first evaluates the sensitivity of energy function components on the NETS model, Fig.3.2 for several fault scenarios shown in section 3.5, using energy functions synthesized using the dynamic state estimation approach in [90]. The second stage involves screening this chosen component in terms of an actual stressed system condition. For that purpose, a cascade is initiated on a part of the WECC test system ultimately leading to a blackout. A common misoperation that takes place during progression of a blackout is load encroachment. It occurs in distance relays where the relay misinterprets overload as a system fault. In stressed system condition, when the line voltage is low and the current is high enough to make the impedance locus enter into the zone 3 setting of the relay, the relay trips, misinterpreting it as a fault. If the transmission line

energy function W_{25} can reliably identify an actual fault event, then continuous monitoring of W_{25} can separate the two events in real time, and the supervisory protection layer proposed in [91] can thus detect this common misoperation. The next section analyzes the suitability of W_{25} to detect the misoperations using data generated from the simulation. At this stage, our main focus is to decipher the role of W_{25}, when relay trips occur in zone 3 due to load encroachment. It should be noted that computing W_{25} requires complete knowledge of wide-area measurements using PMU data.

3.3. New-England Test System

The particle filter based dynamic state estimation as suggested in [90] is used to construct the energy functions of the test system. According to a NERC report [92], most PMUs are capable of sampling 30 measurements per second. In this study, the measurement sampling rate for all test cases is 30 measurements. The generators are modeled accounting for sub-transient dynamics [36]. The prime mover dynamics (steam-turbine governor) and the excitation system (IEEE DC1A) models are considered for each generator except for generator #10, which has constant excitation
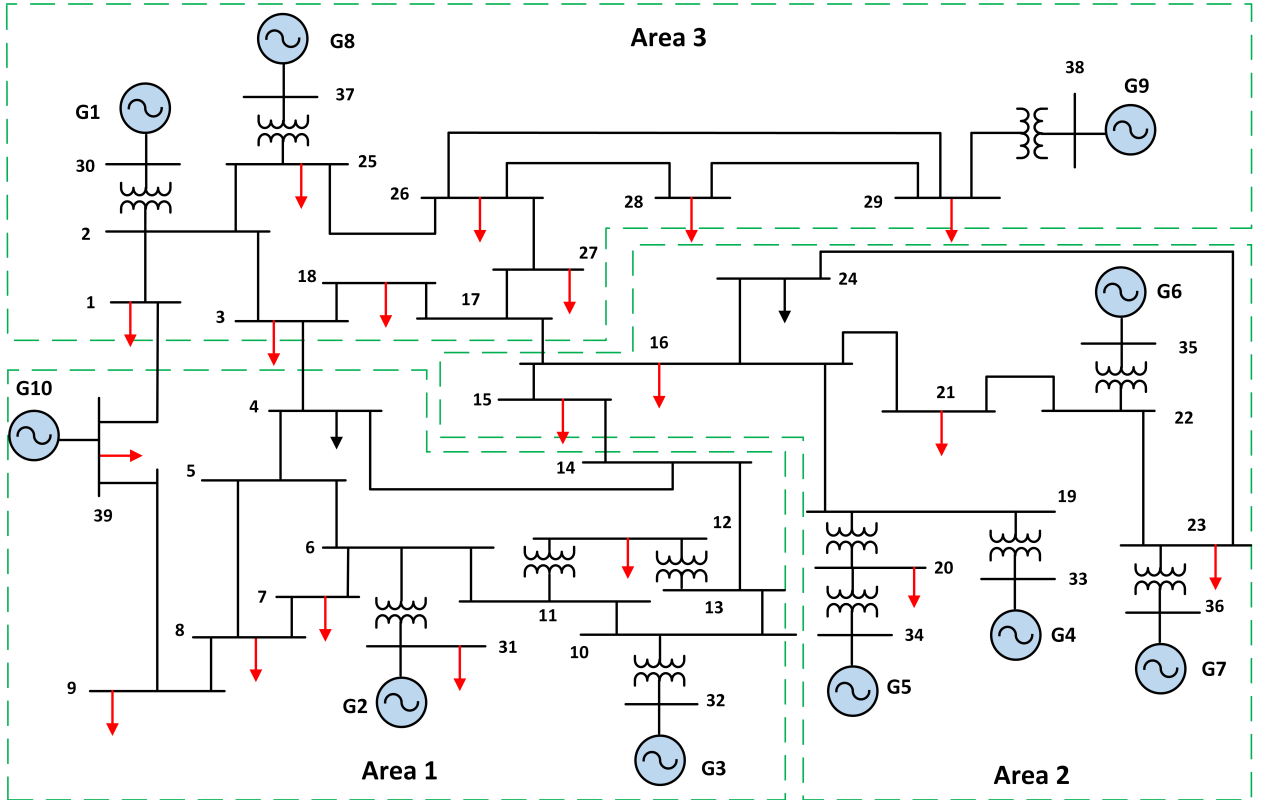
Figure 3.2. IEEE 39-bus New England Test System

input. The simulations were carried out on a desktop PC with 3.6GHz clock-speed, core i7 processor, and 16GB memory.

3.4. WECC Test System

A dynamically simulated blackout that occurred in Pacific Southwest on September 8, 2011 was used as a second test bed. While details about the blackout event and its simulation can be found in [88], [89], a brief summary of its highlights is described here for completeness. Within the WECC system shown in Fig. 3.3, several utilities spanning service areas in Arizona, Southern California, and Baja California, Mexico were affected during that event. Table 3.1 enlists the name and affected service areas of those utilities and Fig. 3.3 shows an overview of the affected power system, including the utility-boundaries [88, 89].
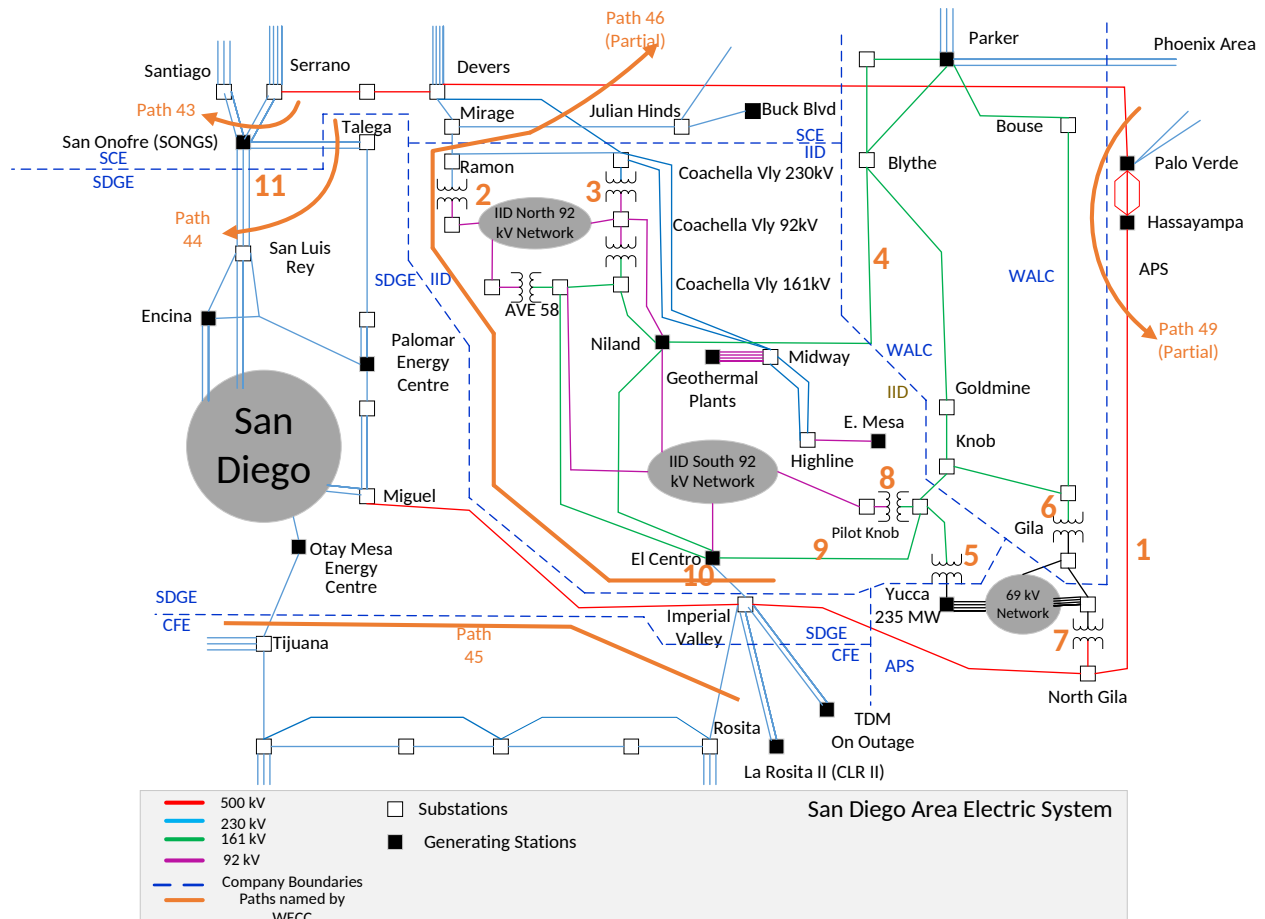
Figure 3.3. Overview of the WECC power system.

Table 3.1. Utilities Affected by Blackout

Name of Utility	Area affected by blackout
Imperial Irrigation district (IID)	Whole area of Imperial Valley, the eastern part of Coachella Valley and a small portion of San Diego County, California
San Diego Gas and Electric (SDG&E)	Whole area of San Diego County and a portion of southern Orange County
Arizona Public Service (APS)	Yuma area load pocket consisting of 69 kV network
Western Area Power Administration-Lower Colorado (WALC)	Lost power partially
Southern California Edison (SCE)	San Onofre Nuclear Generating Station (SONGS)
Comision Federal de Electricidad (CFE)	Whole area of Baja California, Mexico that is connected to WECC.

3.4.1. Load Encroachment Events During Blackout

The blackout was initiated by the tripping of Hassayampa- North Gila 500 kV line which was carrying approximately 1400 MW of power to San Diego (No. 1 in Figure 3.3). It took approximately 11 minutes from the initiation to complete outage in the affected areas. All the affected transmission facilities are numbered from 1 to 11 in Figure 3.3. Of those events, trippings of Niland- Coachella Valley 161 kV line and Elcentro- Pilotknob 161 kV line are of main interests for the scope of this paper as those trippings took place due to load encroachment.

After the tripping of Hassayampa- North Gila 500 kV line power flow redistributed through the lower voltage network of IID and this increased power-flow created stressed condition in the network, i.e., low voltage in the buses and high current in the transmission facilities. This eventually made the relays associated with Niland- Coachella Valley line and Elcentro- Pilotknob line to misinterpret the overflows as system faults under zone 3 and tripping happened worsening the system condition. These two events will be targeted for real time detection of relay misoperations by constructing transmission line energy function W_{25}.

3.4.2. Simulation Methodology and Results

All the affected areas under the jurisdiction of WECC were studied using utility supplied data in PSLF. The simulation was done by first initializing the power flow conditions prior to onset of the blackout followed by dynamic simulations tracing the key events. WECC provided dynamic

data file was used to conduct dynamic simulations for 11 minutes incorporating all the disturbance events described in the blackout progression sequence. Later, appropriate relay models were inserted in the dynamic simulation to trip the transmission facilities rather than tripping them by manual commands.

A list of key transmission facilities was prepared according to the guidance of [89]. These were the facilities where power flows were reported in [89] either by tabular form (for initial intact system) or by flow plots (during the progression of blackout). Errors in flows were calculated for both steady state simulation and dynamic simulation by comparing the results from simulation with actual measurements reported in [89]. Average errors achieved in MVA flows for steady state and dynamic simulation were 4.51% and 8.27% respectively. Also the simulation team were able to get relay trippings as reported in [89] for most of the cases with few exceptions. This concludes that the simulation faithfully followed the different stages of actual blackout event and can therefore be used as an excellent testbed for testing different strategies.

The zone 3 trippings took place in relays associated with Niland-Coachella Valley 161 kV transmission line and Elcentro-Pilotkon 161 kV transmission line. Both the transmission lines are under Imperial Irrigation District (IID). So, area under IID was chosen to test W_{25}. Time synchronized voltage and angle measurements for the buses under IID were read out from the simulated file and W_{25} was constructed. It should be clarified here that W_{25} is calculated between each incoming sample and the sample corresponding to steady state at the beginning of the simulation.

3.5. Observations from the New-England Test System

In order to analyze the effect of different system wide disturbances on the transmission line component energy function W_{25}, an $(n-1)$ contingency analysis was performed on test system 3.3. These included considering important components of the power system that have been prone to contingencies during the event of a cascading failures. A wide range of phenomenon allows to monitor all the corresponding changes to the energy function component.

3.5.1. Fault Sensitivity of W_{25}

The events shown in Table 3.2 were simulated at t=2s, in a total simulation window of t=30s. System conditions tested for include: line faults, generator failures, and significant changes in loading conditions. Fig. 3.4(a) shows the base-case where no faults have been applied and the system is at steady state condition.

Table 3.2. Events Simulated on Test System 3.3

Fault Type	Location (at t=2s)	Duration (cycles)	ΔW_{25} (pu)
Temporary 3ϕ fault	Bus 25-26	12	4.59
	Bus 1-2	6	**5.05**
Permanent 3ϕ fault	Bus 28-29	-	**6.59**
	Bus 22-23	-	4.04
Generator excitation failure	Gen 9	6	0.34
Generator power loss	Gen 8	-	0.49
Load addition	Bus 28	6	0.24

Figs. 3.4, 3.5 depict the transient changes in W_{25} before, during, and after the fault. It can be observed from Fig. 3.4 that the permanent 3ϕ fault on the transmission line connecting bus 28-29 shows maximum deviations from steady-state condition. During this fault, ΔW_{25} reaches a
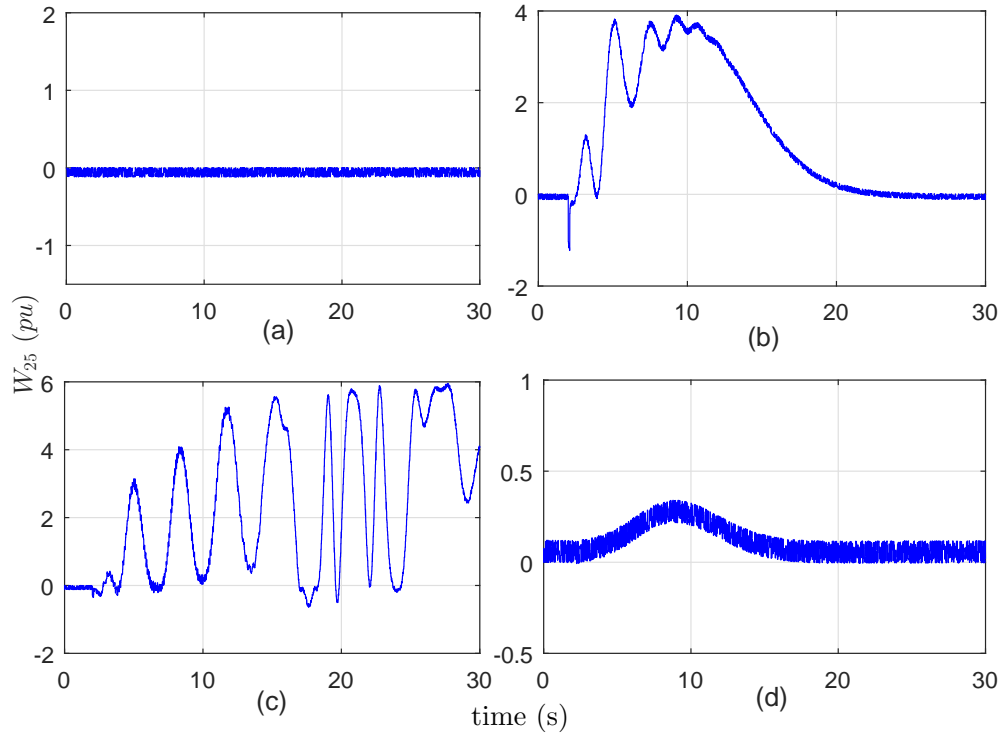
Figure 3.4. Change in P.E. component W_{25} in test system 3.3, subject to (a) without fault applied (b) temporary 3ϕ fault on line connecting bus 1-2 in Fig.3.2 (c) permanent 3ϕ fault on line connecting bus 28-29 in Fig.3.2 (d) generator 9 excitation failure in Fig.3.2
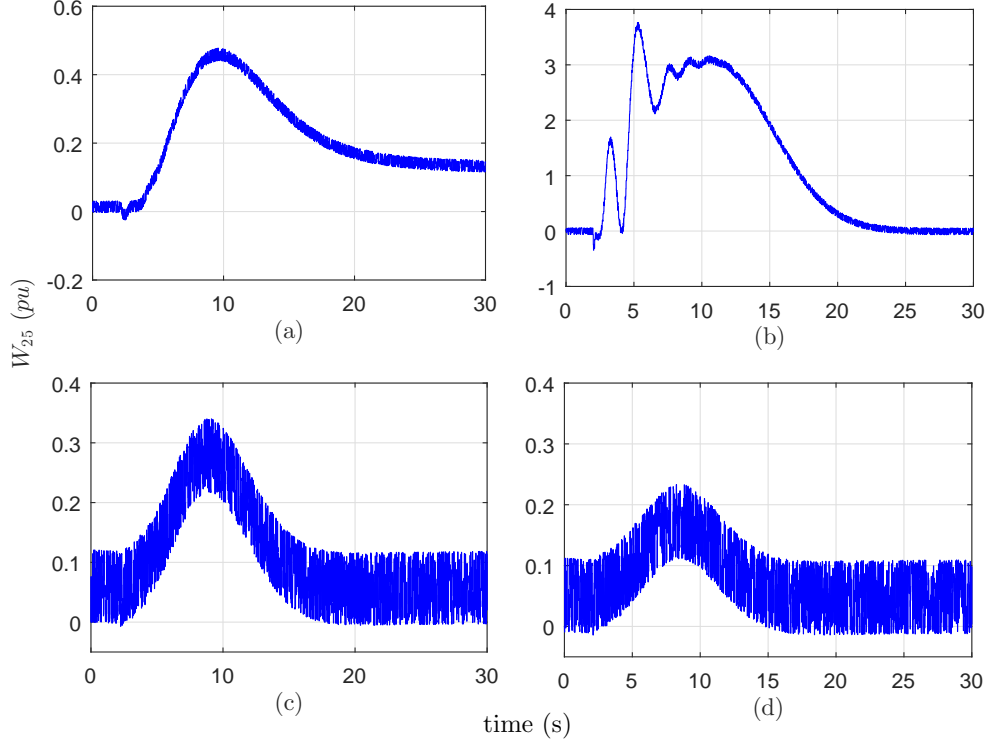
Figure 3.5. Change in P.E. component W_{25} in test system 3.3, subject to (a) generator 8 outage in Fig.3.2 (b) permanent 3ϕ fault on line connecting bus 22-23 in Fig.3.2 (c) generator 9 excitation failure in Fig.3.2 (d) load change on bus 28 in Fig.3.2

maximum variation of **6.59** pu, whereas for the generator #9 excitation failure, ΔW_{25} is around **0.34** pu.

Fig. 3.5 shows the variation of W_{25} with respect to another set of outages, shown in Table 3.2, for test system in section 3.3. It can be observed that even in case of the outage of generator #8, ΔW_{25} changes to **0.49** pu, whereas for the permanent 3ϕ fault on transmission line connecting bus 22-23, ΔW_{25} deviates to **4.04**, which is quite significant with regard to other events in the system. A temporary 3ϕ, 6-cycle fault also renders ΔW_{25} to **5.05**. It makes sense to choose W_{25} as a lead for further studies in the stressed power system for preventive measures.

3.5.2. Relay Misoperation Scenario

Area #3, in Fig. 3.2, spanning bus 29, 28, 26, and 27 was chosen as a subsystem from NETS. A distance relay was considered at bus 29, and the corresponding zones of protection were identified for testing the scenario of actual fault in zone 3, as compared to a relay misoperation in the same zone of the relay. A 3ϕ, 6-cycle, temporary fault was created on the line connecting buses

39

Table 3.3. W_{25} at Different Locations of Zone 3 of Relay

Zone 3 distances (km)	Bus location	W_{25} (p.u.) peak value	
		Temporary 3ϕ fault	Relay misoperation
75	26-28	4.14	0.10
90	26-28	4.83	0.15
100	26-27	5.78	0.17

26-28, in zone 3 of the relay. The outcome of a relay misoperation was simulated by disconnecting the transmission line by opening the breakers. The details of the zones in the subsystem are shown in Table 3.3. Fig. 3.6 (a) indicates the change in W_{25} due to the fault is very high as opposed to relay misoperation. Two similar scenarios were simulated in zone 3 of the relay, as shown in Fig. 3.6 (b), but further away from the previous distance. We observe that W_{25} peaks instantly after the fault is simulated, whereas the relay misoperation shows comparatively lesser deviation, as shown in Table 3.3. It should also be pointed out that W_{25} shows significant changes with respect to different locations in zone 3 of the relay, for both the events.

3.6. Observations from the WECC System

From Figure 3.7, it is evident that the value of W_{25} is changing in response to different system disturbances while the blackout was progressing. The value of energy function changed from 2.378
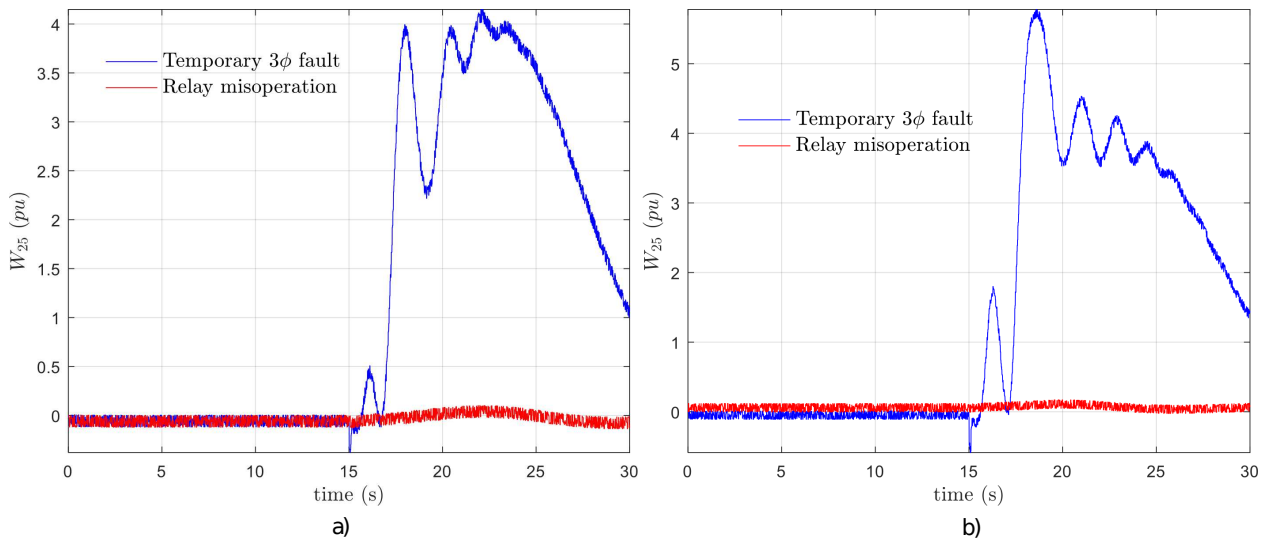
Figure 3.6. Change in W_{25} subject to temporary 6-cycle, 3ϕ fault and relay misoperation between (a) bus 26-28, (b) bus 26-27 in fig. 3.2, simulated at t=15s.
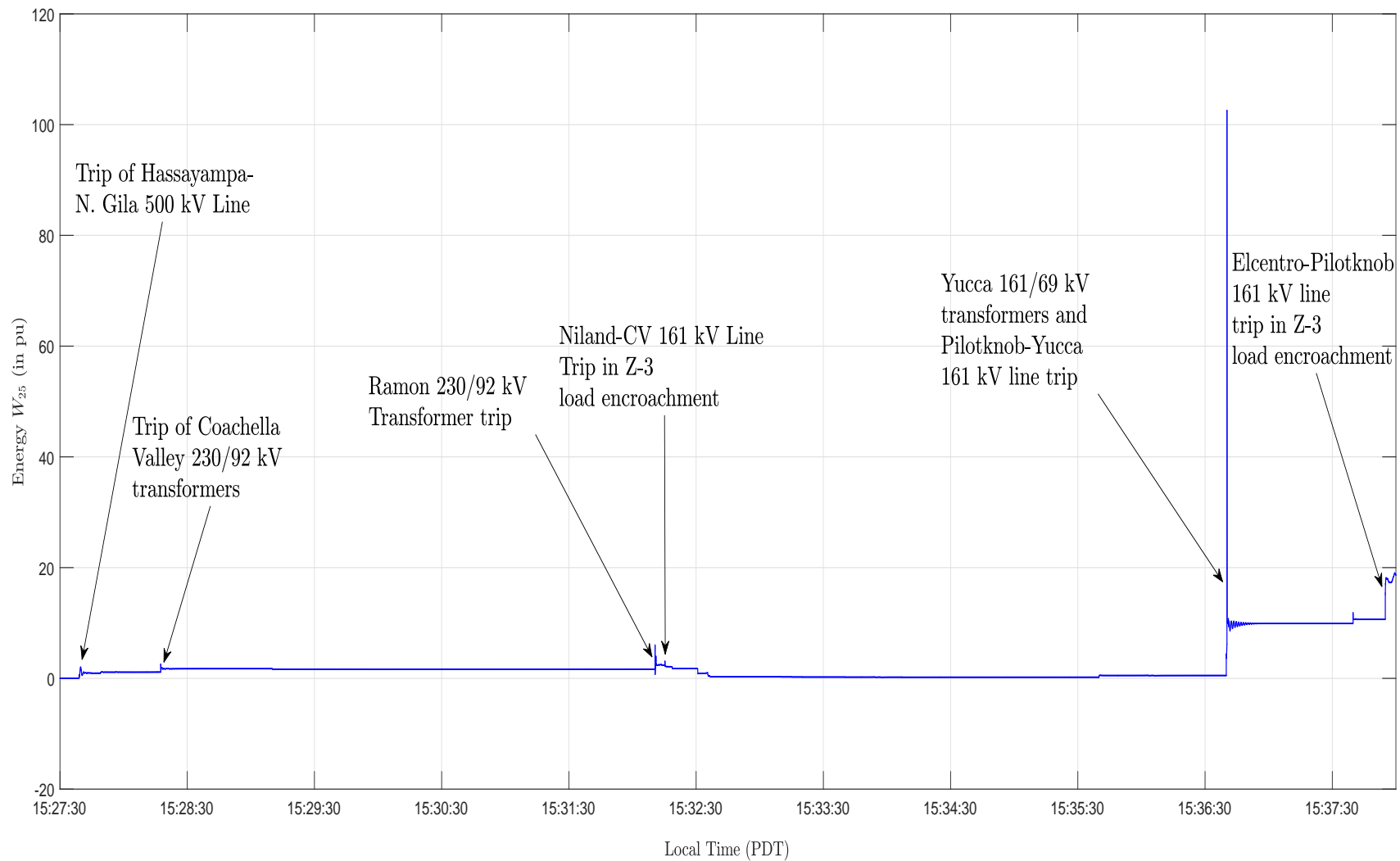
Figure 3.7. Transmission line energy function W_{25} plot in IID until islanding

pu before line-trip to 3.104 pu after line-trip when the Niland-Coachella Valley 161 kV line tripped on load encroachment around 15:32:14 local time - a change of **0.726** pu. In a similar fashion, W_{25} changed from 10.69 pu to 18.19 pu (change of **7.5** pu) as a result of Elecentro- Pilotknob 161 kV line trip under zone 3 load encroachment around 15:37:54 local time.

To check how the value of W_{25} changes when the system is experiencing an actual fault, three-phase faults were simulated in zone 1, zone 2 and zone 3 around the same time the lines tripped during the blackout event. Table 3.4 tabulates the changes in W_{25} (ΔW_{25}) under these fault scenarios, calculated as the difference in value of W_{25} during fault and the value of W_{25} before fault. The tabulated values reveal that ΔW_{25} is higher when there is an actual fault, than for a load encroachment event. So, it is evident that W_{25} is more sensitive to system faults.

Table 3.4. ΔW_{25} under Different Scenarios

Facility Name 161 kV lines	Change of W_{25} (in pu) under			
	Load Encroachment	Zone 1 Fault	Zone 2 Fault	Zone3 Fault
Niland-Coachella Valley	**0.726**	1.077	2.266	2.369
Elcentro-Pilotknob	**7.5**	7.64	7.82	8.22

Though ΔW_{25} is very sensitive under fault conditions than for the two load encroachment events, from Fig. 3.7 it can be seen that there were other events when some transmission facilities tripped due to overload (load was more than settings of over current relays), and ΔW_{25} was much higher than for the events discussed above. For example, the highest ΔW_{25} in the blackout event was 102.08 pu which occurred when Pilotknob Yucca 161 kV transmission line and Yucca 161/69 kV transformers tripped around 15:36:40 local time due to overcurrent. Similarly there are other events, where a likely trend is seen.

Alongside the line event, W_{25} in IID was also tested against generation loss and load loss events. The simulation was performed in the system just before the initiation of the blackout. After running the simulation for 30 s in the healthy system, a generator inside IID producing 90 MW of
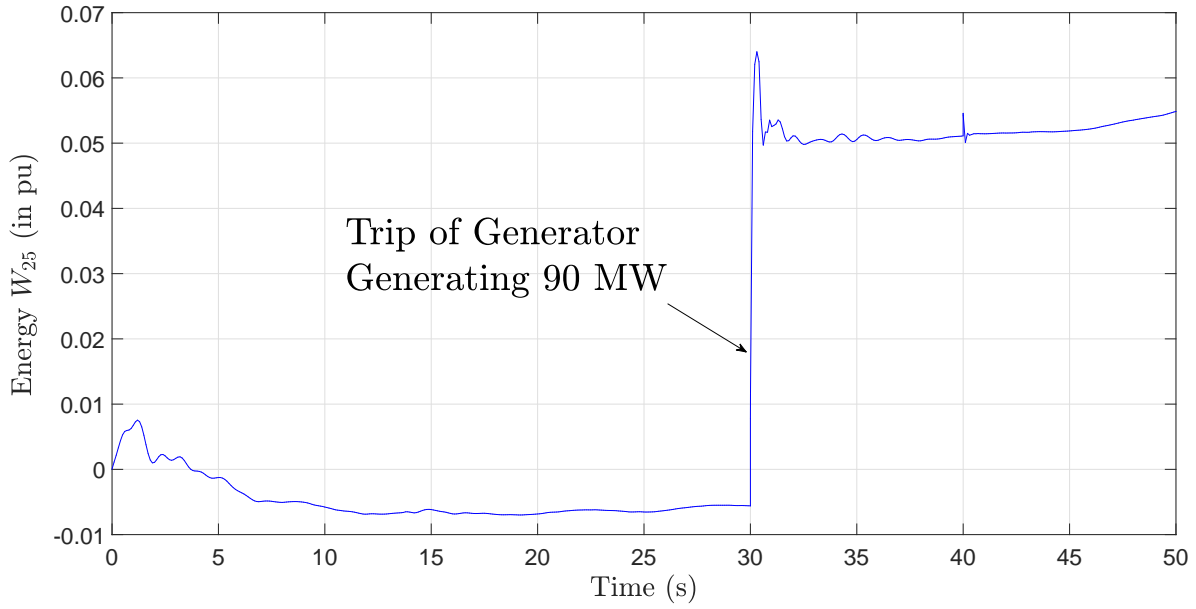
Figure 3.8. W_{25} Plot in IID subjected to generation loss

real power was tripped. Figure 3.8 shows the plot of W_{25} for this generation loss event. The value of W_{25} changed from (-0.006) pu to 0.064 pu following the generator loss ((ΔW_{25}) = 0.07 pu). In a similar manner another simulation was run and this time 100 MW of load inside IID was taken out at 30th second. The corresponding change in W_{25} in this case was -0.19 pu as shown in Fig. 3.9. It
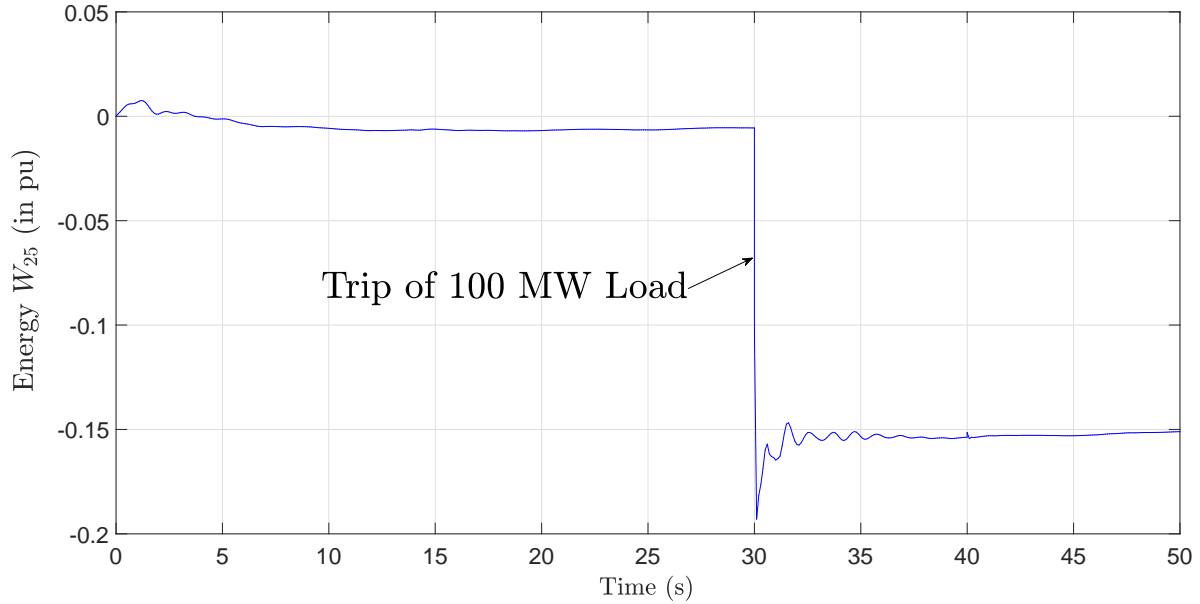
Figure 3.9. W_{25} Plot in IID subjected to load loss

can be inferred that compared to changes in W_{25} for line events, load events and generator events exhibit negligible changes in W_{25}.

3.7. Summary

In this chapter, we explore a novel approach based on energy functions to monitor the future operation of distance relays, motivated by the critical role they have been known to play during blackouts. Our key contribution lies in the observation that the energy function sub-component (W_{25}) is a sensitive metric to discriminate between faults and load encroachment during stressed conditions. We track and study the sensitivity of this metric to different system conditions including generator faults, line faults, and loading conditions. Simulation results are presented on the 39 bus NETS model and a portion of the WECC system for faults in zone 1, 2, and 3 of distance relays, in stressed conditions and during a cascading blackout sequence. Since this metric is independent of relay settings, it can be potentially be used as an alternative index to monitor and supervise the actions of distance relays in response to critical system events.

4. ROBUST DAMPING OF INTER-AREA OSCILLATIONS IN AC-MTDC GRIDS USING H_∞ MIXED-SENSITIVITY APPROACH

This chapter is based on the work "Robust Damping of Inter-area Oscillations in AC-MTDC grids using H_∞ Mixed-Sensitivity Approach," *2016 IEEE Power and Energy Society General Meeting (PESGM)*, Boston, MA, 2016, pp. 1-5. (doi:10.1109/PESGM.2016.7742013) [93]. The authors of the paper are A. Banerjee [1], N. R. Chaudhuri.

4.1. Introduction

Voltage Source Converter (VSC) technology-based Multiterminal DC (MTDC) grids has shown significant promise in interconnecting offshore wind resources to the onshore grid around the world. In the recent past, a lot of research attention has been paid to modeling [94, 95] and control [96, 97] of MTDC grids interconnected to multi-machine AC systems. The operators of these AC systems with multiple areas typically face the challenges of stabilizing poorly-damped inter-area oscillations. It is imperative that the MTDC grids connected to these AC systems should provide damping contribution through supplementary control action. Only a few papers [98, 99, 100] have so far reported research on this topic. Reference [98] focused on the design of converter droop gains in a multivariable framework to reduce the impact of converter pole outage on the oscillatory modes of the surrounding AC system. Reference [100] proposed a control structure for MTDC grids for damping inter-area oscillations and Preece et-al [99] proposed a modal linear quadratic Gaussian (MLQG) structure for achieving that goal. However, none of these papers considered robust damping controller design that will demonstrate acceptable performance when major events like converter pole outage or AC line outage take place. The objective of this contribution is to fill in this gap.

In this chapter, a robust damping controller design for the MTDC grid based on H_∞ mixed-sensitivity formulation in the Linear Matrix Inequality (LMI) framework is presented, which demon-

---

[1]Abhishek Banerjee was the first author and responsible for writing the manuscript and applying simulation tests. Dr. Nilanjan Ray Chaudhuri served as the proofreader and gave recommendations and guidance on drafting the paper.

strates acceptable oscillation damping performance in the surrounding AC system following converter pole outages and AC line outages. Favorable results are demonstrated in a 6-machine and a 16-machine AC system connected to a 4-terminal asymmetric bipolar DC grid.

4.2. Modelling and Control of MTDC Grid

In this design, an asymmetric bipolar VSC-MTDC grid is considered, which has a +ve pole, a -ve pole, and a metallic return network. Figure 4.1 shows the ith converter station of the MTDC grid. The parameters of the ith converter station are denoted with a subscript i, and the +ve (-ve) pole is denoted by a superscript $p(n)$. The cables connecting the MTDC converter stations are modeled using a single pi-section.
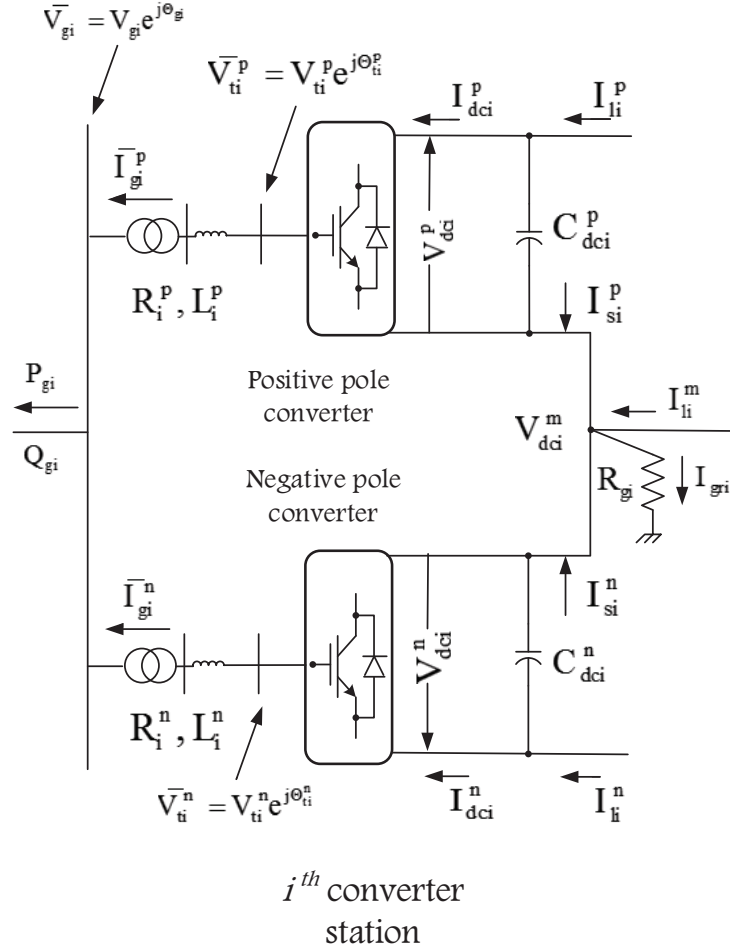
Figure 4.1. The ith converter station of the MTDC grid.

As shown in Fig. 4.2, the converter stations are assumed to operate under active power – common DC link voltage droop control where the error in the square of a *common* DC voltage V_{dc_comm} is drooped against the power error i.e, the difference between the reference and the measured power. In this case the DC link voltage from a common converter station is communicated to the other stations. A PI controller derives the d-axis current reference I_{gX}^{p*} for the inner current control loop of the +ve pole converter. The converter stations are modeled and controlled using well-known decoupled vector control strategy in the $d - q$ frame and are not repeated here. Interested readers can get further details of modeling and control in [44].
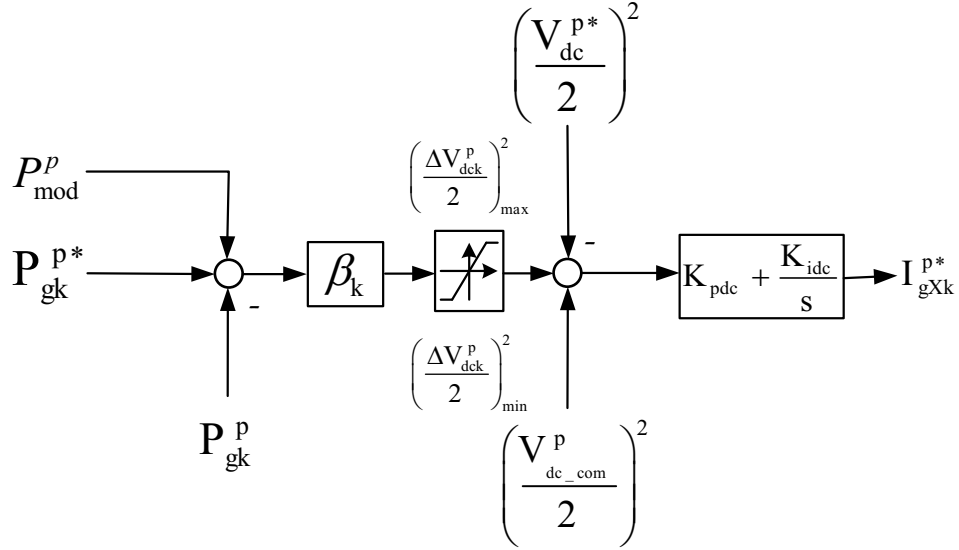
Figure 4.2. Active power-DC link voltage droop control for the +ve pole of the kth converter station. Identical control is used for the -ve pole.

4.3. Test Systems

The MTDC grid consists of four converter terminals, which were interconnected to different AC systems which have been described next.

4.3.1. Test System I: MTDC Grid in 6-Machine System

Figure 4.3 shows the single-line diagram of the asymmetric bipole MTDC grid connected to a 6-machine AC system. The AC system consists of three asynchronous grids. The converter stations operate in droop control mode shown in Fig. 4.2 with station #1 as the common converter. The

approximate values of MW flows through the converters are shown in Figure 4.3. The converters maintain unity power factor at the PCC. Further details can be found in [44].
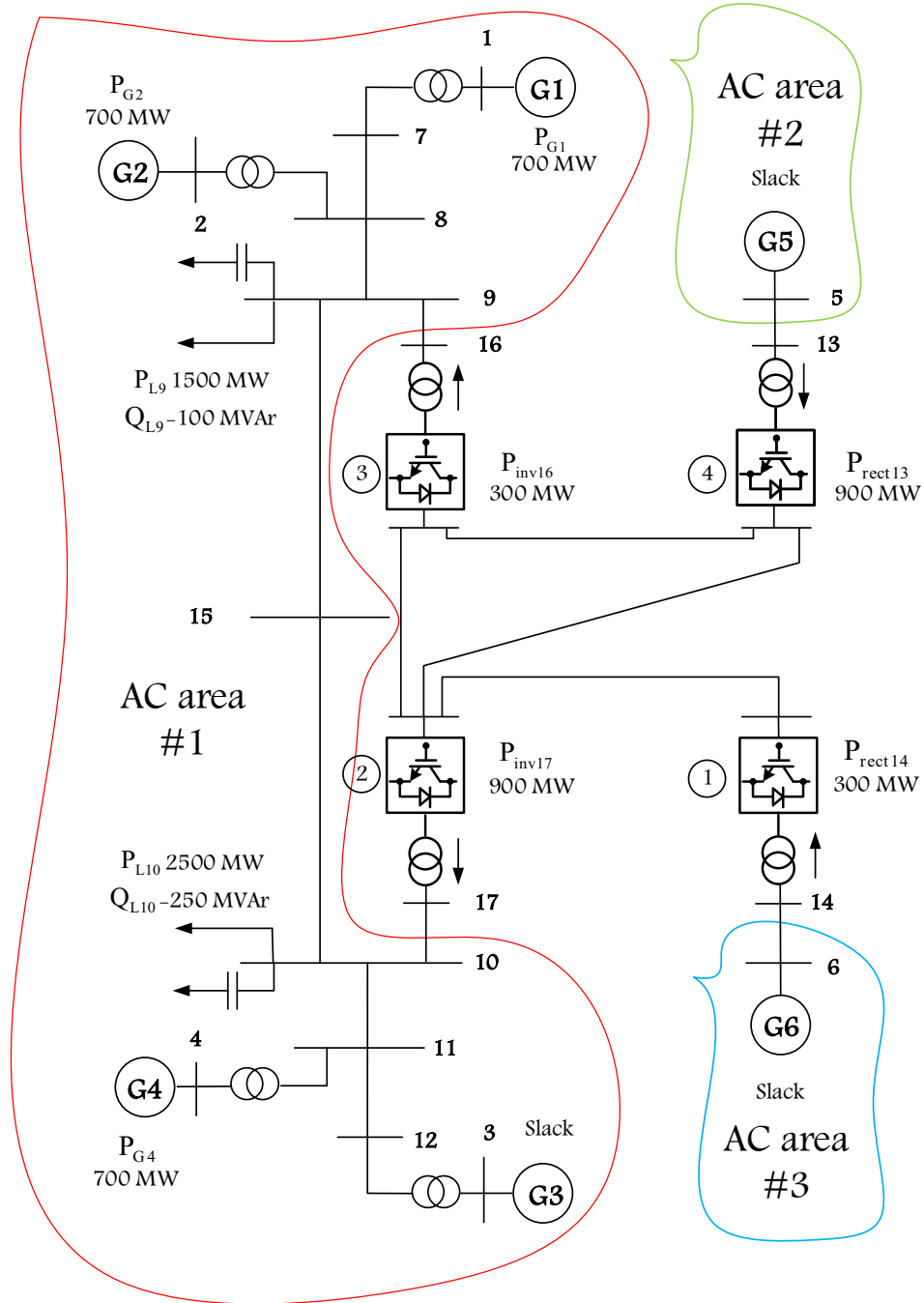
Figure 4.3. Asymmetric Bipole MTDC grid (single line diagram) connected to a 6-machine AC system.

4.3.2. Test System II: MTDC Grid in 16-Machine System

A 16-machine test system [52] is considered with an asymmetric bipolar 4-terminal MTDC grid connecting the New England Test System (NETS) and New York Power System (NYPS) areas as shown in Fig. 4.4. The nominal real and reactive powers at the PCC of the converter stations are marked in this figure.
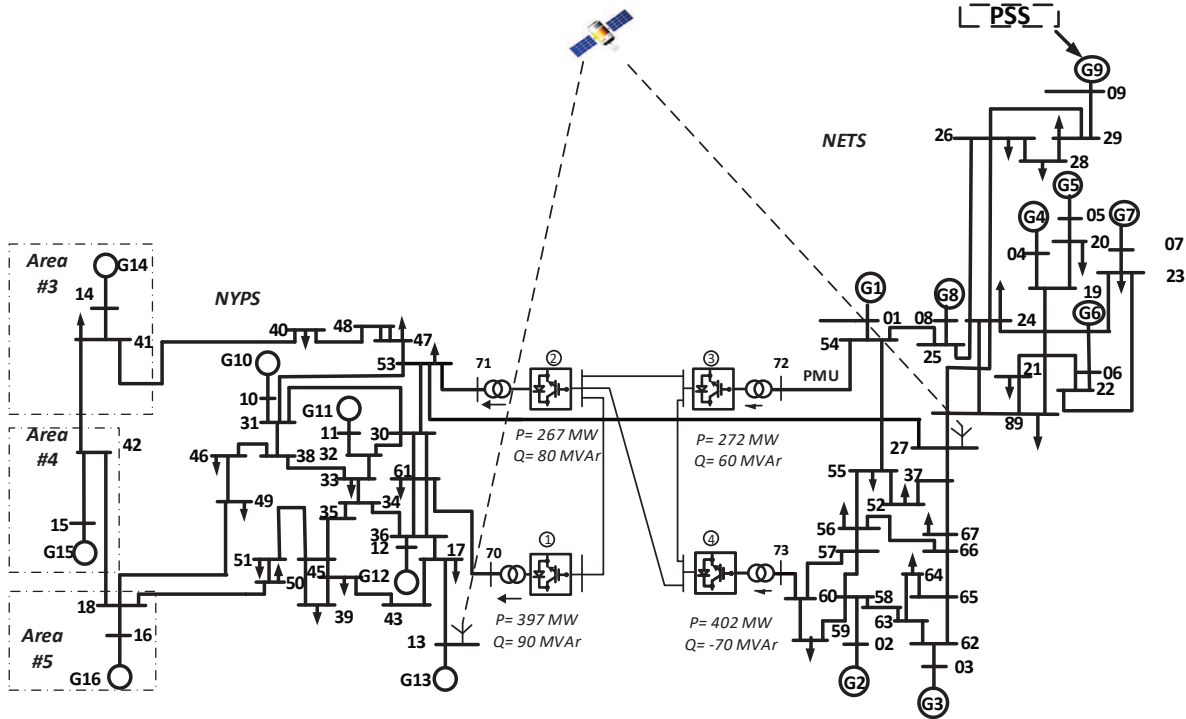
Figure 4.4. Asymmetric Bipole MTDC grid (single line diagram) connected to 16-machine AC system.

4.4. Power Oscillation Damping Using MTDC Converter Controls

Test system I, has one poorly damped 0.57-Hz inter-area mode with 0.7% damping as mentioned in Section 4.3.1. Test system II in Section 4.3.2 has three poorly-damped inter area modes as shown in Table 4.1. The fourth mode has a settling time of $16s$, which is considered to be well-damped. The real power reference in the MTDC converter stations can be modulated using the control input P_{mod}, shown in Fig. 4.2 for damping these inter-area modes. The damping controller design is described in the next Section.

4.5. Design Formulation: H_∞ Mixed Sensitivity-Based Approach

The translation of the mixed sensitivity problem into a generalized H∞ problem has been reported in [49], which is described here. The mixed sensitivity approach is used to minimize the effects of the disturbance on the system and to limit the control effort. The sensitivity function $S = (I - GK)^{-1}$ is shaped with one or more transfer functions such as KS or complementary sensitivity function, $T = I - S$. In power systems, oscillations occur due to the sudden variations in load, converter outages etc. The damping controllers are designed to damp the oscillatory modes following a disturbance scenario. The mixed sensitivity formulation involves shaping S, i.e. the transfer function between the disturbances and the outputs and KS, i.e. the transfer function between the disturbances and the control signals. The disturbance d is a low frequency signal, so a scalar low pass filter $w_1(s)$ with a bandwidth equal to that of the disturbance is selected to find a stabilizing controller which minimizes $\|w_1 S\|_\infty$ whereas $w_2(s)$ is a scalar high pass filter with a crossover frequency approximately equal to that of the desired closed-loop bandwidth. Fig. 4.5 shows the mixed sensitivity block-diagram where $G(s)$ is the open-loop plant, $K(s)$ is the controller to be designed and W_1 and W_2 are the shaping filters.

To facilitate control design and to reduce the complexity of the controller, the nominal plant model can be reduced using model reduction techniques [49, 52]. The reduced order plant should
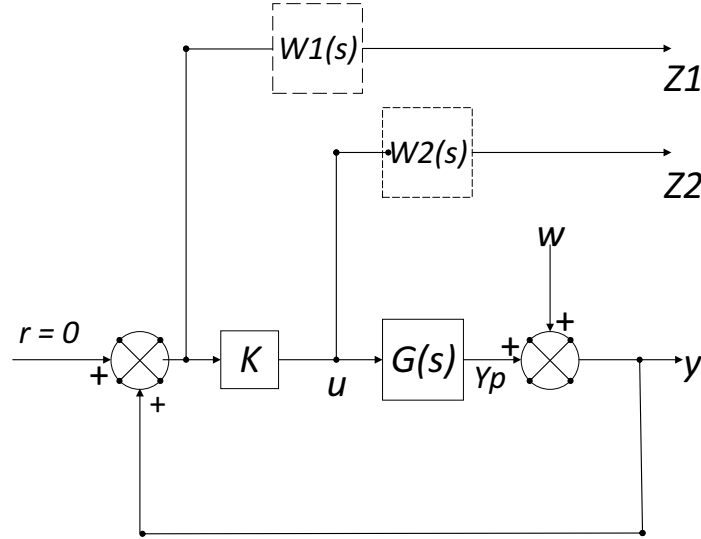
Figure 4.5. Mixed sensitivity block diagram.

closely resemble the orignial plant's response in the frequency range of interest. The weighing filters are important for shaping the closed loop quantities. For disturbance rejection ability at low frequencies, a scalar low pass filter with bandwidth equal to that of the disturbances is selected and for minimizing the control effort at higher frequencies, a high pass filter W_2 , with a crossover frequency approximately equal to the desired closed loop bandwidth is chosen. The performance specifications [49] of the weighing filters can be stated as

$$
\begin{aligned}
&|S(j\omega)| < 1/\left|w_1(j\omega)\right|, \forall\omega \\
&\Leftrightarrow |w_1 S| < 1, \forall\omega \Leftrightarrow \|w_1 S\|_\infty < 1
\end{aligned}
\tag{4.1}
$$

$$
\begin{aligned}
&|KS(j\omega)| < 1/\left|w_2(j\omega)\right|, \forall\omega \\
&\Leftrightarrow |w_2 KS| < 1, \forall\omega \Leftrightarrow \|w_2 KS\|_\infty < 1
\end{aligned}
\tag{4.2}
$$

The mixed sensitivity (S/KS) design objective is represented as (4.3)

$$
\left\| \begin{bmatrix} W_1(s)S(s) \\ W_2 K(s)S(s) \end{bmatrix} \right\|_\infty < 1
\tag{4.3}
$$

The state space representation of the augmented plant [49], [52] is given by (4.4)

$$
\begin{bmatrix} \dot{x} \\ z \\ y \end{bmatrix} = \begin{bmatrix} A & B_1 & B_2 \\ C_1 & D_{11} & D_{12} \\ C_2 & D_{21} & 0 \end{bmatrix} \begin{bmatrix} x \\ d \\ u \end{bmatrix}
\tag{4.4}
$$

where,

x: state variable vector of the power system,

w: disturbance input,

u: control input (output of the damping controllers)

y: measured output (e.g. power flow, line current, bus voltage etc.),

z: regulated output

The state-space realization of the controller is given by (4.5)

$$\dot{x}_k = A_k X_k + B_k y$$
$$u = C_k X_k + D_k y$$

(4.5)

where x_k represents the controller states, u controller output and y plant output. The transfer matrix between the disturbance and the regulated output is given by (4.6)

$$T_{zd}(s) = \begin{bmatrix} W_1(s)S(s) \\ W_2 K(s)S(s) \end{bmatrix} = C_{cl}(sI - A_{cl})^{-1}B_{cl} + D_{cl}$$

(4.6)

where,

$$A_{cl} = \begin{bmatrix} A + B_2 D_k C_2 & B_2 C_k \\ B_k C_2 & A_k \end{bmatrix}$$

$$B_{cl} = \begin{bmatrix} B_1 + B_2 D_k D_{21} \\ B_k D_{21} \end{bmatrix}$$

(4.7)

$$C_{cl} = \begin{bmatrix} C_1 + D_{12} D_k C_2 & D_{12} C_k \end{bmatrix}$$

$$D_{cl} = D_{11} + D_{12} D_k D_{21}$$

The real bounded lemma [101], applying the Schur's formula for the determinant of a partitioned matrix [49], there exists an $X = X^T > 0$ [49] for which the closed loop system in (4.6) achieves asymptotic stability, such that

$$\begin{bmatrix} A_{cl}^T X + X A_{cl} & B_{cl} & X C_{cl}^T \\ B_{cl}^T & -I & D_{cl}^T \\ C_{cl} X & D_{cl} & -I \end{bmatrix} < 0.$$

(4.8)

The existence of $X = X^T > 0$ in (4.8) ensures guarenteed asymptotic stability with $\|T_{zd}\|_\infty < 1$ [49], [52]. Hence, solution to this LMI leads to the controller design. Due to the existence of controller states in the LMI problem in (4.8), it becomes non-linear in nature and hence a change of variables is required to linearize it. [49], [101] To implement this, the new controller variables are

given by (4.9), where R, S, M, N are submatrices of X [102], [103]:

$$\hat{A} = NA_kM^T + NB_kC_2R + SB_2C_kM^T$$
$$+S(A + B_2D_kC_2)R$$
$$\hat{B} = NB_k + SB_2D_k \quad\quad\quad\quad\quad (4.9)$$
$$\hat{C} = C_kM^T + D_kC_2R$$
$$\hat{D} = D_k$$

The design problem transforms to linearized problem where a solution is required for the following

$$\begin{bmatrix} R & I \\ I & S \end{bmatrix} > 0 \quad\quad\quad\quad\quad (4.10)$$

$$\begin{bmatrix} \Psi_{11} & \Psi_{21}^T \\ \Psi_{21} & \Psi_{22} \end{bmatrix} < 0 \quad\quad\quad\quad\quad (4.11)$$

where the elements of (4.10)-(4.11) are presented in [104]. The LMI's in (4.10)-(4.11) are solved first for $\hat{A}, \hat{B}, \hat{C}$ and $\hat{D}$ as an optimization problem. By solving (4.9), A_k, B_k, C_k and D_k are obtained from the solution of $\hat{A}, \hat{B}, \hat{C}$ and $\hat{D}$.

In addition to achieving $\|T_{zd}\|_\infty < \gamma$ for guarenteed robustness [49], another design criterion for power oscillation damping is to place the closed loop poles of the critical modes within a conic sector with inner angle θ and the apex at the origin to ensure minimum damping ratio $\zeta_{min} = cos^{-1}\frac{\theta}{2}$ for the closed loop poles [104],[105].

4.6. Simulation Results

4.6.1. Test System I: MTDC Grid in 6-Machine System

Based on residue magnitude-angle criteria [106], two feedback signals, real power output of $G3$ and $G4$ (Fig. 4.3) are chosen, while the +ve and the -ve pole converters of station #2 are used as the actuators. The nominal plant model was reduced to a 9th order equivalent using the Schur
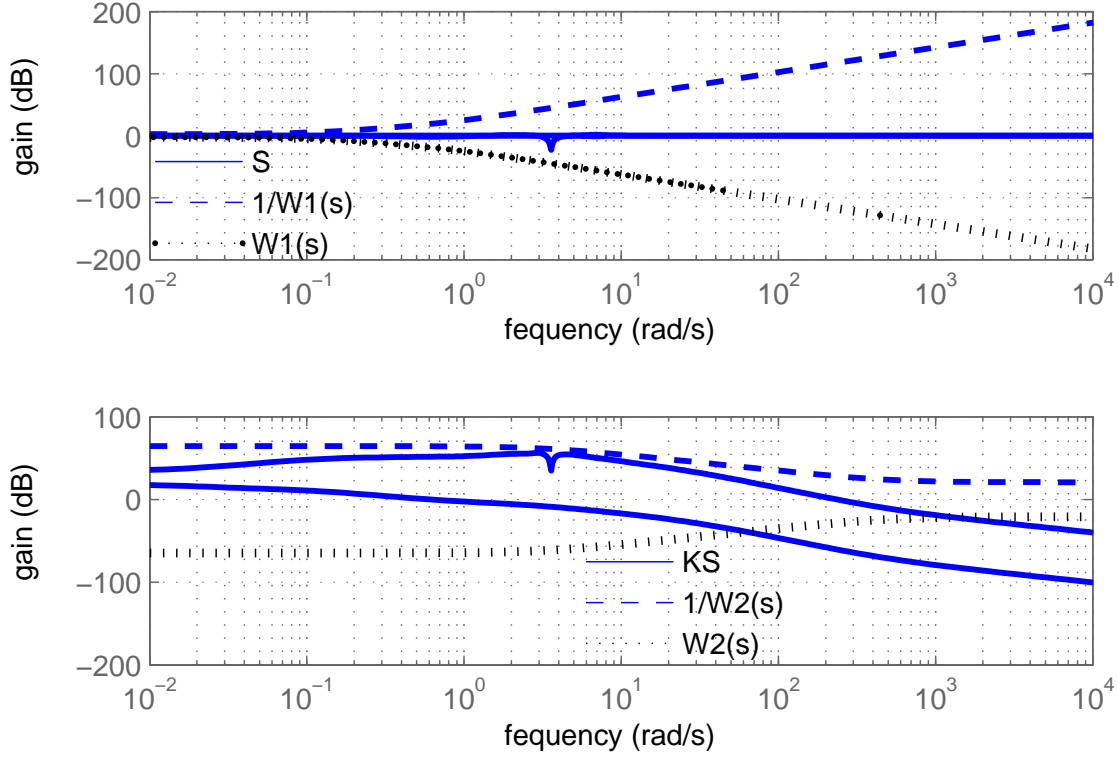
Figure 4.6. Frequency response of S, KS, and the weighing filters.

balanced truncation [49]. The filter parameters were selected as:

$$W_1 = \frac{0.075}{s^2+s+0.1}, W_2 = \frac{0.09s+0.295}{s+500} \tag{4.12}$$

The LMI optimization was performed using the multi-objective function $hinfmix$ in the Robust Control Toolbox in MATLAB to design the controller. A settling time of $15s$ for the 0.57-Hz mode was achieved. The frequency response of S, KS, and the weighing filters are shown in Fig. 4.6. The dynamic performance of the system following the outage of the -ve pole of converter station #3 is depicted in Figure 4.7. It can be clearly observed that the controller design is robust to such a large change in system operating condition and the oscillations settle within 15s.

4.6.2. Test System II: MTDC Grid in 16-Machine System

Based on residue magnitude-angle criteria [106], two feedback signals were chosen: real power flowing through lines connecting buses 13 and 17 (i.e. $P(13-17)$) and buses 17 and 53 (i.e.
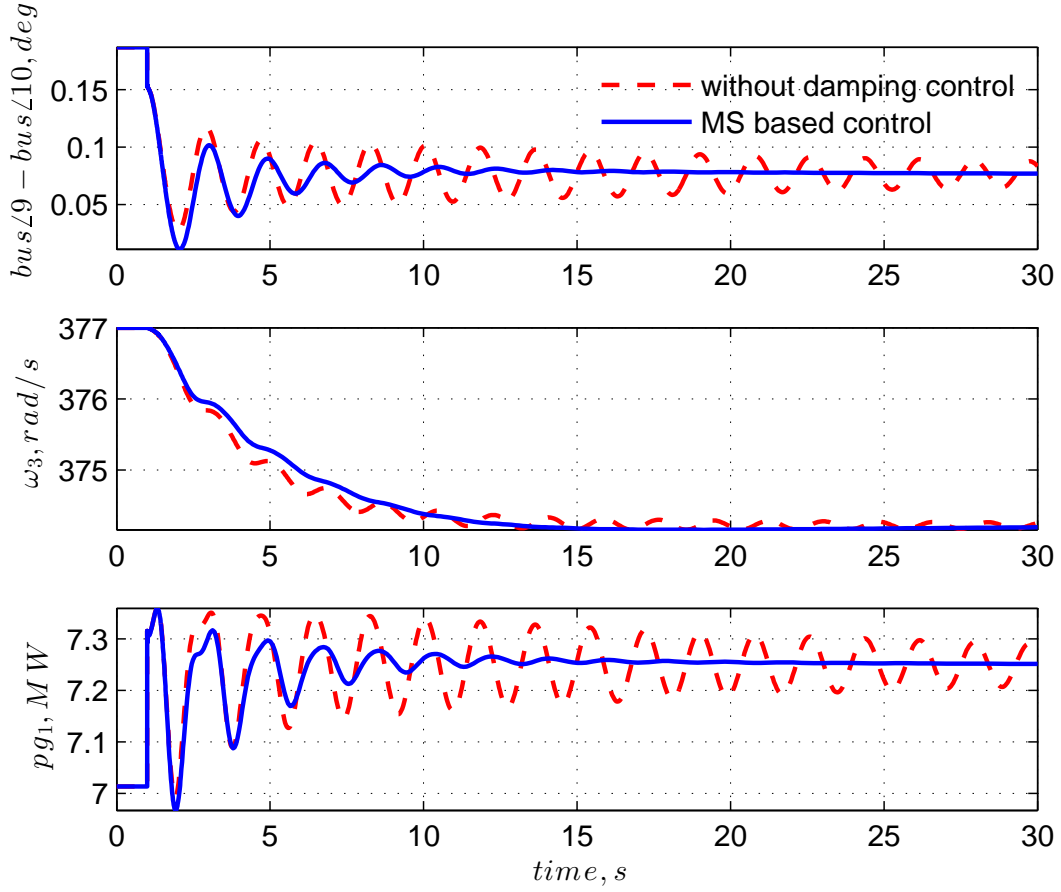
Figure 4.7. Dynamic performance of the system following the outage of the -ve pole of converter station #3 at $t = 1s$. MS based control: performance with H_∞ Mixed Sensitivity based damping controller.

$P(27 - 53))$, respectively, see Fig. 4.4. The +ve and the -ve pole converters of station #2 are used as the actuators. Schur balanced truncation method was used to reduced the system model and the frequency response of the original and the reduced system are show in Fig. 4.8.

The filter parameters were selected as:

$$W_1 = \frac{0.075}{s^2+s+0.1}, \quad W_2 = \frac{0.09s+0.345}{0.01s+430} \tag{4.13}$$

The LMI optimization was performed to design the controller that ensures placement of all closed-loop poles in a conic sector with a minimum damping ratio of 15%. It can be seen from Table 4.1 that a settling time of about $15s$ is achieved for all four inter-area modes. The frequency response of S, KS, and the weighing filters are shown in Fig. 4.9.
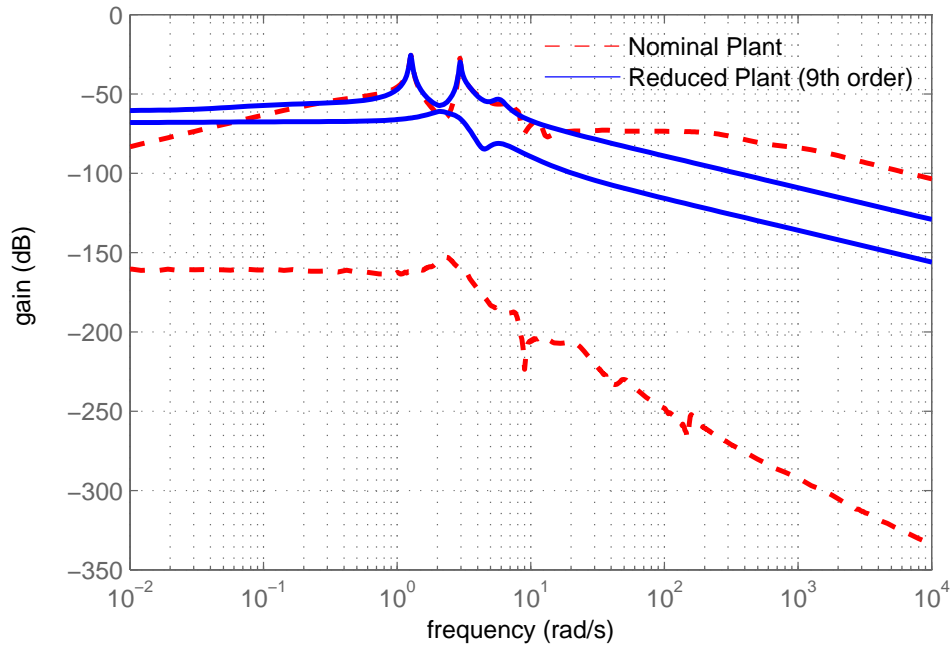
Figure 4.8. Frequency response of original and reduced-order plant of Test System II.
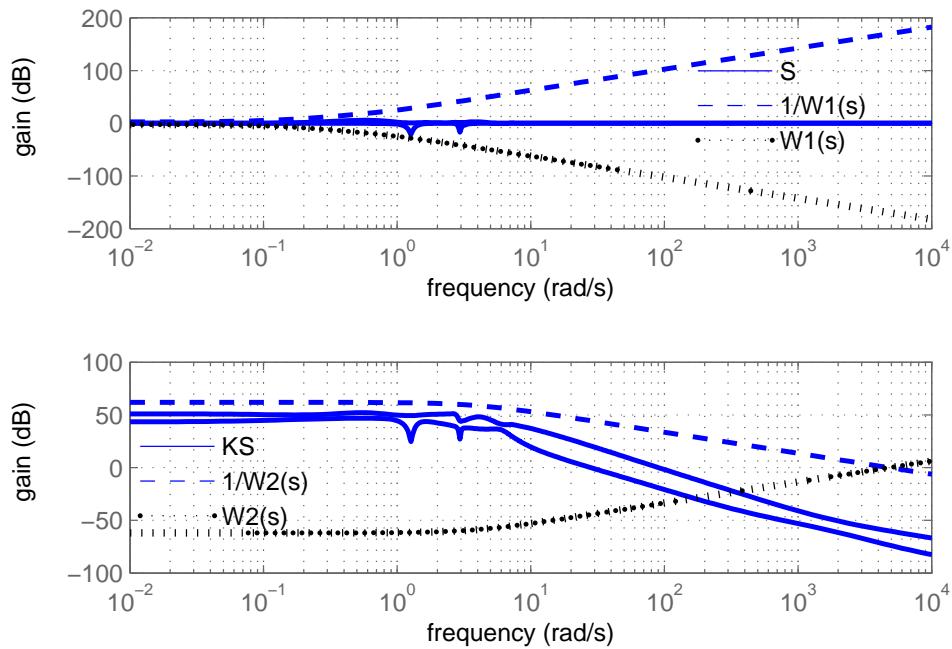
Figure 4.9. Frequency response of S, KS, and the weighing filters.
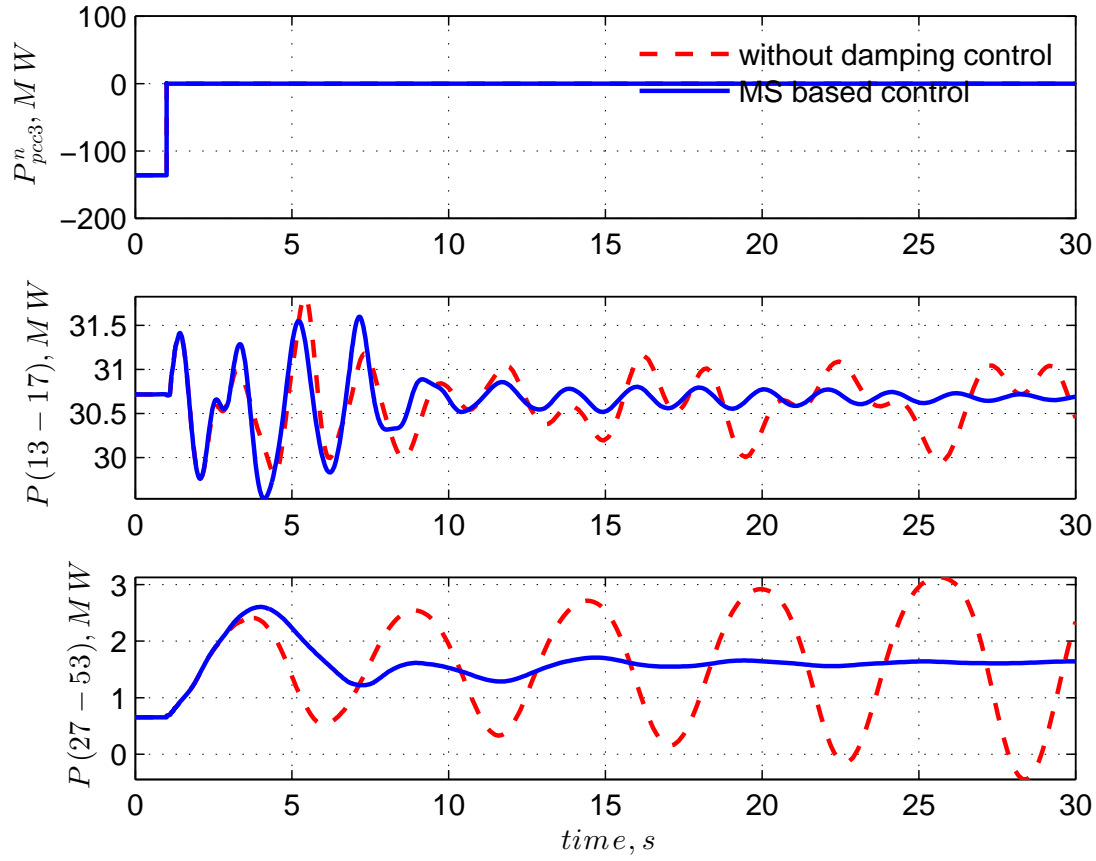
Figure 4.10. Dynamic performance of the system following the outage of the -ve pole of converter station #3 at $t = 1s$. MS based control: performance with H_∞ Mixed Sensitivity based damping controller.

It can be observed from Fig. 4.12 that the proposed damping controller can produce acceptable damping performance following a 5-cycle fault at bus #18 followed by the outage of one of the double-circuit lines connecting buses 18 and 49 in Fig. 5.8.

Table 4.1. Damping Ratios, Frequencies and Settling Times of the Inter-area Modes in Test System II

Mode no.	Open-loop			Closed loop		
	ζ	f, Hz	T, s	ζ	f, Hz	T, s
1.	0.016	0.202	193.001	0.202	0.216	**14.343**
2.	0.009	0.469	152.749	0.094	0.448	**15.023**
3.	0.044	0.515	28.220	0.076	0.493	**16.888**
4.	0.050	0.790	16.106	0.051	0.790	**15.795**
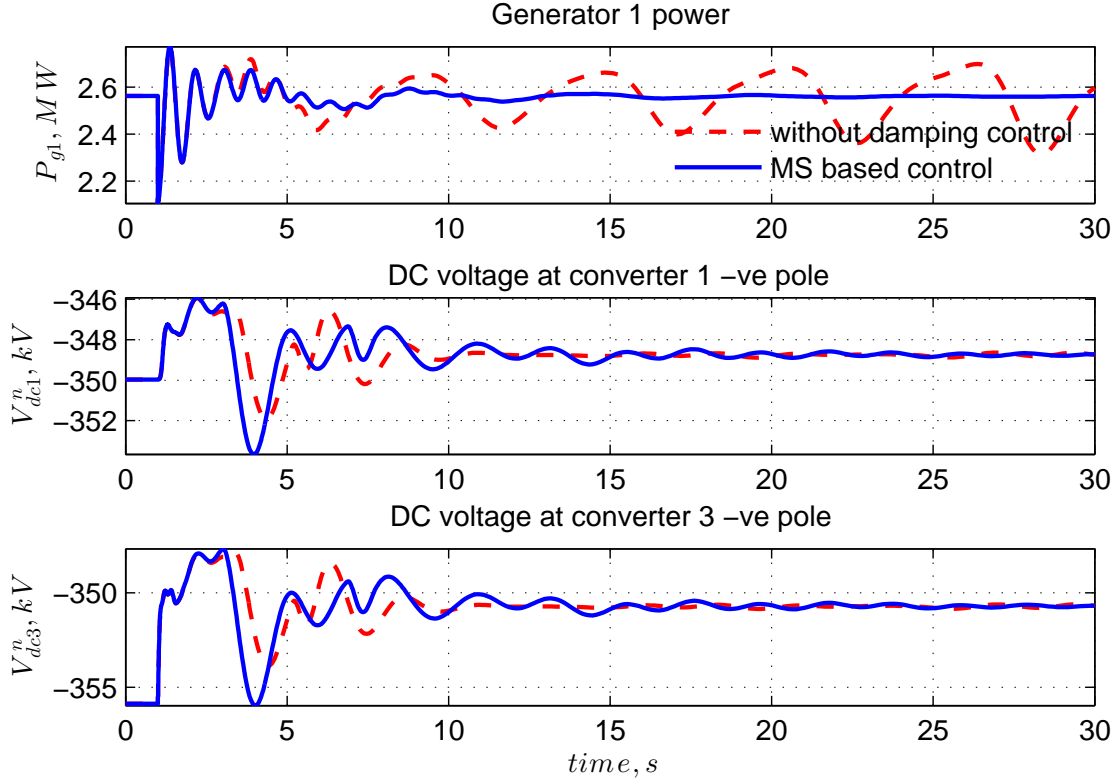
Figure 4.11. Dynamic performance of the system following the outage of the -ve pole of converter station #3 at $t = 1s$. MS based control: performance with H_∞ Mixed Sensitivity based damping controller.

Figures 4.10 and 4.11 show the dynamic performance of the system following the outage of the -ve pole of converter station #3 in Test system II (see Fig. 5.8). It can be seen that – (a) at $t = 1s$ the real power output of converter #3 -ve pole becomes zero; (b) the system becomes unstable in absence of any supplementary damping control, whereas the H_∞ Mixed Sensitivity based damping controller is able to damp the oscillatory modes in a reasonable time-frame. It can also be observed from Fig. 4.11 that the DC bus voltages at the converter stations with damping control do not reach unreasonably high or low magnitudes compared to the scenario without any damping control.

4.7. Summary

A robust power oscillation damping controller for MTDC grids connected to AC systems based on H_∞ mixed-sensitivity formulation in the LMI framework is proposed and designed in this chapter. The effectiveness of the robust design is validated through simulation results in a 6-machine
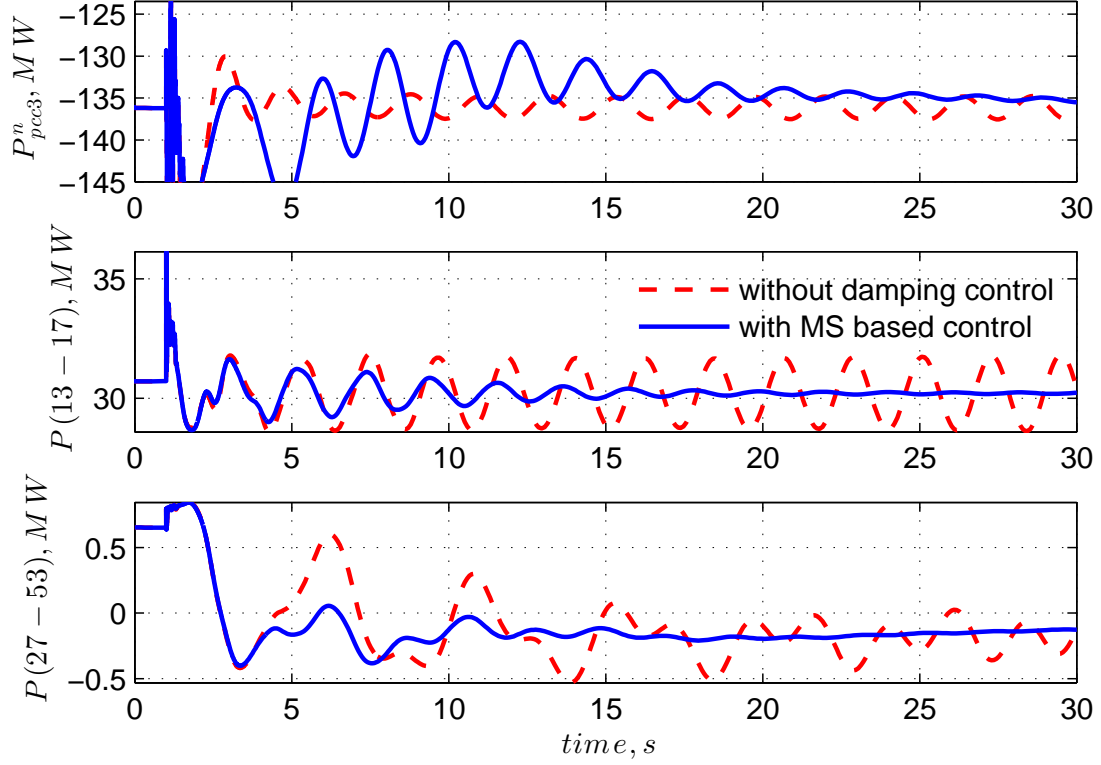
Figure 4.12. Dynamic performance of the system following a 5-cycle fault at bus #18 followed by the outage of one of the double-circuit lines connecting buses 18 and 49, Fig. 5.8, at $t = 1s$. MS based control: performance with H_∞ Mixed Sensitivity based damping controller.

3-area and a 16-machine 5-area system connected to a 4-terminal asymmetric bipolar MTDC grid. Acceptable dynamic performance is demonstrated following contingencies like converter pole and AC line outage. This opens up a new spectrum of enabling VSC stations to be used as actuators for supplementary damping control in AC-MTDC grids. It also substantiates the need to model AC as well as DC side disturbances for increased robustness to more severe contingency scenarios like actuator outages, feedback signal loss and communication latency. In order to address these exogenous disturbances have to modeled within the LMI framework of the existing H_∞ control scheme that has been described in the next chapter.

5. A NOVEL EXPLICIT DISTURBANCE MODEL-BASED ROBUST DAMPING OF INTER-AREA OSCILLATIONS THROUGH MTDC GRIDS EMBEDDED IN AC SYSTEMS

This chapter is based on the work "A Novel Explicit Disturbance Model-Based Robust Damping of Interarea Oscillations Through MTDC Grids Embedded in AC Systems," in *IEEE Transactions on Power Delivery*, vol. 33, no. 4, pp. 1864-1874, Aug. 2018. (doi: 10.1109/TP-WRD.2018.2799170) [107]. The authors of the paper are A. Banerjee [1], N. R. Chaudhuri and R. G. Kavasseri.

5.1. Introduction

Voltage Source Converter (VSC)-based Multiterminal DC (MTDC) grids are beginning to show significant promise in integrating offshore wind resources to onshore grids - thus attracting recent research attention towards modeling [94, 95] and control [96, 97] of such systems. In general point-to-point HVDC schemes suffer from certain issues, which can be overcome by an MTDC grid. As a result, such systems can also be beneficial for onshore installations. The advantages of MTDC grids include: (a) Improved reliability in face of a single-point failure, (b) Reduced capacity and reserve capacity requirement since the peak demand of different AC systems do not occur at the same time, (c) Reduced curtailment from wind farms, (d) reduced variability in renewable generation, ease of annual and preventive maintenance of the generators and the converter systems and energy trading between multiple regions like today's AC power systems, and (e) Lower energy cost. For further explanation on points (a) – (d), please refer to [108], and for point (e), please see [109],[110].

The operators of these MTDC grids connected to AC systems with multiple areas will face the typical challenges of stabilizing poorly-damped inter-area oscillations. The idea that VSC MTDC converters can provide damping support to the surrounding AC system by virtue of their ability for fast modulation of active power injections has been explored in recent literature [98, 99, 100, 111, 108, 93] to design supplementary controllers. In this emerging area, it is important as

---

[1]Abhishek Banerjee was the first author and responsible for writing the manuscript and applying simulation tests. Dr. Nilanjan Ray Chaudhuri and Dr. Rajesh G. Kavasseri steered the research and guided development of the manuscript.

pointed out in [99] to understand how the choice of controller structure influences improvements to dynamic system performance. Thus motivated, our goal is to design a supplementary controller, which can damp multiple modes and remain robust even after DC-side contingencies including actuator outages occur. The novelty lies in explicitly incorporating the MTDC current injection as disturbances in the control design using an $\mathcal{H}_\infty$ mixed-sensitivity formulation in the Linear Matrix Inequality (LMI) framework. This allows the control performance to be robust even when there are failures on the DC side, an aspect overlooked in recent literature. We summarize our salient contributions while drawing distinctions from prior related work as follows:

Unlike [99, 100, 111, 108, 93], we incorporate robustness against DC grid disturbances into the design formulation itself and demonstrate control performance in the wake of DC-side contingencies including converter outages. To that end, the design problem presented here includes disturbance rejection into control design by introducing a novel explicitly modeled disturbance plant as opposed to the conventional way of modeling disturbances in the LMI problem in the $\mathcal{H}_\infty$ framework, as in our prior work in [93]. This has not been reported in any prior work on MTDC systems. Moreover, we have taken into account a true MIMO design by considering two converter stations in the control design formulation to damp the targeted inter-area modes, as opposed to using only two poles of a single converter station as in [93]. This presents a tough challenge in determining the control directions in an MTDC system due to increased interactions, which has been established by RGA computations. Furthermore, robustness has been assessed on several major outages, feedback signal loss, and communication latencies. A comparison has been done with the prevailing standard $\mathcal{H}_\infty$ design for power oscillation damping to demonstrate the benefits of the proposed design over an existing technique.

Unlike [100, 111] where a single mode of interest is considered, we show that the proposed method can target multiple poorly damped modes of interest and improve their damping significantly without compromising other non-targeted modes. Unlike [108] where essentially point-to-point DC links are considered to test the control strategy, we demonstrate control performance on truly MTDC grids embedded in the AC system. We emphasize that the MTDC system or its placement is not considered solely for the purpose of damping improvement for AC systems. Neither do we consider $\mathcal{H}_\infty$-based design blindly as a "black-box" tool for robustness. Instead, our key contributions lie in modifying the design approach itself by explicitly modeling disturbances, which allows the problem

to be cast in terms of an $\mathcal{H}_\infty$ optimization. This renders our approach generic and applicable to hybrid systems regardless of the size or placement of the MTDC system within the AC system.

The chapter is organized with modeling aspects described in Sec. 5.2, control formulation and solution in Sec. 5.3, system description and signal selection in Sec. 5.4, simulation results in Sec. 5.5, and conclusions in Sec. 5.6.

5.2. Modeling and Control of MTDC Grid

We consider a bipolar VSC-MTDC grid with a metallic return network. Figure 5.1 shows the ith converter station with positive (p) and negative poles (n). Converters are represented by
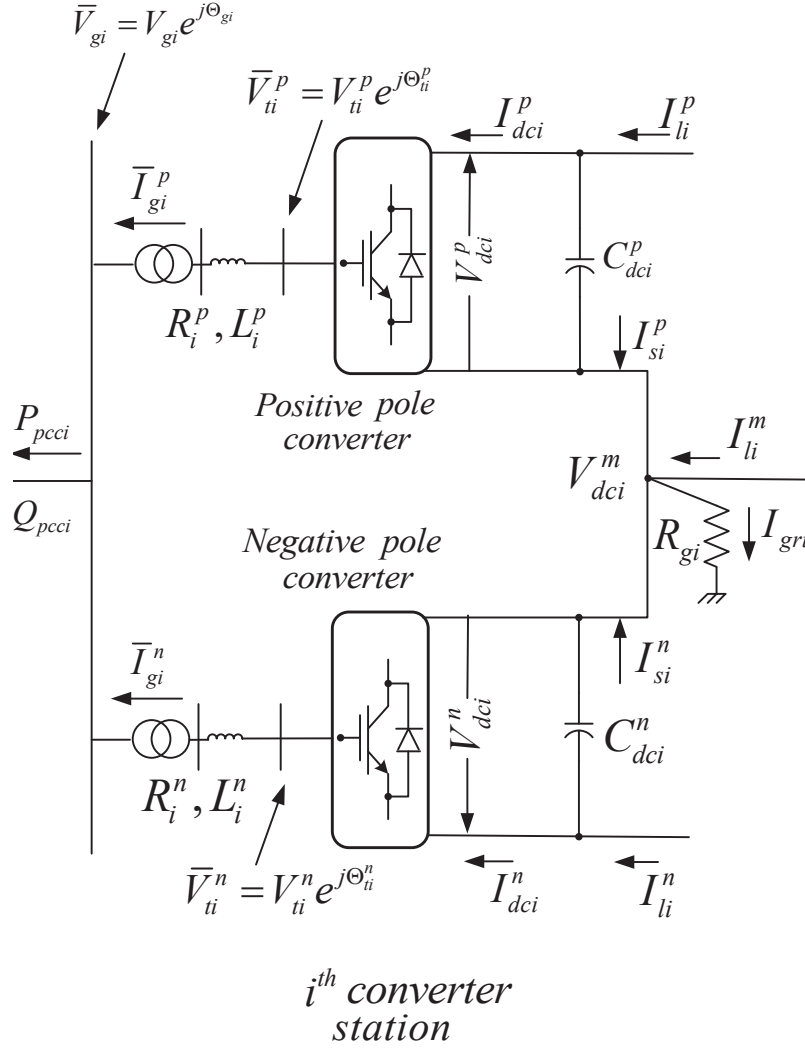
Figure 5.1. The ith converter station of the MTDC grid.

their averaged models and transmission lines between converter stations are represented by π-section models. Further details can be found in [95, 44].

5.2.1. Inner and Outer Control Loops

As shown in Fig. 5.2, the converter stations are assumed to operate under active power-common DC link voltage droop control where the error in the square of a *common* DC voltage V_{dc_comm} is drooped against the power error. Here, the DC link voltage from a common converter station is communicated to the other stations [96]. The real power reference P_{pcck}^{p*} is modulated using control input P_{mod}^{p} for power oscillation damping. As shown in Fig. 5.3 the converter stations are modeled and controlled using well-known decoupled vector control strategy in the $d - q$ frame. We denote this frame as the $X - Y$ frame to avoid conflict with the $d - q$ frame notations commonly used for individual generator models [95, 44]. The PI controller shown in Fig. 5.2 derives the X-axis current reference I_{gX}^{p*} for the inner current control loop of the positive pole converter. An identical control scheme is used for the negative pole.
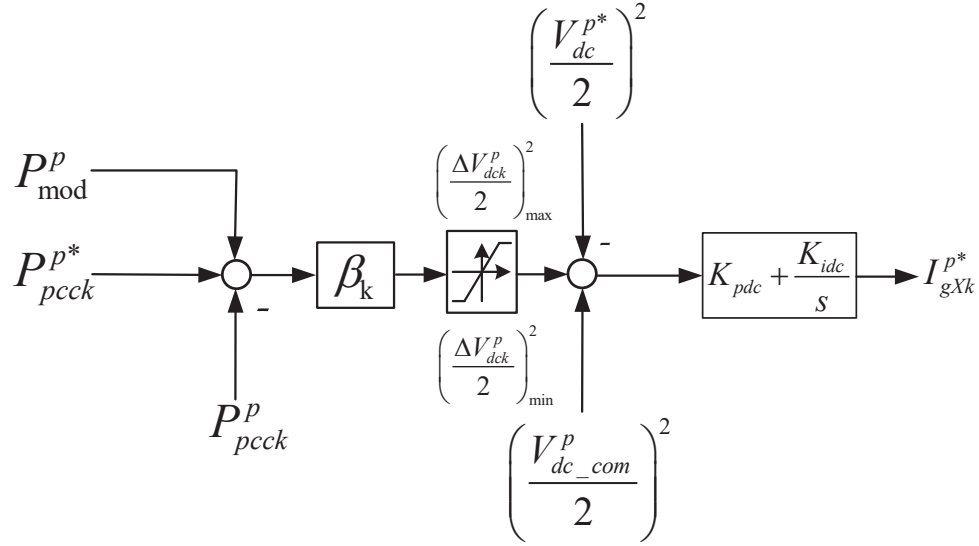
Figure 5.2. Active power-DC link voltage droop control for the positive pole of the kth converter station. The real power reference P_{pcck}^{p*} is modulated using control input P_{mod}^{p} for power oscillation damping. Identical control is used for the negative pole.

Figure 5.3. Model of the positive pole converter of the ith converter station with its inner current control loop.

5.2.2. Integration with Surrounding AC System

The differential-algebraic equation model of the multi-machine AC system is built on a current injection framework. Similarly, the MTDC portion is also modeled using this current injection framework. Interface of the converter and controller models along with the DC network model is well understood and not presented here. Interested readers are refered to [44] for details.

5.3. Control Formulation and Design

5.3.1. Explicit Modeling of Disturbance Rejection

Our key contribution is in framing a robust control problem where DC-side contingencies in the MTDC grid can be incorporated as a disturbance in a LMI formulation. Since the MTDC portion is modeled on a current injection framework, any disturbance on the DC side will induce corresponding changes in the current injections into the AC grid. In turn, this will perturb the currents I_{gX} and I_{gY} in the inner current control loop of converter station poles, which have been modeled in the $X_i - Y_i$ reference frame (see Fig. 5.3). Since our model consists of positive and negative poles in each converter station, this perturbed current can be resolved into four such current components $I_{gX}^{p/n}$, $I_{gY}^{p/n}$ for both poles of a converter station, Fig 5.4. These current components can

be further combined into the current injections at the positive and the negative poles $I_g^{p/n}$ of the converters, see Fig 5.4.
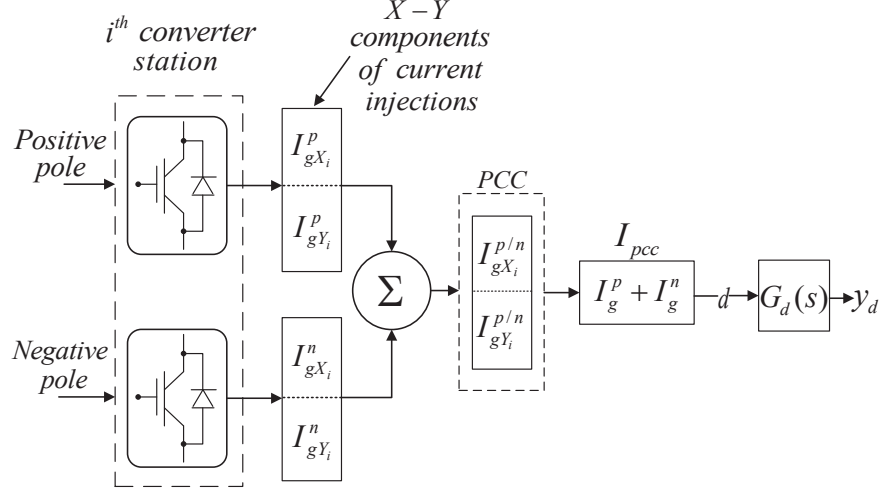
Figure 5.4. DC-side contingencies modeled as a disturbance plant $G_d(s)$ using current injections I_{pcc} as input and feedback signals y_d used for damping control as output.

Therefore, the current I_{pcc} at the point of common coupling (PCC) comprising the current injections of the positive and negative poles is modeled as the disturbance input d to the MTDC grid. Figure 5.4 represents the complete modeling of the disturbance plant $G_d(s)$ where in a nutshell, the input are the injected currents from the positive and negative poles of the ith converter station and the output are the feedback signals y_d used for damping control. Note that the synthesized disturbance plant $G_d(s)$ has the same poles as in the plant $G_u(s)$, which represents the MIMO linear model of the system between control input u denoted by P_{mod} signals shown in Fig. 5.2 and the feedback signals denoted as y_p used for damping control. The Mixed-Sensitivity formulation involving plants $G_d(s)$ and $G_u(s)$ is described next.

5.3.2. Mixed Sensitivity Formulation

With the explicitly modeled disturbances, we translate the Stacked Sensitivity problem to an $\mathcal{H}_\infty$ optimization.

The modeled disturbance plant $G_d(s)$ is incorporated into the formulation of the generalized plant P and further included in the LMI by formation of the partitioned plant. The combined output
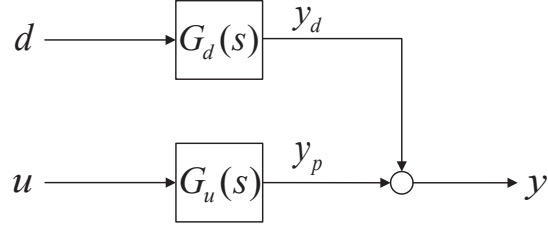
Figure 5.5. Combined output of the nominal and the disturbance plant.

as shown in Fig. 5.5 can be expressed as $y = G_d(s)d + G_u(s)u$ where,

$$G_d = C(sI - A)^{-1}B_d, \ G_u = C(sI - A)^{-1}B_u \tag{5.1}$$

The proposed control scheme is depicted in Fig. 5.6 where d, r are the exogenous input including disturbances. The regulated output are z_1 and z_2, and being a regulator problem, the reference $r = 0$.
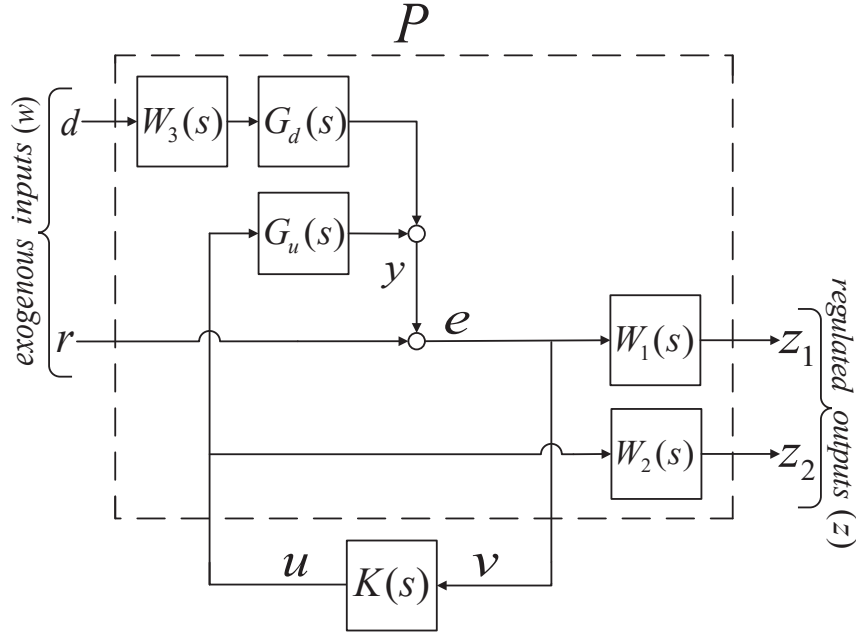
Figure 5.6. Mixed sensitivity with explicit disturbance rejection

The generalized plant P, including the weighting filters and the disturbance plant can be partitioned as,

$$P = \left[\begin{array}{c|c} P_{11} & P_{12} \\ \hline P_{21} & P_{22} \end{array} \right] \quad (5.2)$$

such that its parts resemble with z, v, w, and u and in the generalized control configuration as,

$$z = P_{11}w + P_{12}u$$
$$v = P_{21}w + P_{22}u \quad (5.3)$$

Expanding this to the proposed mixed-sensitivity scheme as shown in Fig. 5.6, the generalized plant P is obtained as,

$$P = \left[\begin{array}{cc|c} W_1 W_3 G_d & W_1 G_u \\ 0 & W_2 \\ \hline G_d & G_u \end{array} \right] \quad (5.4)$$

After the interconnecting structure has been used to determine P, the next step is to synthesize a sub-optimal controller, and combine the controller in the structure in Fig. 5.6, to obtain the closed-loop form N, which represents the closed-loop transfer function, see Fig. 5.7, from the exogenous input to the regulated output, i.e, from $[\frac{r}{d}]$ to $[\frac{z_1}{z_2}]$. N is calculated using a Lower Fractional Transformation (LFT), [49] which yields,

$$N = P_{11} + P_{12}K\left(I - P_{22}K\right)^{-1}P_{21} \cong F_l\left(P, K\right) \quad (5.5)$$
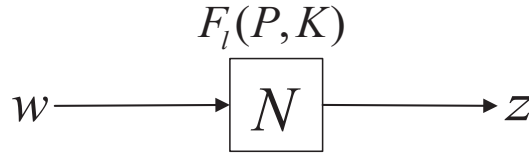
Figure 5.7. General block diagram for analysis of closed-loop performance.

The $\mathcal{H}_\infty$ optimization problem now boils down to find a stabilizing controller K to minimize the cost function,

$$\left\| \begin{bmatrix} W_1 S & W_1 S G_d W_3 \\ W_2 K S & W_2 K S G_d W_3 \end{bmatrix} \right\|_\infty \tag{5.6}$$

which is the $\mathcal{H}_\infty$ norm of the transfer function from $[\frac{r}{d}]$ to z. Since in our case $r = 0$, the cost function in (5.6) simplifies to (5.7). The goal of the $\mathcal{H}_\infty$ design is minimizing (5.7) for guaranteed robustness.

$$\left\| \begin{bmatrix} W_1 S G_d W_3 \\ W_2 K S G_d W_3 \end{bmatrix} \right\|_\infty \tag{5.7}$$

This $\mathcal{H}_\infty$ optimization problem in (5.7) involves solutions of LMI's for minimizing $\|N\|_\infty$, which guarantees asymptotic stability. This is a well studied aspect and it involves the solutions of LMI's in regard to the bounded real lemma [101], [102], using Schur's formula for the determinant of a partitioned matrix [49], and is not discussed here. This LMI problem can be solved by using the Robust Control Toolbox in Matlab [112]. An additional constraint to place all poles on the left-half of of the s-plane within a conic sector was considered to ensure the desired closed-loop damping ratio [103], [104], [105].

5.4. Test System and Damping Controller Synthesis

5.4.1. Test System

The MTDC grid consists of four converter terminals, which are interconnected to the 16-machine NETS-NYPS system [52] as shown in Fig. 5.8. The nominal real and reactive powers at the PCC of the converter stations are annotated in this figure. All generators are represented by subtransient models and eight of them ($G1 - G8$) are equipped with the IEEE DC1A excitation system. The rest of the machines are under manual excitation control, and $G9$ is equipped with a static exciter and a power system stabilizer (PSS). Constant impedance type loads are considered. The dynamic data and base case conditions are as in [52].

5.4.2. Signal Selection Criterion

Eigenvalue analysis reveals that the system has two poorly damped inter-area modes of interest: (0.2 Hz at 1.5 %) and (0.47 Hz at 3.3 %), which are shown in Table 5.1. Since the specific objective of the damping controller is to improve the damping of these two modes without negatively
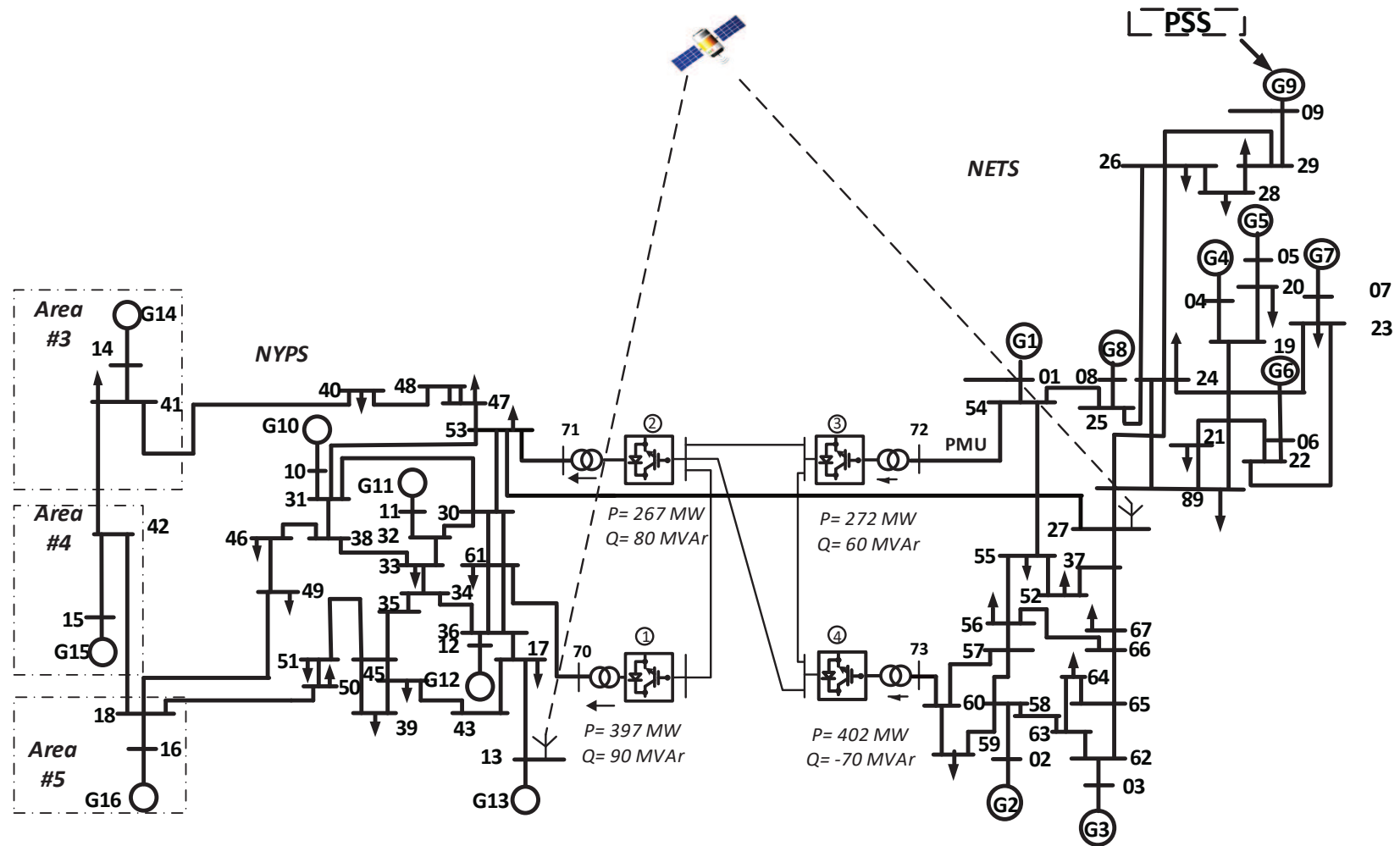
Figure 5.8. Bipolar MTDC grid with metallic return (single line diagram) connected to 16-machine AC system.

impacting the others, it is necessary to learn the interaction among input and output, and identify the most appropriate control directions.

Table 5.1. Damping Ratios, Frequencies and Settling Times of the Inter-Area Modes in Test System with Proposed Control

Design Criterion, $\zeta_{min} = 6.5\%$						
Mode no.	OPEN-LOOP			CLOSED-LOOP		
	ζ	f, Hz	T, s	ζ	f, Hz	T, s
1.	**0.015**	0.201	204.20	**0.285**	0.238	8.99
2.	**0.033**	0.475	40.25	**0.091**	0.473	14.68
3.	0.081	0.537	14.64	0.085	0.528	14.12
4.	0.053	0.792	15.25	0.054	0.792	14.89

To that end, residue analysis was performed for appropriate selection of feedback signals and control input. In MIMO systems, the angle of the residue is important as well. The phase compensation required at each modal frequency is closely related to the phase angles of the residue [106]. The residue analysis of the linear model shown in Table 5.2 reveals that the best selection of feedback signals are P_{27-53} across mode 1 and P_{13-17} across mode 2 whereas converter stations #1 and #3 are the best choice for the control input.

Relative Gain Array (RGA): In a true MIMO sense, RGA is used to corroborate the input/output pairing choices obtained from the signal selection. The RGA of a non-singular square matrix G is a square matrix defined as

$$RGA\left(G\right) = \Lambda\left(G\right) \cong G \times \left(G^{-1}\right)^{T} \tag{5.8}$$

Table 5.2. Residues Showing Normalized Magnitude and Angle

	Input Signals				
Feedback	Converter #1		Converter #3		
	mag	ang (degree)	mag	ang (degree)	Mode 1
$P_{(27-53)}$	1	-158.88	1	33.02	
$P_{(13-17)}$	0.1325	39.71	0.1325	-128.37	
	Input Signals				
Feedback	Converter #1		Converter #3		
	mag	ang (degree)	mag	ang (degree)	Mode 2
$P_{(27-53)}$	0.0632	-57.97	0.0632	-11.04	
$P_{(13-17)}$	1	125.03	1	171.96	

where $\times$ denotes element-by-element multiplication (the Schur or Hadamard product). RGA can also be computed for non-square matrices by the method of pseudoinverse [49].

RGA values are useful to guide the selections because: (a) values close to 1 show favourable pairing [113] for centralized control scheme and (b) negative entries indicate too much interaction and not suitable for pairing. In our design, RGA was calculated for the nominal plant $G_u(s)$ with results shown in Table 5.3, where the input are the columns and the feedback signals are the rows. The analysis clearly affirms with the input/output pairing choices made earlier by residue calculations.

Table 5.3. Relative Gain Array

Output	Input			
	Converter #**1**	Converter #**2**	Converter #**3**	Converter #**4**
$P_{(13-17)}$	-0.311	-0.121	**0.655**	0.533
$P_{(27-53)}$	**0.793**	0.311	-0.249	-0.172

As seen in Table 5.3, for the feedback signal P_{13-17}, converter station #3 shows the best possibility of pairing with RGA value being closest to unity. Although converter station #4 negative pole has a closer value than #3 negative pole, we choose #3 as the best possible case because it has a higher modal controllability index for mode 2. For feedback signal P_{27-53}, converter #1 stands closest to unity which validates our signal selection.

5.4.3. Process for Damping Controller Synthesis

5.4.3.1. Damping Criterion

The closed loop poles of the critical modes are placed within a conic sector with inner angle θ and the apex at the origin [104], [105] to ensure a minimum damping ratio $\zeta_{min} = cos(\theta/2)$. A minimum damping ratio of 6.5% was chosen for both modes which corresponds to an inner angle of 3.0115 radians. The design achieves this specification for both the inter-area modes.

5.4.3.2. Weighting Filter Selection

The weighting filters W_1, W_2, and W_3 in Fig 5.6 are selected in light of the following requirements:

• **Selection of W_1**: The disturbance d as in Fig 5.5 is a low frequency signal and is hence penalized with a low-pass filter with the bandwidth equal to the disturbance signal d. Iteratively,

W_{1_init} was best found as (5.9), where $K_1 = 0.05$. In order to scale it to the plant gain, a 3-stage cascade is used to obtain W_1, resulting in a 6th order filter.

$$W_{1\_init}(s) = K_1 \frac{0.25}{s^2 + s + 0.25} \tag{5.9}$$

The added advantage of the cascade was the steepness of the low pass filter, which proved to be very effective for the disturbance attenuation at the low frequencies, and to achieve improvement in damping for the required modes. W_1 dominates in the frequency range of $(0 - 8.5 \text{ rad/s})$. It should be noted that all the modes of interest are within this frequency range.

• **Selection of W_2**: The filter W_2 is selected to be a highpass filter with crossover frequency approximately equal to the closed loop bandwidth of the system. This improves control effort minimization at higher frequencies. The cut-off frequency for the high-pass filter was set to 150 rad/s to limit the magnitude of the closed loop poles of the controller. W_2 was also obtained after cascading the high-pass filter $W_{2_{init}}$ (5.10) in series resulting in a 6th order high-pass filter, where $K_2 = 0.01$. In order to ensure that the weight W_1 dominated at the low frequencies for successful disturbance attenuation, W_2 was designed to attain a low frequency gain of -572 dB.

$$W_{2\_init}(s) = K_2 \frac{s^2}{s^2 + 120s + 3600} \tag{5.10}$$

• **Selection of W_3**: W_3 is weighted for the disturbance plant input matrix. It is selected as $W_3 = \alpha I$, with α designed for disturbance rejection by scaling the input of the disturbance plant as close as possible to the nominal plant. After an iterative process, $\alpha = (50 \times 10^{-6})$ is obtained to satisfy these criteria.

5.4.3.3. Damping Controller Design

A self-explanatory flowchart is shown in Fig. 5.10, which summarizes the damping controller design methodology. The original plant and the disturbance plant are reduced to a 20th order equivalent by Schur Balanced Truncation [49], see Fig. 5.9. The reduced plants capture the targeted inter-area modes of 0.201 Hz and 0.475 Hz. As shown in Fig. 5.10, the objectives of the control design is simultaneous disturbance attenuation, explicitly modeled disturbance rejection, and control effort minimization. This resulted in a 56th order controller, which was reduced to 28th order - the singular
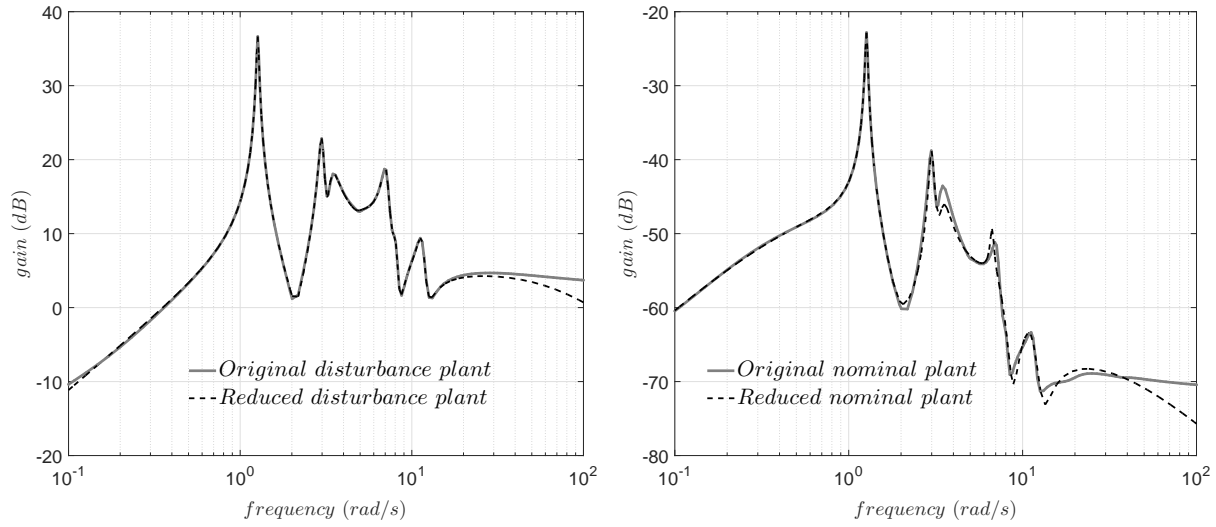
Figure 5.9. Maximum singular value plot of the disturbance plant $G_d(s)$ and nominal plant $G_u(s)$.

value plots are shown in Fig.5.11(a). The designed controller modulates the real power reference of the positive and negative poles of converter stations #1 and #3. The control design was performed using the Robust Control Toolbox in Matlab [112]. Table 5.1 highlights the closed-loop poles of the system with the reduced controller, which shows that a settling time of less than $15.0s$ is achieved for the targeted modes without compromising the well-damped modes.

5.4.4. Comparison of Performance with Standard $\mathcal{H}_\infty$ Design

A comparison study with the standard $\mathcal{H}_\infty$ design was performed to present the effectiveness of the proposed control scheme. The standard $\mathcal{H}_\infty$ design philosophy is kept the same as in [93]. The same reduced-order nominal plant was used for the control design. In order to maintain uniformity in design, the same weights (5.9), (5.10) were chosen, and cascading was performed in a similar fashion as in case of the explicit disturbance rejection design. This resulted in a 56th order controller, which was reduced to 28th order - the singular value plots are shown in Fig.5.11(b).

Table 5.4 shows the closed loop poles with the standard $\mathcal{H}_\infty$ design. This is the best possible closed-loop damping performance we could achieve, albeit with $\zeta_{min} = 15\%$ as design criterion, as opposed to $\zeta_{min} = 6.5\%$ used for the proposed method. Attempt to increase closed-loop damping by further increasing ζ_{min} lead to non-convergence. It can be seen in Table 5.4 that the closed-loop damping is slightly inferior compared to the explicit disturbance rejection design, in Table 5.1.
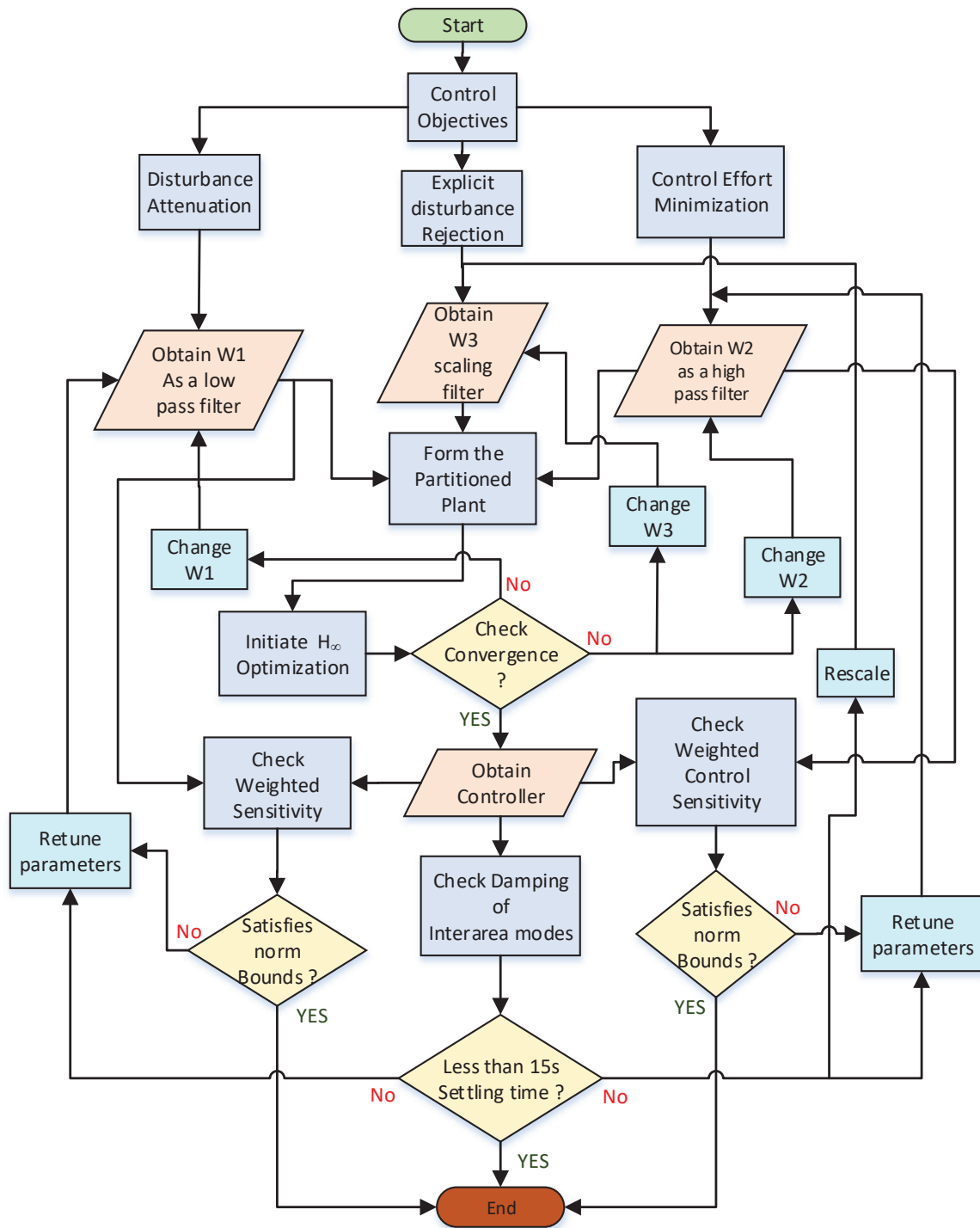
Figure 5.10. Flowchart describing damping controller synthesis.
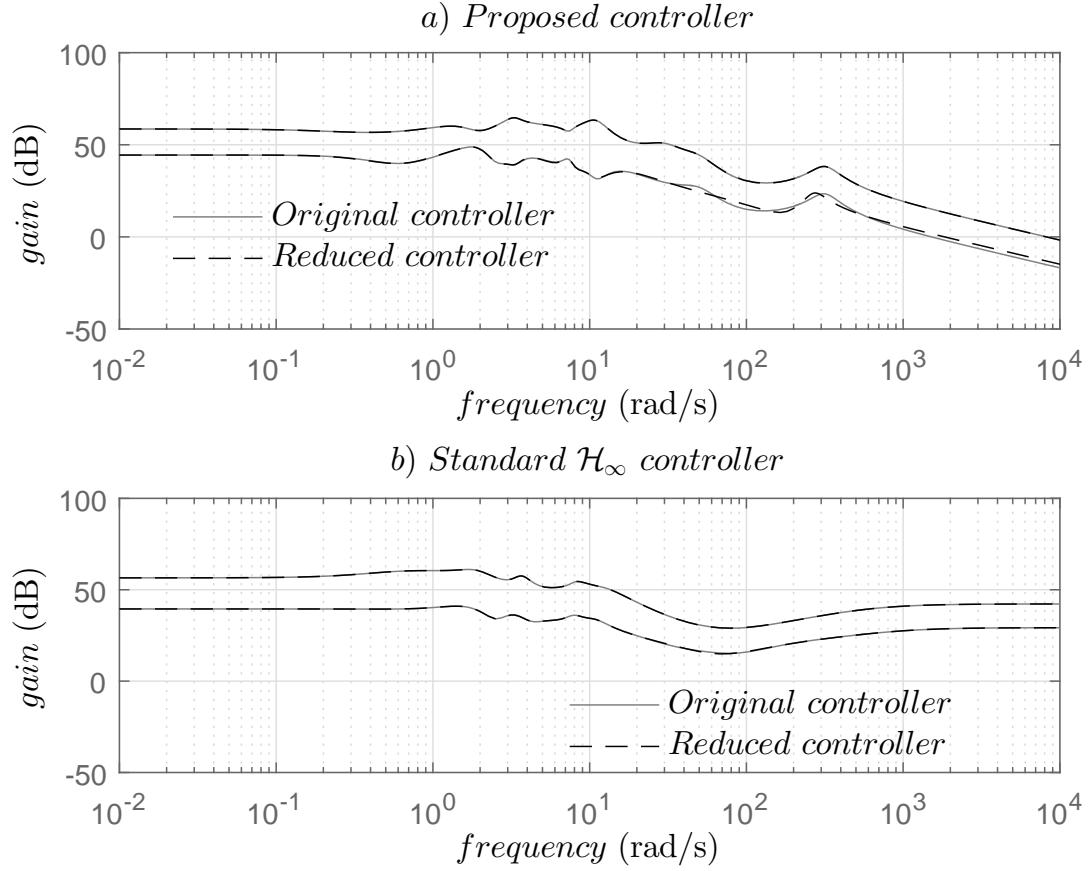
Figure 5.11. Frequency response of the synthesized damping controllers: a) proposed controller, b) standard $\mathcal{H}_\infty$ controller.

Figure 5.12 shows the comparison of control effort between the standard $\mathcal{H}_\infty$ design and the proposed design when a pulse disturbance is applied at the input of the closed-loop full-order linearized plant. The proposed controller produces slightly better damping performance at significantly lesser control effort.

Table 5.4. Damping Ratios, Frequencies and Settling Times of the Inter-Area Modes in Test System with Standard $\mathcal{H}_\infty$ Control

Design Criterion, $\zeta_{min} = 15\%$						
Mode no.	OPEN-LOOP			CLOSED-LOOP		
	ζ	f, Hz	T, s	ζ	f, Hz	T, s
1.	**0.015**	0.201	204.20	**0.214**	0.192	15.17
2.	**0.033**	0.475	40.25	**0.070**	0.501	18.09
3.	0.053	0.792	15.25	0.061	0.795	13.09
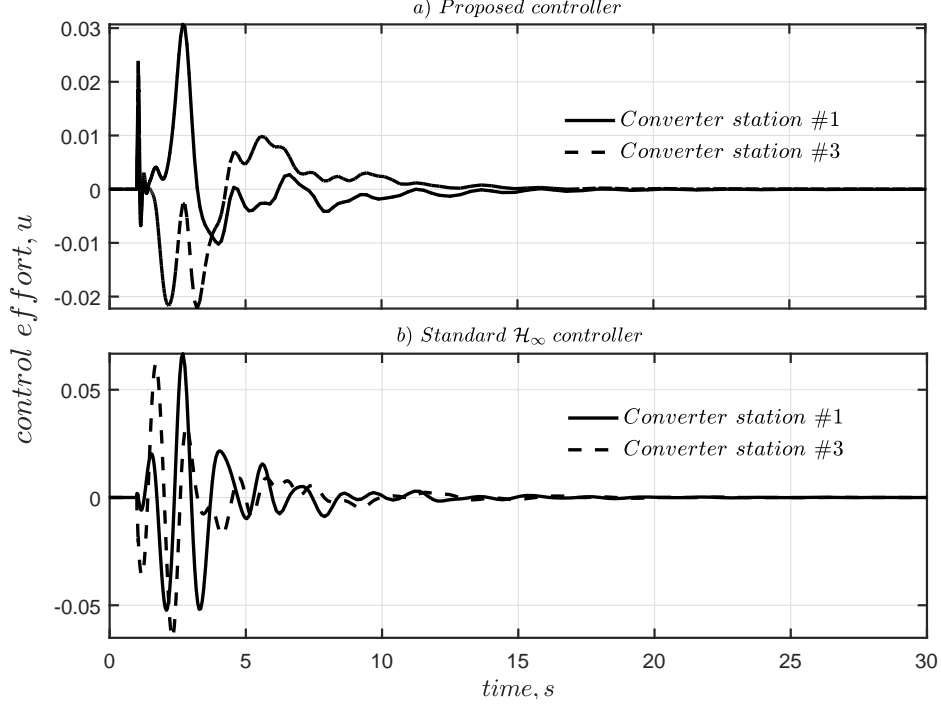
Figure 5.12. Comparison of control effort between a) proposed controller and b) standard $\mathcal{H}_\infty$ controller when a pulse disturbance is applied at the input of the closed-loop full-order linearized plant.

5.4.5. Measures of Robustness

Robustness in the design can be observed from the infinity norm of the weighted sensitivity and the control times sensitivity, according to the Small Gain Theorem and the Bounded Real Lemma [101, 49]. Both the weighted functions in our proposed design satisfy the robustness criteria:

$$\|W_1 S\|_\infty = 1.2523 \times 10^{-4}, \ \|W_2 K S\|_\infty = 7.3755 \times 10^{-5}.$$

They also satisfy the robustness criterion with the standard $\mathcal{H}_\infty$ design:

$$\|W_1 S\|_\infty = 1.2518 \times 10^{-4}, \ \|W_2 K S\|_\infty = 1.2889 \times 10^{-4}.$$

Another measure of robustness is the smallest unstructured inverse input multiplicative perturbation at the sensitivity function that can destabilize the system. This parameter can be evaluated by placing a bound on the largest singular value of the sensitivity [114]. If we assume the perturbation as δ_0, then robust stability requires $\bar{\sigma}\left[(I - L)^{-1}\right] < \frac{1}{\delta_0}$, where $L = KG$ is the open loop gain at the plant input channels. The singular values of the input plant sensitivity are plotted in Fig. 5.13, which correspond to the smallest unstructured inverse input multiplicative perturbation.

76
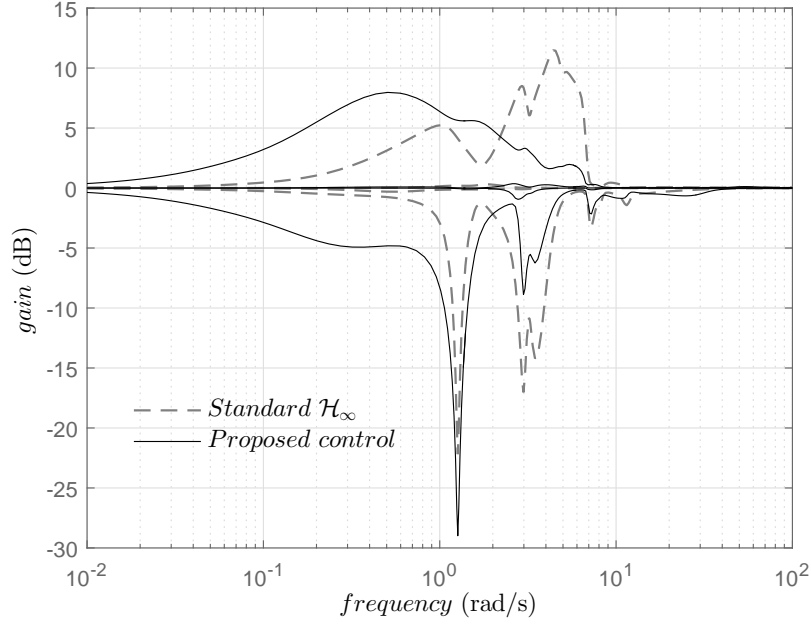
Figure 5.13. Input plant sensitivity subject to the designed controllers

From Table 5.5, it can be seen that δ_0 for the proposed controller is almost twice of that of the standard $\mathcal{H}_\infty$ controller. This indicates that the proposed control has a greater bound for the disturbance input, i.e, any perturbation in the input channels of the plant will have to be almost double the amount as compared to the standard $\mathcal{H}_\infty$ design to destabilize the system. This ensures that the disturbance attenuation property of the proposed control design is superior, which makes it more robust to disturbance input than that of the existing method.

The phase and gain margins at the input channels [114] are calculated using (5.11) and shown in Table 5.5. The gain and phase margins at the input channels are comparitively better for the proposed control.

$$GM = \left[\frac{1}{1+\delta_0}, \frac{1}{1-\delta_0}\right], \quad PM = \pm\cos^{-1}[1 - \frac{\delta_0^2}{2}]$$

(5.11)

Table 5.5. Input Plant Sensitivity

Control used	$\bar{\sigma}\left(I - L\right)^{-1}$	δ_0	GM	PM
Proposed	7.96dB	0.4	[1.67,0.714]	±23.04°
Standard $\mathcal{H}_\infty$	11.5dB	0.26	[1.32,0.79]	±15.27°

77

Remark: For an MTDC grid connecting offshore wind farms to onshore AC system, a combination of onshore converter stations and offshore wind farms can be used as actuators. The real power reference of the offshore wind farms can be modulated using remote PMU signals from the onshore AC grid.

5.5. Simulation Results

To demonstrate robustness of the proposed control scheme, simulations were carried out for multiple contingencies, which trigger the inter-area modes. Unlike earlier works, which considered only AC-side faults, we illustrate performance following major AC as well as DC-side disturbances. From now on, we will use the legend "Explicitly modelled DR" to represent the proposed explicitly modeled disturbance rejection controller response in the plots.

5.5.1. Major Tie-Line Outages

We have considered outages of one of the tie-lines in each of the double-circuit lines connecting buses $(18-42)$, $(18-49)$, $(27-53)$ and $(40-41)$, see Fig. 5.8, following a 3-phase, 5-cycle fault. The faults were simulated near bus 18, 49, 27, and 40, respectively. Notably, these tie-lines interconnect the five areas in the meshed AC-MTDC system.

Figure 5.14. Dynamic performance of the system following a 3-phase fault near bus 18 cleared after 5-cycles by the outage of one of the double-circuit lines connecting buses 18 and 42, Fig. 5.8, at $t = 1.0s$.

78

Figure 5.15. DC voltage of the converter poles following a 3-phase fault near bus 18 cleared after 5-cycles by the outage of one of the double-circuit lines connecting buses 18 and 42, Fig. 5.8, at $t = 1.0s$.

Figure 5.16. Dynamic performance of the system following a 3-phase fault near bus 49 cleared after 5-cycles by the outage of one of the double-circuit lines connecting buses 18 and 49, Fig. 5.8, at $t = 1.0s$.

Figures 5.14, 5.16, 5.18, and 5.19 show effective damping for outage of lines $(18-42)$,$(18-49)$, $(27 - 53)$ and $(40 - 41)$, respectively. It can be seen from Figs 5.14, 5.16, 5.18, and 5.19 that the proposed method produces similar damping performance compared to the standard $\mathcal{H}_\infty$ control, in

case of major tie-line outages in the grid. This is expected since both approaches are robust control design methods. The DC voltages of the converter stations' negative and positive poles are plotted in Figs 5.15, 5.17, and 5.20 in the event of outage of the lines $(18 - 42)$, $(18 - 49)$ and $(40 - 41)$, respectively. It can be observed that the DC voltage excursions in the converter station poles during these events are lower for the proposed control design. This is a consequence of a significantly less control effort required to damp the oscillatory modes in case of the proposed approach.

5.5.2. Converter Station Outage

1) Negative pole outage at converter station #2

Figures 5.21 and 5.22 show the dynamic performance of the system following the outage of the negative pole of converter station #2. It can be seen that – (a) At $t = 1.0s$ the real power output of converter #2 negative pole becomes zero; (b) The explicitly modelled disturbance rejection $\mathcal{H}_\infty$ damping controller is able to damp the oscillatory modes better than the standard $\mathcal{H}_\infty$ controller; (c) Major line power flows have been shown in Fig. 5.21 whereas Fig. 5.22 shows DC voltages of the negative and positive poles of the converter stations.

2) Actuator outage: Negative pole outage at converter station #3

Converter station #3 was used as an actuator in the control design. The outage of one pole of
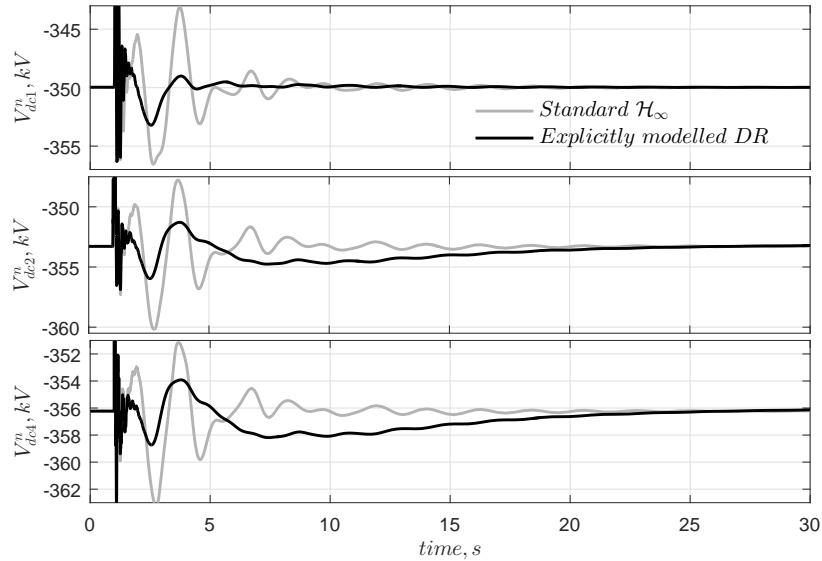
Figure 5.17. DC voltage of the converter poles following a 3-phase fault near bus 49 cleared after 5-cycles by the outage of one of the double-circuit lines connecting buses 18 and 49, Fig. 5.8, at $t = 1.0s$.

80
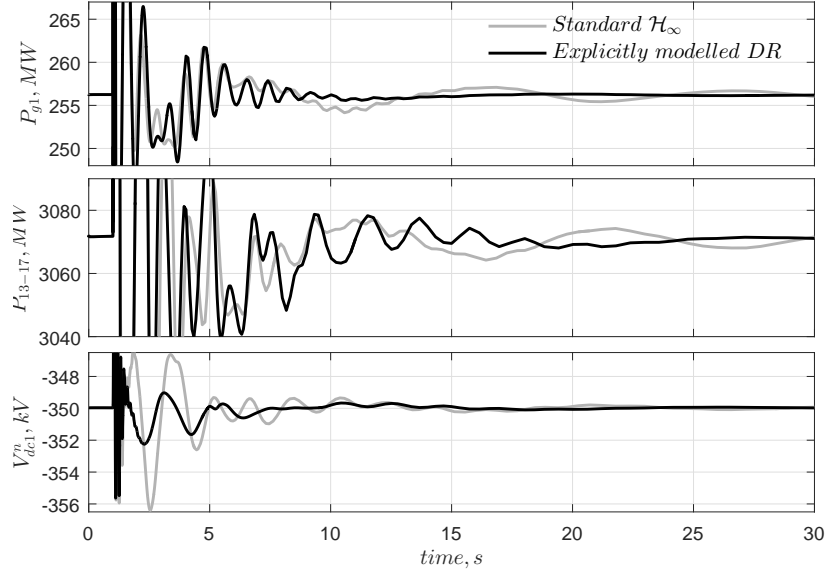
Figure 5.18. Dynamic performance of the system following a 3-phase fault near bus 27 cleared after 5-cycles by the outage of one of the double-circuit lines connecting buses 27 and 53, Fig. 5.8, at $t = 1.0s$.

converter #3 may have serious consequences, if it is not considered in the design phase of the controller. Figure 5.23 shows that despite the outage of the actuator, the proposed damping controller
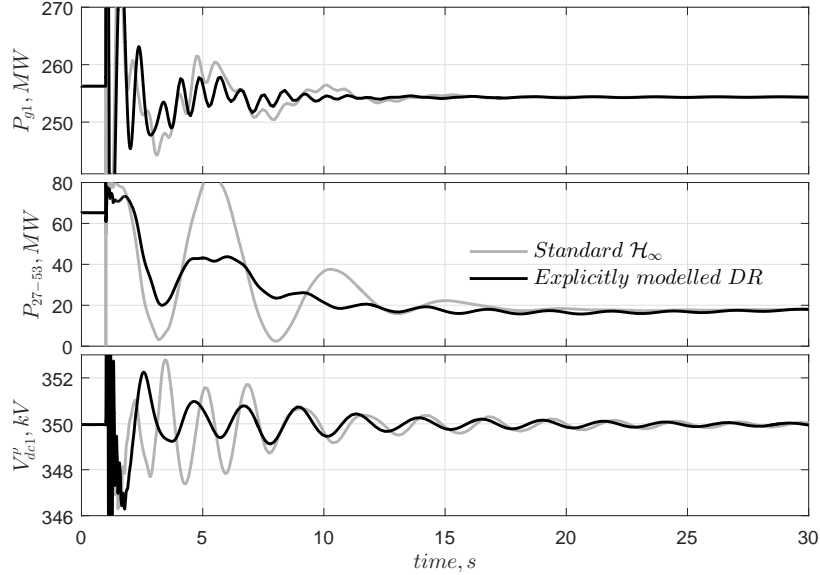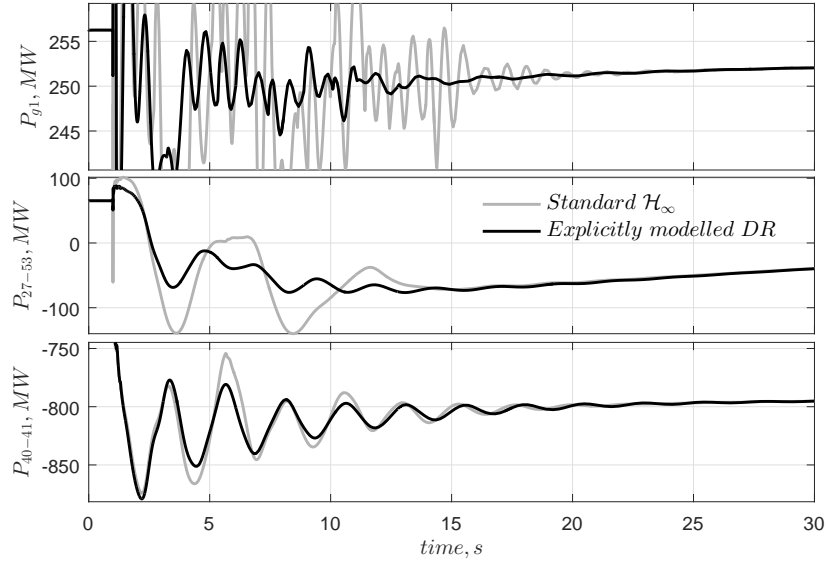

Figure 5.19. Dynamic performance of the system following a 3-phase fault near bus 40 cleared after 5-cycles by the outage of one of the double-circuit lines connecting buses 40 and 41, Fig. 5.8, at $t = 1.0s$.
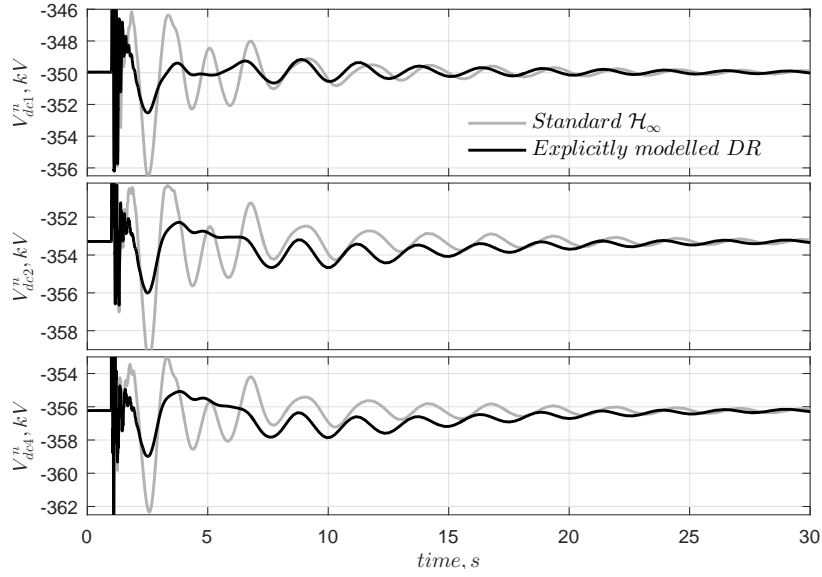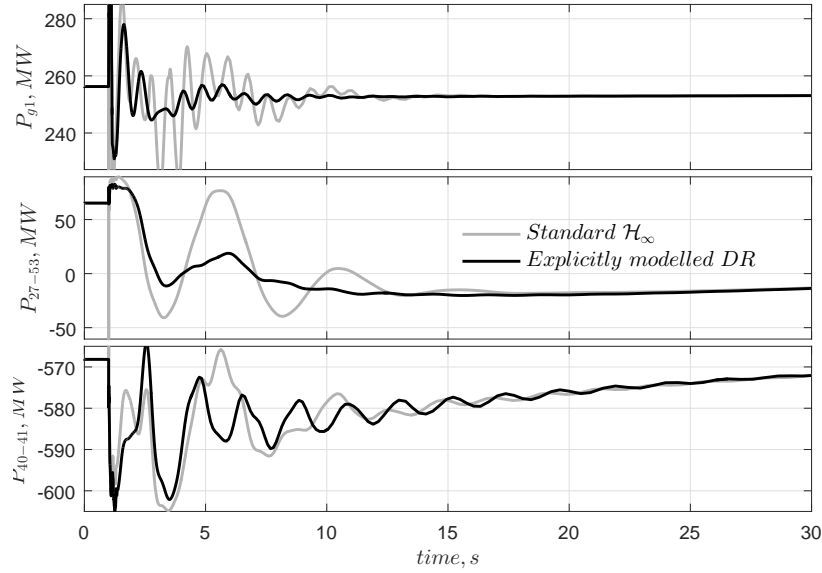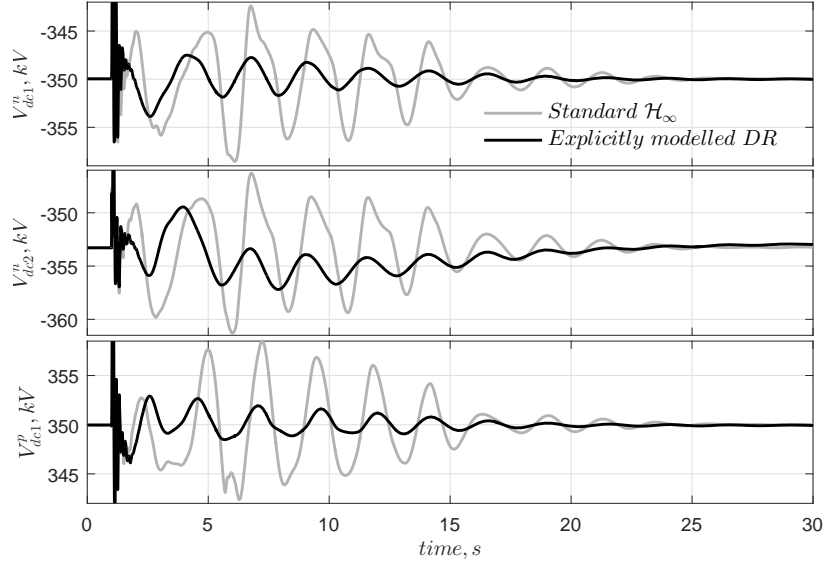
Figure 5.20. DC voltage of the converter poles following a 3-phase fault near bus 40 cleared after 5-cycles by the outage of one of the double-circuit lines connecting buses 40 and 41, Fig. 5.8, at $t = 1.0s$.
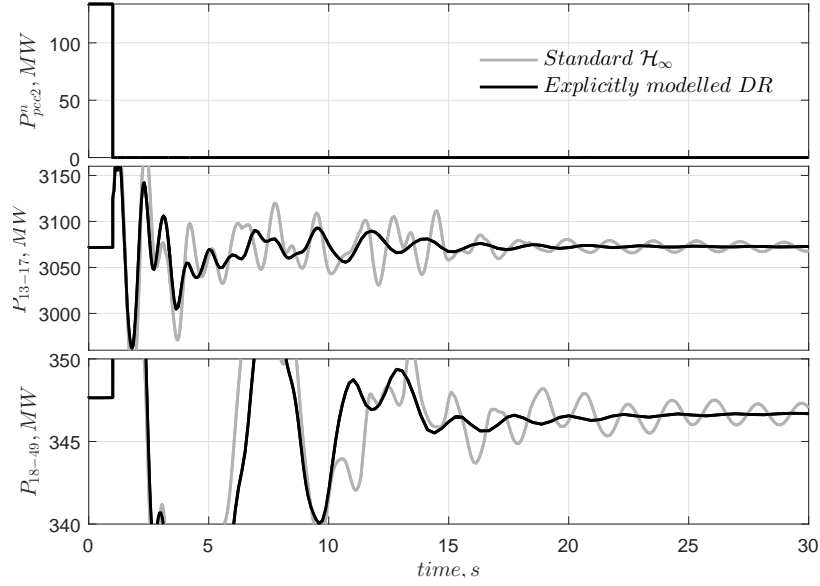
Figure 5.21. Dynamic performance of the system following the outage of the negative pole of converter station #2 at $t = 1.0s$.

demonstrates strong disturbance rejection properties. The actuator #3 outage can been seen from the first subplot in Fig. 5.23. It can be observed that the proposed controller produces better damping performance in the event of actuator outage-a major DC-side contingency scenario. Figure 5.24
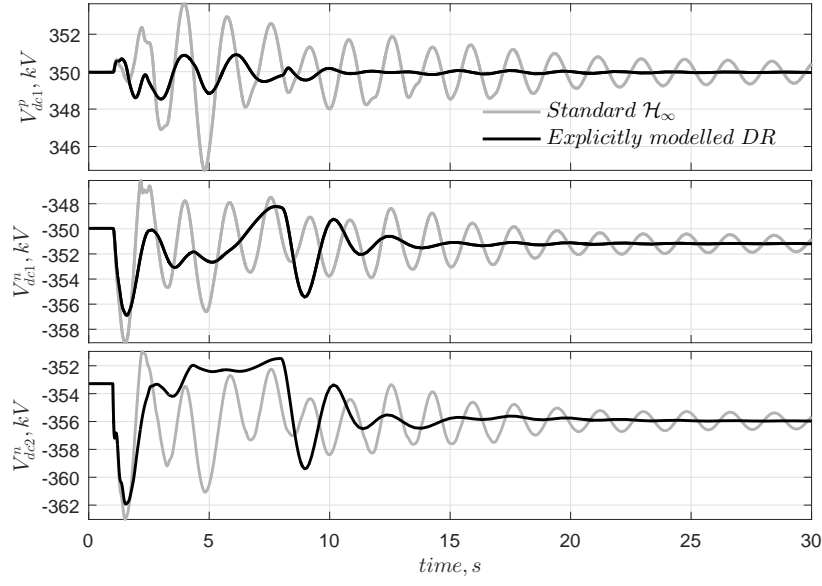
Figure 5.22. DC voltage of the converter poles following the outage of the negative pole of converter station #2 at $t = 1.0s$.

shows the DC voltage of converter station #1's positive and negative pole in the first two subplots, and the power modulation in the positive pole of converter #4 in the last subplot.
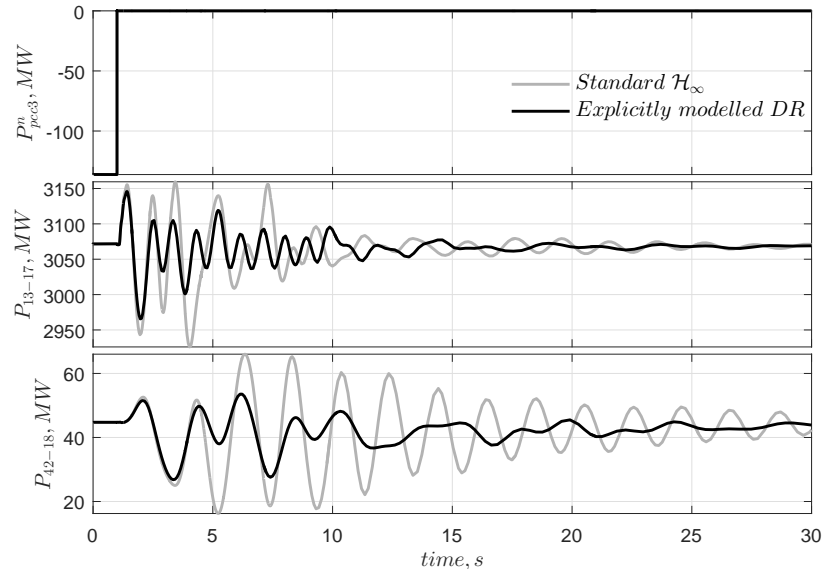
Figure 5.23. Dynamic performance of the system following the outage of the negative pole of converter station #3 at $t = 1.0s$.
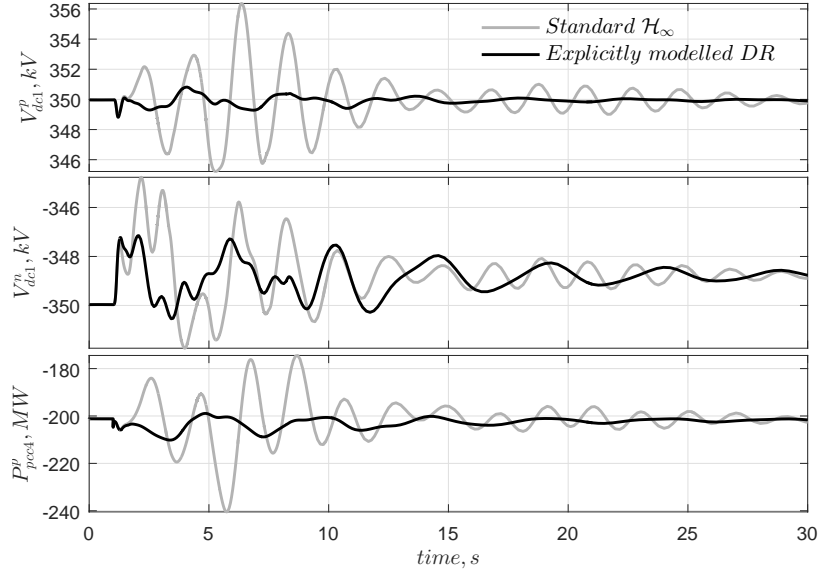
Figure 5.24. Dynamic performance of the system following the outage of the negative pole of converter station #3 at $t = 1.0s$.

The damping performance of the standard $\mathcal{H}_\infty$ controller is comparatively inferior to the proposed controller in case of major DC-side outages, see Figs 5.21, 5.23. Moreover, the DC voltage profiles in the converter station poles in Figs 5.22 and 5.24 show huge excursions with the standard $\mathcal{H}_\infty$ control due to higher control effort requirement. On the contrary, the proposed controller produces lesser fluctuations in the DC voltages. These results confirm the benefits of the novel concept of explicitly modeling the disturbances for controller design, as this approach produces better damping performance with lesser control effort for AC as well as DC-side outages.

5.5.3. Feedback Signal Loss

Figure 5.25 shows the dynamic performance of the damping controller with the loss of the feedback signal P_{13-17}, following the outage of one of the double-circuit lines connecting buses 18 and 49 at $t = 1.0s$. A similar damping performance can be observed for both the design approaches.

5.5.4. Communication Latency

To demonstrate the robustness of the controller performance following (a) converter #2 negative pole outage and (b) outage of one of the double circuit lines connecting buses 18 and 42 are studied in presence of a 100 ms latency in the feedback signals. The effectiveness of the controller in presence of latency can be seen in Fig. 5.26 following the converter and the line outage scenarios. It is interesting to note that for the AC line outage, see the last subplot in Fig. 5.26, the standard $\mathcal{H}_\infty$
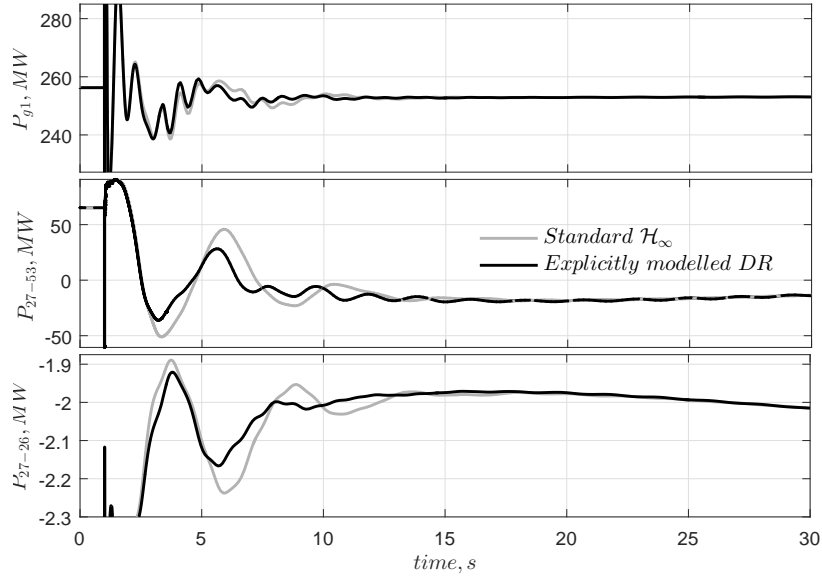
Figure 5.25. Dynamic performance of the system with the loss of feedback signal P_{13-17}, following the outage of one of the double-circuit lines connecting buses 18 and 49 at $t = 1.0s$.
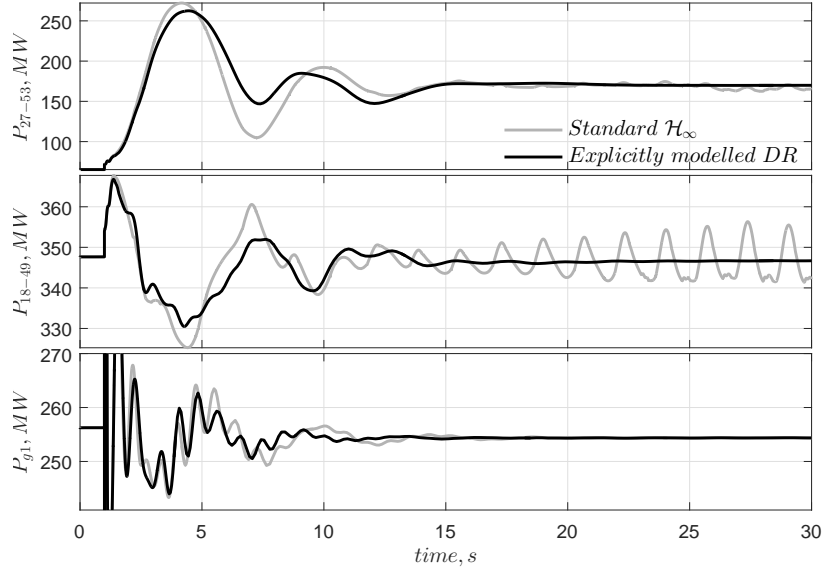
Figure 5.26. Dynamic performance of the system with 100 ms latency following the outage of a) first two subplots - the negative pole of converter station #2 at $t = 1.0s$. b) last subplot - one of the double-circuit lines connecting buses 18 and 42 at $t = 1.0s$.

controller produces a similar performance as the proposed controller. However, in case of the DC outage, shown in the first two subplots in Fig. 5.26, the standard $\mathcal{H}_\infty$ controller fails to maintain stability. This further substantiates the need for explicitly modeling disturbances in the control

formulation to take into account such events that can cause the standard $\mathcal{H}_\infty$ control technique to fail.

5.6. Summary

This chapter presents a new approach for robust power oscillation damping in MTDC grids connected to AC systems. The novelty consists in modifying the $\mathcal{H}_\infty$ control design approach where disturbances can be viewed and accounted explicitly in terms of MTDC current injections. This problem is solved by an updated mixed sensitivity formulation in the Linear Matrix Inequality (LMI) framework. The resulting MIMO controller uses wide-area signals to stabilize poorly-damped inter-area modes without compromising well-damped modes. Control performance and robustness are assessed with dynamic simulations on a 16-machine 5-area system connected to a 4-terminal asymmetric bipolar MTDC grid. The unique aspect of the proposed controller is its robustness to severe disturbances on the AC as well as DC side - including loss of actuators. In addition, the proposed controller is able to maintain acceptable performance in the wake of communication latencies and partial signal loss. The proposed design approach shows superior performance compared to a standard $\mathcal{H}_\infty$ design.

6. CONCLUSION AND FUTURE RESEARCH DIRECTIONS

6.1. Conclusion

This thesis provides a new approach for resilient monitoring of the power grid by using energy function sensitivity and a novel control architecture for robust damping controller design for inter-area oscillations damping in a hybrid AC-MTDC grid. The research work here is presented in chapters above based on previously published papers and the essential conclusions are drawn as follows:

- Chapter 2 presents a resilient monitoring scheme for fault detection in a multi-machine setting by exploring the wide area and system component information-rich SPEFs sub-spaces. A sliding window based principal component sensitivity algorithm derived from singular value decomposition technique is introduced. This energy function approach to wide area monitoring, delves further into the post-fault dynamics of the system and their effects on the interconnected system components. The effectiveness of the approach can be witnessed in certain PCs of individual energy functions which are highly affected by different categorical events. The variability of certain SPEFs also are indicative of the severity of the fault by conveying the information in their respective principal components. Finally, this approach is able to depict the changes in energies of the system-wide components and paves the way for using this information in more complex test systems where increased interactions can be expected.

- In chapter 3, we extend the concept of energy functions based monitoring to identify a metric and explore its potential in averting zone 3 failures in distance relays using two separate test cases; a) IEEE 39 bus New England test system (NETS) for offline simulations and b) a part of the Western Electricity Coordinating Council (WECC) system as an actual blackout simulation model. The offline model is used to ascertain the most sensitive energy function in the event of relay misoperations, which is later constructed and monitored online during an actual blackout progression. Our key contribution lies in the observation that the energy function sub-component (W_{25}) is a sensitive metric to discriminate between faults and load

encroachment during stressed conditions. We track and study the sensitivity of this metric to different system conditions including generator faults, line faults, and loading conditions in both test systems. Results indicate that since this metric is independent of relay settings, it can be potentially be used as an alternative index to monitor and supervise the actions of distance relays in response to critical system events.

- Chapter 4 demonstrates the control design and implementation a MIMO robust supplementary power oscillation damping controller using MTDC converter terminal poles as actuators in an AC-MTDC grid setting. The control formulation is based on H_∞ mixed-sensitivity in the Linear Matrix Inequality (LMI) framework, aided by appropriate selection of weight filters based on the upper bound of the maximum singular values in various sensitivity functions. The effectiveness of the robust design is validated through simulation results in two test systems: a) 6-machine 3-area system with one inter-area mode of interest and b) a 16-machine 5-area system connected to a 4-terminal asymmetric bipolar MTDC grid with three inter-area modes. Significant improvement in multi-modal damping can be observed in addition to better robustness during (n-1) contingency scenarios in the AC-MTDC grid.

- Chapter 5 proposes a novel approach for robust power oscillation damping in MTDC grids connected to AC systems. The novelty lies in modifying the $\mathcal{H}_\infty$ control design approach where disturbances can be viewed and accounted explicitly in terms of MTDC current injections. This problem is solved by an updated mixed sensitivity formulation in the Linear Matrix Inequality (LMI) framework. The resulting MIMO controller uses wide-area signals to stabilize poorly-damped inter-area modes without compromising well-damped modes. Control performance and robustness are assessed with dynamic simulations on a 16-machine 5-area system connected to a 4-terminal asymmetric bipolar MTDC grid. The unique aspect of the proposed controller is its robustness to severe disturbances on the AC as well as DC side - including loss of actuators. In addition, the proposed controller is able to maintain acceptable performance in the wake of communication latencies and partial signal loss. Furthermore, the proposed design approach shows superior performance compared to a standard $\mathcal{H}_\infty$ design by significantly improving damping of the inter-area modes with only half the amount of control effort than the standard $\mathcal{H}_\infty$ control. This is a very important result which aides in obtaining

lesser voltage deviations during the event of converter station outages in the MTDC grid. Additionally, a frequency domain based measure of robustness is presented, which depicts the novel controller to be two times more robust to input channel uncertainties in the plant.

6.2. Future Research Directions

- **Energy functions-based monitoring in Variable Renewable Energy (VRE) interfaced modern power grids**: The test systems in chapters 2 and 3 are based on conventional synchronous machine based grids. The energy functions are calculated based on estimated internal states of synchronous machines and wide-area measurements available via the Phasor Measurement Units (PMUs), located at specific buses in the power system models. However, not much attention has been paid towards how to account for inverter based modern power grids that would include higher penetration levels of variable renewable energy. It would be meaningful to derive the Structure Preserving Energy Functions (SPEFs) in a VRE dominated setting and observe its effects on the approach that has been proposed in this dissertation for resilient monitoring in cascading failures. This would also call for deriving additional energy function components arising due to the contributions from the power electronic interfaces that might contribute significantly to increased sensitivity towards system faults and failures.

- W_{25} **as a new relaying metric in inverter dominated grids** The near future of power grids will be a combination of synchronous generators (SGs) and Variable Renewable Energy (VRE). In a conventional SG, faults current magnitudes are very high which provide specific signatures for over-current and distance relays to trip during faults. However, in an inverter dominated grid, the fault current is way too lesser in magnitude, which might hinder the conventional operation of protective relays in the grid. However, there is significant promise in the proposed approach with the use of the potential energy function W_{25} in establishing new relaying principles based on its online monitoring. W_{25} is a synchronous machine independent metric and depends on pre-fault and post-fault wide area measurements, and the system topology. This would open a completely new spectrum for power systems protection based on transmission line energy function in modern VRE based inverter dominated power grids.

- **Automating weighting filter design in $\mathcal{H}_\infty$ control**: The robust control design proposed in the AC-Multi-terminal Direct Current (MTDC) grid in section 4.4, incorporates weighting

filters design to achieve the mixed sensitivity objectives. In the proposed scheme, the filters are designed based on frequency response of the sensitivity functions using singular value decomposition analysis techniques where the objective is to satisfy the upper and lower bounds of the maximum and minimum singular values of the sensitivity functions respectively. The filter design is tedious and has to be re-iterated and re-verified with the criteria until it has been met. It would be meaningful to automate this process by means of artificial neural networks where the weights can be trained using information of the sensitivities that are being addressed in the optimization sub-routines. This would significantly reduce the effort of manually tuning weights and make it a generic approach for any $\mathcal{H}_\infty$ control design in a hybrid system setting.

- **Modeling cyber physical processes in the robust control design** The designed controller demonstrates robust performance in the wake of communication latency of lower orders (≈ 100 ms) in the AC-MTDC test system. However, from a cyber security viewpoint, more realistic cyber-physical systems need to be modeled considering uncertainty-based approach. Similarly, other cyber physical aspects like feedback signal loss can be modeled as uncertainty and accounted for in an updated robust control design. These aspects need newer mathematical and control theoretical formulations which make it a very interesting topic for future studies. This kind of abstraction can also be leveraged in hybrid settings in the distribution test systems as well, where not much work has been done in uncertainty modeling for robust control design and applications. Human errors have been a concern for contingency scenarios and modeling such human errors in the control loop could be another aspect of cyber physical modeling that needs to be pondered upon.

REFERENCES

[1] P. H. J. Nardelli, N. Rubido, C. Wang, M. S. Baptista, C. Pomalaza-Raez, P. Cardieri, and M. Latva-aho, "Models for the modern power grid," *The European Physical Journal Special Topics*, vol. 223, no. 12, pp. 2423–2437, 2014.

[2] S. Massoud Amin and B. F. Wollenberg, "Toward a smart grid: power delivery for the 21st century," *IEEE Power and Energy Magazine*, vol. 3, no. 5, pp. 34–41, 2005.

[3] A. Rufer, "Today's and tomorrow's meaning of power electronics within the grid interconnection," in *2007 European Conference on Power Electronics and Applications*, 2007, pp. 1–11.

[4] R. Kinney, P. Crucitti, R. Albert, and V. Latora, "Modeling cascading failures in the north american power grid," *The European Physical Journal B - Condensed Matter and Complex Systems*, vol. 46, no. 1, pp. 101–107, 2005.

[5] S. Mei, Y. Ni, G. Wang, and S. Wu, "A study of self-organized criticality of power system under cascading failures based on ac-opf with voltage stability margin," *IEEE Transactions on Power Systems*, vol. 23, no. 4, pp. 1719–1726, 2008.

[6] U.S. Department of Energy,, "Blackout 2003, final report on the august 14, 2003 blackout in the united states and canada, causes and recommendations." [Online]. Available: https://www.energy.gov/sites/prod/files/oeprod/DocumentsandMedia/BlackoutFinal-Web.pdf

[7] J. De La Ree, Yilu Liu, L. Mili, A. G. Phadke, and L. DaSilva, "Catastrophic failures in power systems: Causes, analyses, and countermeasures," *Proceedings of the IEEE*, vol. 93, no. 5, pp. 956–964, 2005.

[8] M. Rohden, D. Jung, S. Tamrakar, and S. Kettemann, "Cascading failures in ac electricity grids," *Phys. Rev. E*, vol. 94, p. 032209, Sep 2016.

[9] R. Baldick, B. Chowdhury, I. Dobson, Zhaoyang Dong, Bei Gou, D. Hawkins, H. Huang, M. Joung, D. Kirschen, Fangxing Li, Juan Li, Zuyi Li, Chen-Ching Liu, L. Mili, S. Miller, R. Podmore, K. Schneider, Kai Sun, D. Wang, Zhigang Wu, Pei Zhang, Wenjie Zhang, and

Xiaoping Zhang, "Initial review of methods for cascading failure analysis in electric power transmission systems ieee pes cams task force on understanding, prediction, mitigation and restoration of cascading failures," in *2008 IEEE Power and Energy Society General Meeting - Conversion and Delivery of Electrical Energy in the 21st Century*, 2008, pp. 1–8.

[10] J. Song, E. Cotilla-Sanchez, G. Ghanavati, and P. D. H. Hines, "Dynamic modeling of cascading failure in power systems," *IEEE Transactions on Power Systems*, vol. 31, no. 3, pp. 2085–2095, 2016.

[11] B. Schäfer, D. Witthaut, M. Timme, and V. Latora, "Dynamically induced cascading failures in power grids," *Nature Communications*, vol. 9, no. 1, p. 1975, 2018.

[12] North American Electric Reliability Corporation, "Nerc operating manual, august 2016." [Online]. Available: https://www.nerc.com/comm/OC/Operating%20Manual%20DL/Operating_Manual_20160809.pdf

[13] IEEE GlobalSpec, Engineering 360, "Operating new york's electric grid part 1." [Online]. Available: https://insights.globalspec.com/article/4633/operating-new-york-s-electric-grid-part-1

[14] M. M. Adibi and N. Martins, "Impact of power system blackouts," in *2015 IEEE Power Energy Society General Meeting*, 2015, pp. 1–15.

[15] E. Mills and R. B. Jones, "An insurance perspective on u.s. electric grid disruption costs," *The Geneva Papers on Risk and Insurance - Issues and Practice*, vol. 41, no. 4, pp. 555–586, 2016.

[16] O. P. Veloza and F. Santamaria, "Analysis of major blackouts from 2003 to 2015: Classification of incidents and review of main causes," *The Electricity Journal*, vol. 29, no. 7, pp. 42 – 49, 2016.

[17] Eaton, Power Outage Annual Report, "Blackout tracker, united states annual report 2017." [Online]. Available: https://switchon.eaton.com/plug/blackout-tracker

[18] B. Li, J. Li, H. Li, W. He, X. Zeng, and C. Yu, "Analysis of turkish blackout on march 31, 2015 and lessons on china power grid," vol. 36, pp. 5788–5795, 11 2016.

[19] M. A. Kabir, M. M. H. Sajeeb, S. M. S. M. Chowdhury, and A. H. Chowdhury, "Analysis of real time frequency transients and inertia estimation of bangladesh power system," in *2015 18th International Conference on Computer and Information Technology (ICCIT)*, Dec 2015, pp. 116–121.

[20] G. Andersson, P. Donalek, R. Farmer, N. Hatziargyriou, I. Kamwa, P. Kundur, N. Martins, J. Paserba, P. Pourbeik, J. Sanchez-Gasca, R. Schulz, A. Stankovic, C. Taylor, and V. Vittal, "Causes of the 2003 major grid blackouts in north america and europe, and recommended means to improve system dynamic performance," *IEEE Transactions on Power Systems*, vol. 20, no. 4, pp. 1922–1928, Nov 2005.

[21] The Economic Times. 31 July 2012, "Power grids fail: Power restoration complete in delhi and northeast, 50Available: https://economictimes.indiatimes.com/industry/energy/power/power-grid-failure-ntpc-says-complete-restoration-possible-by-midnight/articleshow/15293178.cms

[22] Government of India, Ministry of Power, "Report of the enquiry committee on grid disturbance in northern region on 30th july 2012 and in northern, eastern and north-eastern region on 31st july 2012." [Online]. Available: https://powermin.nic.in/sites/default/files/uploads/GRID_ENQ_REP_16_8_12.pdf

[23] I. Dobson, B. A. Carreras, V. E. Lynch, and D. E. Newman, "An initial model fo complex dynamics in electric power system blackouts," in *Proceedings of the 34th Annual Hawaii International Conference on System Sciences*, Jan 2001, pp. 710–718.

[24] Z. Bao, Y. Cao, G. Wang, and L. Ding, "Analysis of cascading failure in electric grid based on power flow entropy," *Physics Letters A*, vol. 373, no. 34, pp. 3032 – 3040, 2009. [Online]. Available: http://www.sciencedirect.com/science/article/pii/S0375960109007610

[25] N. Amjady and S. F. Majedi, "Transient stability prediction by a hybrid intelligent system," *IEEE Transactions on Power Systems*, vol. 22, no. 3, pp. 1275–1283, Aug 2007.

[26] T. Amraee and S. Ranjbar, "Transient instability prediction using decision tree technique," *IEEE Transactions on Power Systems*, vol. 28, no. 3, pp. 3028–3037, Aug 2013.

[27] S. Shukla, A. Fung, and K. Raahemifar, "Transient stability optimization analysis for transmission systems generators to prevent cascade failure by coordinating contingency planning load-shedding in power transmission grid," in *2015 IEEE 28th Canadian Conference on Electrical and Computer Engineering (CCECE)*, May 2015, pp. 291–296.

[28] S. Poudel, Zhen Ni, T. M. Hansen, and R. Tonkoski, "Cascading failures and transient stability experiment analysis in power grid security," in *2016 IEEE Power Energy Society Innovative Smart Grid Technologies Conference (ISGT)*, Sep. 2016, pp. 1–5.

[29] M. Rahnamay-Naeini and M. M. Hayat, "Impacts of operating characteristics on sensitivity of power grids to cascading failures," in *2016 IEEE Power and Energy Society General Meeting (PESGM)*, July 2016, pp. 1–5.

[30] R. Kavasseri and S. K. Srinivasan, "Joint placement of phasor and power flow measurements for observability of power systems," *IEEE Transactions on Power Systems*, vol. 26, no. 4, pp. 1929–1936, Nov 2011.

[31] B. Gou and R. G. Kavasseri, "Unified pmu placement for observability and bad data detection in state estimation," *IEEE Transactions on Power Systems*, vol. 29, no. 6, pp. 2573–2580, Nov 2014.

[32] A. G. PHADKE and T. BI, "Phasor measurement units, wams, and their applications in protection and control of power systems," *Journal of Modern Power Systems and Clean Energy*, vol. 6, no. 4, pp. 619–629, 2018.

[33] R. G. Kavasseri, Y. Cui, and S. M. Brahma, "A new approach for event detection based on energy functions," in *PES General Meeting| Conference & Exposition, 2014 IEEE*. IEEE, 2014, pp. 1–5.

[34] L. F. C. Alberto and H. D. Chiang, "Towards development of generalized energy functions for electric power systems," in *2012 IEEE Power and Energy Society General Meeting*, July 2012, pp. 1–6.

[35] K. Padiyar, *Structure preserving energy functions in power systems: theory and applications*. CRC Press, 2016.

[36] P. Kundur, N. J. Balu, and M. G. Lauby, *Power system stability and control.* McGraw-hill New York, 1994, vol. 7.

[37] Northwest Power and Conservation Council., "1996 system disturbances report." [Online]. Available: https://www.nerc.com/pa/rrm/ea/System%20Disturbance%20Reports%20DL/ 1996SystemDisturbance.pdf

[38] Y. ALShamli, N. Hosseinzadeh, H. Yousef, and A. Al-Hinai, "A review of concepts in power system stability," in *2015 IEEE 8th GCC Conference Exhibition*, 2015, pp. 1–6.

[39] S. Poudel, Zhen Ni, T. M. Hansen, and R. Tonkoski, "Cascading failures and transient stability experiment analysis in power grid security," in *2016 IEEE Power and Energy Society Innovative Smart Grid Technologies Conference (ISGT)*, 2016, pp. 1–5.

[40] F. Shi, H. Zhang, and G. Xue, "Instability prediction of the inter connected power grids based on rotor angle measurement," *International Journal of Electrical Power and Energy Systems*, vol. 88, pp. 21 – 32, 2017.

[41] US Department of Energy, Office of Energy Efficiency and Renewable Energy,, "2018 offshore wind technologies market report." [Online]. Available: https://www.energy.gov/eere/wind/ downloads/2018-offshore-wind-market-report

[42] Office of Energy Efficiency and Renewable Energy,, "Windexchange, u.s. department of energy." [Online]. Available: https://windexchange.energy.gov/maps-data/321

[43] J. Arillaga, *AC-DC Power System Analysis*, ser. Energy Engineering. Institution of Engineering and Technology, 1998. [Online]. Available: https://digital-library.theiet.org/ content/books/po/pbpo027e

[44] N. R. Chaudhuri, B. Chaudhuri, R. Majumder, and A. Yazdani, "Multiterminal direct-current grids: Modeling, anlysis, and control." *Wiley-IEEE Press*, 2014.

[45] P. Rodriguez and K. Rouzbehi, "Multi-terminal dc grids: challenges and prospects," *Journal of Modern Power Systems and Clean Energy*, vol. 5, no. 4, pp. 515–523, 2017.

[46] M. Ndreko, A. Bucurenciu, M. Popov, and M. A. M. M. van der Meijden, "On grid code compliance of offshore mtdc grids: modeling and analysis," in *2015 IEEE Eindhoven PowerTech*, 2015, pp. 1–6.

[47] A. Sadu, G. K. Roy, F. Ponci, and A. Monti, "Methodology for reliability analysis of cyber-physical mtdc grids," *IEEE Journal of Emerging and Selected Topics in Power Electronics*, pp. 1–1, 2020.

[48] C. Gavriluta, C. Boudinet, F. Kupzog, A. Gomez-Exposito, and R. Caire, "Cyber-physical framework for emulating distributed control systems in smart grids," *International Journal of Electrical Power and Energy Systems*, vol. 114, p. 105375, 2020.

[49] S. Skogestad and I. Postlethwaite, "Multivariable feedback control." *Wiley, New York*, 2001.

[50] Y. P. Leong and J. C. Doyle, "Understanding robust control theory via stick balancing," in *2016 IEEE 55th Conference on Decision and Control (CDC)*, 2016, pp. 1508–1514.

[51] D. Wang, D. Liu, H. Li, B. Luo, and H. Ma, "An approximate optimal control approach for robust stabilization of a class of discrete-time nonlinear systems with uncertainties," *IEEE Transactions on Systems, Man, and Cybernetics: Systems*, vol. 46, no. 5, pp. 713–717, 2016.

[52] B. Pal and B. Chaudhuri, "Robust control in power systems." *Springer*, 2005.

[53] A. Banerjee, M. Maharjan, and R. G. Kavasseri, "Fault mapping in multi-machine power systems by principal component sensitivity-an energy function perspective," in *2018 North American Power Symposium (NAPS)*, Sep. 2018, pp. 1–6.

[54] P. N. Papadopoulos, J. V. Milanović, P. Bhui, and N. Senroy, "Fast online identification of power system dynamic behavior," in *2017 IEEE Power Energy Society General Meeting*, July 2017, pp. 1–5.

[55] P. Kundu and A. K. Pradhan, "Real-time event identification using synchrophasor data from selected buses," *IET Generation, Transmission Distribution*, vol. 12, no. 7, pp. 1664–1671, 2018.

[56] F. Gomez, A. Rajapakse, U. Annakkage, and I. Fernando, "Support vector machine-based algorithm for post-fault transient stability status prediction using synchronized measurements," in *2011 IEEE Power and Energy Society General Meeting*, July 2011, pp. 1–1.

[57] O. P. Dahal, S. M. Brahma, and H. Cao, "Comprehensive clustering of disturbance events recorded by phasor measurement units," *IEEE Transactions on Power Delivery*, vol. 29, no. 3, pp. 1390–1397, 2014.

[58] J. Ma, Y. V. Makarov, C. H. Miller, and T. B. Nguyen, "Use multi-dimensional ellipsoid to monitor dynamic behavior of power systems based on pmu measurement," in *Power and Energy Society General Meeting-conversion and Delivery of Electrical Energy in the 21st Century, 2008 IEEE.* IEEE, 2008, pp. 1–8.

[59] J. Yan, Y. Zhu, H. He, and Y. Sun, "Multi-contingency cascading analysis of smart grid based on self-organizing map," *IEEE Transactions on Information Forensics and Security*, vol. 8, no. 4, pp. 646–656, 2013.

[60] I. T. Jolliffe and J. Cadima, "Principal component analysis: a review and recent developments." *Philos Trans A Math Phys Eng Sci*, vol. 374, no. 2065, p. 20150202, Apr 2016.

[61] R. Zhang, J. Wu, L. Hao, M. Shao, B. Li, and Y. Lu, "Power system transient stability assessment based on principal component analysis," in *2018 2nd IEEE Conference on Energy Internet and Energy System Integration (EI2)*, Oct 2018, pp. 1–6.

[62] K. K. Anaparthi, B. Chaudhuri, N. F. Thornhill, and B. C. Pal, "Coherency identification in power systems through principal component analysis," *IEEE Transactions on Power Systems*, vol. 20, no. 3, pp. 1658–1660, Aug 2005.

[63] I. T. Jolliffe, "Principal component analysis and factor analysis," in *Principal component analysis.* Springer, 1986, pp. 115–128.

[64] R. B. Cattell, "The scree test for the number of factors," *Multivariate behavioral research*, vol. 1, no. 2, pp. 245–276, 1966.

[65] R. B. Cattell and S. Vogelmann, "A comprehensive trial of the scree and kg criteria for determining the number of factors," *Multivariate Behavioral Research*, vol. 12, no. 3, pp. 289–325, 1977.

[66] A. Shaw and S. Joseph, "Principal components analysis of maltby and day's (1998) amended quest religious orientation scale: a replication of the three component structure," *Personality and Individual Differences*, vol. 37, no. 7, pp. 1425 – 1430, 2004.

[67] M. T. John, D. R. Reissmann, L. Feuerstahler, N. Waller, K. Baba, P. Larsson, A. Čelebić, G. Szabo, and K. Rener-Sitar, "Exploratory factor analysis of the oral health impact profile," *Journal of Oral Rehabilitation*, vol. 41, no. 9, pp. 635–643, 2014.

[68] J. T. Townsend, "Theoretical analysis of an alphabetic confusion matrix," *Perception & Psychophysics*, vol. 9, no. 1, pp. 40–50, 1971.

[69] H. G. Lewis and M. Brown, "A generalized confusion matrix for assessing area estimates from remotely sensed data," *International Journal of Remote Sensing*, vol. 22, no. 16, pp. 3223–3235, 2001.

[70] A. HAY, "The derivation of global estimates from a confusion matrix," *International Journal of Remote Sensing*, vol. 9, no. 8, pp. 1395–1398, 1988.

[71] J. Parker, "Rank and response combination from confusion matrix data," *Information Fusion*, vol. 2, no. 2, pp. 113 – 120, 2001.

[72] L. Chen and H. L. Tang, "Improved computation of beliefs based on confusion matrix for combining multiple classifiers," *Electronics Letters*, vol. 40, no. 4, pp. 238–239, Feb 2004.

[73] C. B. Vilakazi and T. Marwala, "Bushing fault detection and diagnosis using extension neural network," in *2006 International Conference on Intelligent Engineering Systems*, June 2006, pp. 170–174.

[74] M. Amozegar and K. Khorasani, "An ensemble of dynamic neural network identifiers for fault detection and isolation of gas turbine engines," *Neural Networks*, vol. 76, pp. 106 – 121, 2016.

[75] S. D. J. McArthur, S. M. Strachan, and G. Jahn, "The design of a multi-agent transformer condition monitoring system," *IEEE Transactions on Power Systems*, vol. 19, no. 4, pp. 1845–1852, Nov 2004.

[76] R. Chedid, H. Akiki, and S. Rahman, "A decision support technique for the design of hybrid solar-wind power systems," *IEEE Transactions on Energy Conversion*, vol. 13, no. 1, pp. 76–83, 1998.

[77] *Matlab User's Guide.* The Mathworks Inc., USA, 2015.

[78] A. Banerjee, R. G. Kavasseri, M. B. Gani, and S. Brahma, "Towards supervisory protection using energy functions for relay misoperations in a stressed power system during blackout," in *2019 IEEE Milan PowerTech*, June 2019, pp. 1–6.

[79] S. H. Li, N. Yorino, and Y. Zoka, "Operation margin analysis of zone 3 impedance relay based on sensitivities to power injection," *IET Generation, Transmission Distribution*, vol. 1, no. 2, pp. 312–317, March 2007.

[80] S. Li, N. Yorino, M. Ding, and Y. Zoka, "Sensitivity analysis to operation margin of zone 3 impedance relays with bus power and shunt susceptance," *IEEE Transactions on Power Delivery*, vol. 23, no. 1, pp. 102–108, Jan 2008.

[81] B. Ravikumar, D. Thukaram, and H. P. Khincha, "An approach for distance relay co-ordination using support vector machines," *TENCON 2008 - 2008 IEEE Region 10 Conference*, pp. 1–6, 2008.

[82] B. Ravikumar, D. Thukaram, and H. P. Khincha, "An approach using support vector machines for distance relay coordination in transmission system," *IEEE Transactions on Power Delivery*, vol. 24, no. 1, pp. 79–88, Jan 2009.

[83] K. Seethalekshmi, S. N. Singh, and S. C. Srivastava, "A classification approach using support vector machines to prevent distance relay maloperation under power swing and voltage instability," *IEEE Transactions on Power Delivery*, vol. 27, no. 3, pp. 1124–1133, July 2012.

[84] M. R. Aghamohammadi, S. Hashemi, and A. Hasanzadeh, "A new approach for mitigating blackout risk by blocking minimum critical distance relays," *International Journal of*

Electrical Power and Energy Systems, vol. 75, pp. 162–172, 2016. [Online]. Available: http://www.sciencedirect.com/science/article/pii/S0142061515003567

[85] H. Song and M. Kezunovic, "A new analysis method for early detection and prevention of cascading events," *Electric Power Systems Research*, vol. 77, no. 8, pp. 1132 – 1142, 2007. [Online]. Available: http://www.sciencedirect.com/science/article/pii/S0378779606002343

[86] A. K. Singh and B. C. Pal, "Decentralized dynamic state estimation in power systems using unscented transformation," *IEEE Transactions on Power Systems*, vol. 29, no. 2, pp. 794–804, March 2014.

[87] G. Anagnostou and B. C. Pal, "Derivative-free kalman filtering based approaches to dynamic state estimation for power systems with unknown inputs," *IEEE Transactions on Power Systems*, vol. 33, no. 1, pp. 116–130, Jan 2018.

[88] M. B. Gani and S. M. Brahma, "Dynamic simulation of the arizona-southern california blackout to develop a wide area testbed," in *2018 North American Power Symposium (NAPS)*, Sep. 2018, pp. 1–6.

[89] North American Electric Reliability Council and Federal Energy Regulatory Commission, "Arizona - southern california outages on september 8, 2011: Causes and recommendations." [Online]. Available: https://www.ferc.gov/legal/staff-reports/04-27-2012-ferc-nerc-report.pdf

[90] Y. Cui and R. Kavasseri, "A particle filter for dynamic state estimation in multi-machine systems with detailed models," *IEEE Transactions on Power Systems*, vol. 30, no. 6, pp. 3377–3385, Nov 2015.

[91] S. Brahma, R. Kavasseri, H. Cao, N. R. Chaudhuri, T. Alexopoulos, and Y. Cui, "Real-time identification of dynamic events in power system using pmu data, and potential applications-models, promises and challanges," *IEEE transactions on Power Delivery*, vol. 32, no. 1, 2017.

[92] *North American Electric Reliability Corporation (NERC), NERC Report, Real-Time Application of Synchrophasors for Improving Reliability.* NERC, USA, 2010.

[93] A. Banerjee and N. R. Chaudhuri, "Robust damping of inter-area oscillations in ac-mtdc grids using h infinity mixed-sensitivity approach," in *2016 IEEE Power and Energy Society General Meeting (PESGM)*, July 2016, pp. 1–5.

[94] S. Cole, J. Beerten, and R. Belmans, "Generalized dynamic vsc mtdc model for power system stability studies," *IEEE Transactions on Power Systems*, vol. 25, no. 3, pp. 1655–1662, Aug 2010.

[95] N. R. Chaudhuri, R. Majumder, B. Chaudhuri, and J. Pan, "Stability analysis of vsc mtdc grids connected to multimachine ac systems," *IEEE Transactions on Power Delivery*, vol. 26, no. 4, pp. 2774–2784, Oct 2011.

[96] N. R. Chaudhuri and B. Chaudhuri, "Adaptive droop control for effective power sharing in multi-terminal dc (mtdc) grids," *IEEE Transactions on Power Systems*, vol. 28, no. 1, pp. 21–29, Feb 2013.

[97] E. Prieto-Araujo, F. D. Bianchi, A. Junyent-Ferre, and O. Gomis-Bellmunt, "Methodology for droop control dynamic analysis of multiterminal vsc-hvdc grids for offshore wind farms," *IEEE Transactions on Power Delivery*, vol. 26, no. 4, pp. 2476–2485, Oct 2011.

[98] R. Eriksson, J. Beerten, M. Ghandhari, and R. Belmans, "Optimizing dc voltage droop settings for ac/dc system interactions," *IEEE Transactions on Power Delivery*, vol. 29, no. 1, pp. 362–369, Feb 2014.

[99] R. Preece and J. V. Milanović, "Tuning of a damping controller for multiterminal vsc-hvdc grids using the probabilistic collocation method," *IEEE Transactions on Power Delivery*, vol. 29, no. 1, pp. 318–326, Feb 2014.

[100] R. Eriksson, "A new control structure for multiterminal dc grids to damp interarea oscillations," *IEEE Transactions on Power Delivery*, vol. 31, no. 3, pp. 990–998, June 2016.

[101] P. Gahinet and P. Apkarian, "A linear matrix inequality approach to h/sub /spl infin// control," *International Journal of Robust and Nonlinear Control*, vol. 4, no. 4, pp. 421–448, 1994.

[102] C. Scherer, P. Gahinet, and M. Chilali, "Multiobjective output-feedback control via lmi optimization," *IEEE Transactions on Automatic Control*, vol. 42, no. 7, pp. 896–911, July 1997.

[103] M. Chilali and P. Gahinet, "H/sub /spl infin// design with pole placement constraints: an lmi approach," *IEEE Transactions on Automatic Control*, vol. 41, no. 3, pp. 358–367, March 1996.

[104] B. Chaudhuri, B. C. Pal, A. C. Zolotas, I. M. Jaimoukha, and T. C. Green, "Mixed-sensitivity approach to h/sub /spl infin// control of power system oscillations employing multiple facts devices," *IEEE Transactions on Power Systems*, vol. 18, no. 3, pp. 1149–1156, Aug 2003.

[105] B. Chaudhuri and B. C. Pal, "Robust damping of multiple swing modes employing global stabilizing signals with a tcsc," *IEEE Transactions on Power Systems*, vol. 19, no. 1, pp. 499–506, Feb 2004.

[106] S. Ray, B. Chaudhuri, and R. Majumder, "Appropriate signal selection for damping multi-modal oscillations using low order controllers," in *2008 IEEE Power and Energy Society General Meeting - Conversion and Delivery of Electrical Energy in the 21st Century*, July 2008, pp. 1–7.

[107] A. Banerjee, N. R. Chaudhuri, and R. G. Kavasseri, "A novel explicit disturbance model-based robust damping of interarea oscillations through mtdc grids embedded in ac systems," *IEEE Transactions on Power Delivery*, vol. 33, no. 4, pp. 1864–1874, Aug 2018.

[108] P. Agnihotri, A. M. Kulkarni, A. M. Gole, B. A. Archer, and T. Weekes, "A robust wide-area measurement-based damping controller for networks with embedded multiterminal and multiinfeed hvdc links," *IEEE Transactions on Power Systems*, vol. 32, no. 5, pp. 3884–3892, Sep. 2017.

[109] A. McDonald and C. Clack, "Low cost and low carbon emission wind and solar energy systems are feasible for large geographic domains," *Sustainable Energy and Atmospheric Sciences Seminar*, NOAA, NREL, and CU-Boulder RASEI, May 2014. 2014.

[110] Y. Li and J. D. McCalley, "Design of a high capacity inter-regional transmission overlay for the u.s." *IEEE Transactions on Power Systems*, vol. 30, no. 1, pp. 513–521, Jan 2015.

[111] L. Harnefors, N. Johansson, L. Zhang, and B. Berggren, "Interarea oscillation damping using active-power modulation of multiterminal hvdc transmissions," *IEEE Transactions on Power Systems*, vol. 29, no. 5, pp. 2529–2538, Sep. 2014.

[112] "The math works inc." *Matlab Users Guide*, 2015.

[113] Y. Cao, "Control structure selection for chemical processes using input-output controllability analysis," *PhD thesis, University of Exeter*, 1995.

[114] N. Lehtomaki, D. Castanon, B. Levy, G. Stein, N. Sandell, and M. Athans, "Robustness and modeling error characterization," *IEEE Transactions on Automatic Control*, vol. 29, no. 3, pp. 212–220, March 1984.

APPENDIX

A.1. WAMS Based Measurements

The equations for constructing the SPEFs for the test system mentioned in chapter 2 can be summarized below. The load at bus i is represented in (A.1), (A.2), (A.3) as follows:

$$P_L^i = f_{pi}(V_i) = a_{0i} + a_{1i}V_i + a_{2i}V_i^2, \quad Q_L^i = f_{qi}(V_i) = b_{0i} + b_{1i}V_i + b_{2i}V_i^2 \tag{A.1}$$

where V_i is the voltage magnitude at bus i. The contribution of the load components (active, reactive) to the energy function is then given by:

$$W_{22}(t) = \sum_{i=1}^{N} \int_{t_0}^{t} f_{pi}(V_i)\frac{d\phi_i}{dt}dt \tag{A.2}$$

$$W_{23}(V) = \sum_{i=1}^{N} \int_{V_{i0}}^{V_i} \frac{f_{qi}(\sigma_i)}{\sigma_i}d\sigma_i \tag{A.3}$$

The relative change in magnetic energies stored in the transmission lines is captured by the component W_{25} as shown in (A.4):

$$W_{25} = -\tfrac{1}{2}\sum_{i=1}^{N}\sum_{j=1}^{N} B_{ij}\left(V_i V_j \cos(\phi_{ij}) - V_{i0}V_{j0}\cos(\phi_{ij0})\right) \tag{A.4}$$

The energy contributions from a generator arise from the magnetic energies stored in the machine reactance, damper windings on the d and d axes and the field circuit (with AVR) and can be represented as W_{21}, in (A.5)

$$W_{21}(y) = -\sum_{i=1}^{M} \int_{t_0}^{t} P_{mi}(t)\frac{d\theta_i}{dt}dt \tag{A.5}$$

All the remaining energy functions in a multi-machine power system setting can be calculated using the formulae depicted in (A.6) - (A.12).

$$W_{24}(x,y) = \sum_{i=1}^{M} [f_{24}^i - f_{24,0}^i],$$

$$f_{24}^i = E_{qi}'^2 + V_i^2 - 2E_{qi}'V_i\cos(\theta_i - \phi) \tag{A.6}$$

$$W_{26}(y) = \sum_{i=1}^{M} [f_{26}^i - f_{26,0}^i],$$

$$f_{26}^i = [V_i^2(\cos 2(\theta_i - \phi) - 1)]\frac{x_{di}' - x_{qi}'}{4x_{qi}'x_{di}'} \tag{A.7}$$

$$W_{27}(x,y) = \sum_{i=1}^{M} [f_{27}^i - f_{27,0}^i],$$

$$f_{27}^i = [E_{di}'^2 + V_i^2 + 2E_{di}'V_i\sin(\theta_i - \phi)]\frac{1}{x_{qi}'} \tag{A.8}$$

$$W_{28}(y) = -\sum_{i=1}^{M} \frac{V_i^2 - V_{i0}^2}{2x_{qi}'} \tag{A.9}$$

$$W_{29}(y) = -\sum_{i=1}^{M} \int_{t_0}^{t} [\frac{E_{fdi}}{x_{di} - x_{di}'}]\frac{dE_{qi}'}{dt}dt \tag{A.10}$$

$$W_{210}(y) = \sum_{i=1}^{M} \frac{E_{qi}'^2 - E_{qi0}'^2}{2(x_{di} - x_{di}')} \tag{A.11}$$

$$W_{211}(y) = \sum_{i=1}^{M} \frac{E_{di}'^2 - E_{di0}'^2}{2(x_{qi} - x_{qi}')} \tag{A.12}$$

A.2. State-Space Form of Controller

The state-space representation of the controller designed in Chapter 4 is shown below in (A.13), (A.14), (A.15) and (A.16).

$$
A = \begin{bmatrix}
-4.89 & 0.00 & -0.68 & 0.22 & 0.10 & 0.48 & 0.31 & -0.67 & -3.77 & 2.49 & 10.09 & -15.15 & 3.76 & -32.02 & 95.21 \\
0.30 & -5.23 & 0.41 & 0.88 & -0.16 & -0.44 & 0.20 & 0.23 & 0.93 & 3.33 & 6.73 & 3.63 & 14.44 & 14.79 & 16.47 \\
-0.04 & 0.38 & -1.43 & 0.40 & 0.00 & 0.29 & -0.02 & -0.05 & -0.13 & -0.26 & -0.46 & -0.51 & -1.20 & -1.70 & -0.18 \\
0.49 & -0.06 & -7.00 & -0.40 & 0.46 & 2.85 & -0.05 & -0.08 & 0.34 & -0.82 & -2.33 & 1.56 & -2.56 & 2.30 & -15.34 \\
0.49 & -0.06 & -7.00 & -0.40 & 0.46 & 2.85 & -0.05 & -0.08 & 0.34 & -0.82 & -2.33 & 1.56 & -2.56 & 2.30 & -15.34 \\
-0.11 & -0.58 & -2.17 & -2.08 & 0.40 & -0.23 & 0.04 & 0.00 & 0.09 & 0.01 & -0.08 & 0.45 & 0.21 & 1.12 & -2.03 \\
0.61 & 0.10 & -1.21 & 0.40 & -0.52 & 0.42 & -0.22 & 0.14 & 0.95 & -0.90 & -3.17 & 3.88 & -1.86 & 7.75 & -26.68 \\
0.60 & 1.43 & 6.44 & 7.57 & -1.33 & -2.29 & -0.12 & -0.08 & -0.32 & 0.53 & 1.63 & -1.73 & 1.34 & -3.26 & 13.23 \\
-0.83 & -0.46 & -4.45 & 0.61 & 0.21 & 1.98 & 0.21 & -0.54 & -2.75 & 2.34 & 8.34 & -10.68 & 4.41 & -21.66 & 71.79 \\
0.35 & 0.33 & 1.37 & 1.25 & -0.24 & -0.43 & -0.08 & -0.04 & -0.13 & -1.35 & -1.61 & -0.22 & -2.32 & 2.69 & -10.34 \\
0.28 & 0.37 & 1.58 & 2.04 & -0.38 & -0.41 & -0.06 & -0.17 & -0.46 & -1.30 & -0.80 & -1.33 & -5.35 & 3.21 & -9.18 \\
-0.07 & 0.05 & 0.47 & -0.52 & 0.05 & -0.23 & -0.08 & 0.08 & 0.46 & 1.91 & -0.10 & -0.04 & 0.14 & -0.19 & -2.30 \\
0.20 & 0.23 & -0.05 & 0.17 & -0.02 & 0.07 & -0.02 & -0.07 & -0.14 & 0.54 & 2.45 & -0.70 & -2.75 & 0.32 & -4.64 \\
0.34 & 1.23 & 4.52 & 4.89 & -0.88 & -1.28 & -0.09 & 0.01 & 0.26 & -2.00 & -5.29 & 1.12 & 1.66 & -8.97 & 16.19 \\
1.20 & 0.06 & 0.44 & 0.90 & -0.17 & -0.12 & -0.02 & 0.07 & 0.32 & -1.33 & -0.09 & 3.40 & -3.52 & 4.35 & -37.21
\end{bmatrix}
\quad\text{(A.13)}
$$

$$
B = \begin{bmatrix}
0.06 & -0.01 \\
0.01 & -0.02 \\
1.06 & 0.03 \\
-0.18 & -0.38 \\
0.29 & -2.42 \\
2.18 & 0.55 \\
-0.62 & 2.07 \\
-8.36 & -1.74 \\
-0.77 & 8.53 \\
-1.40 & -0.81 \\
-2.28 & -0.21 \\
0.61 & -1.49 \\
-0.23 & 0.26 \\
-5.42 & -1.82 \\
-1.09 & 0.50
\end{bmatrix}
\quad\text{(A.14)}
$$

$$
C = \begin{bmatrix}
78.204 & -42.174 & 0.754 & -0.232 & 0.026 & -0.029 & -0.010 & -0.000 & -0.003 & 0.001 & 0.011 & -0.030 & -0.007 & -0.071 & 0.153 \\
48.044 & 68.150 & -0.924 & -1.528 & 0.151 & 0.006 & -0.010 & 0.001 & 0.001 & 0.007 & 0.021 & -0.011 & 0.026 & -0.012 & 0.129
\end{bmatrix}
\quad\text{(A.15)}
$$

$$D = \begin{bmatrix} 0 & 0 \\ 0 & 0 \end{bmatrix} \tag{A.16}$$

A.3. Modal Analysis

Modal analysis is used to identify the important local modes and inter-area modes in the system by the method of eigenvalue analysis. Inter-area oscillation modes in large interconnected power systems are usually observed in frequencies ranging from 0.1 Hz to 0.8 Hz. Eigenvalues (λ) can be represented as a complex conjugate pair where the real part (σ) refers to damping (ς) and the imaginary part (ω) relates to frequency of oscillation (f) of the modes as shown in (A.17)

$$\lambda_{1,2} = \sigma \pm j\omega$$
$$f = \frac{\omega}{2\pi} \tag{A.17}$$
$$\varsigma = -\frac{\sigma}{\sqrt{\sigma^2 + \omega^2}}$$

In order to obtain the proposed objectives a MIMO controller controller has been designed. MIMO controllers provide more knowledge on the interactions than SISO controllers and have more significant directions that need to be identified in a control design problem. The linear state space model can be represented as (A.18)

$$\dot{X} = AX + BU$$
$$Y = CX + DU \tag{A.18}$$

Modal Controllabity and Observability indices were performed on the linearized model, refer Table A.1 and Table A.2 , where all the calculated indices have been calculated and normalized as shown in (A.19). The state-space form in (A.18) can be represented as a transfer function in (A.19) which is subject to manipulations where V and W represents the right and left eigenvectors respec-

tively.

$$G_r(s) = C(sI - A)^{-1}B$$

$$= CVW(sI - A)^{-1}VWB$$

$$= CV\left[V^{-1}(sI - A)W^{-1}\right]^{-1}WB$$

$$= CV(sI - A)^{-1}WB \qquad\qquad (A.19)$$

$$= \sum_{i=1}^{i=n} \frac{Cv_i w_i B}{s - \lambda_i}$$

$$= \sum_{i=1}^{i=n} \frac{R_i}{s - \lambda_i}$$

For the test system in chapter 5, the choice of feedback signal was determined from the 89 outputs of the system, which are some linear combination of the states, for both the inter-area modes of interest. Real power flowing through lines connecting buses 13 and 17 (i.e. P_{13-17}) and buses 17 and 53 (i.e. P_{27-53}), respectively, see Fig. 5.8, were chosen as the feedback signals. Table A.2 shows that P_{27-53} and P_{13-17} have the maximum observability across inter-area modes 1 and 2 respectively. The input signals were the converter station positive and negative poles, where converter stations #1 and #3, both positive and negative poles ($\#1, 3$ and $\#5, 7$), respectively, were chosen as the actuators having the highest weight in the relative controllability index, see Table A.1. The resulting plant used for the MIMO control design is hence a four input, two output plant.

Table A.1. Modal Controlabillity indices for the two inter-area modes of interest for test system in Chapter 5

MODAL CONTROLLABILITY			
Mode 1 (0.201 Hz)		Mode 2 (0.475 Hz)	
i/p signals	norm. cont	i/p signals	norm. cont
5	1	7	1
1	1	3	1
6	0.983	8	0.957
2	0.983	4	0.957

An additional contraint θ_{min} to place all poles on the left half of the s-plane within a conic sector was considered to ensure the desired closed-loop damping ratio. The damping ratio (ζ) with respect to the conic sector can be represented as, $\zeta_{min} = cos(\dfrac{\theta_{min}}{2})$. Figure A.1 depicts the

Table A.2. Modal Observability indices for the two inter-area modes of interest test system in Chapter 5

MODAL OBSERVABILITY			
Mode 1 (0.201 Hz)		**Mode 2 (0.475 Hz)**	
o/p signals	*norm. obsv*	*o/p signals*	*norm. obsv*
83 (P$_{27\text{-}53}$)	1	13 (P$_{13\text{-}17}$)	1
28	0.626	85	0.803
45	0.482	51	0.545
33	0.478	14	0.528

conic sector within which alll the closed loop poles placement has to be attained setting it up as a constraint in the H_∞ optimization routine. In Chapter 5, a damping ratio of $\zeta_{min} = 6.5\%$ was considered for the explicitly modeled disturbance rejection design in the LMI framework and was compared with a standard H_∞ design with $\zeta_{min} = 15\%$.
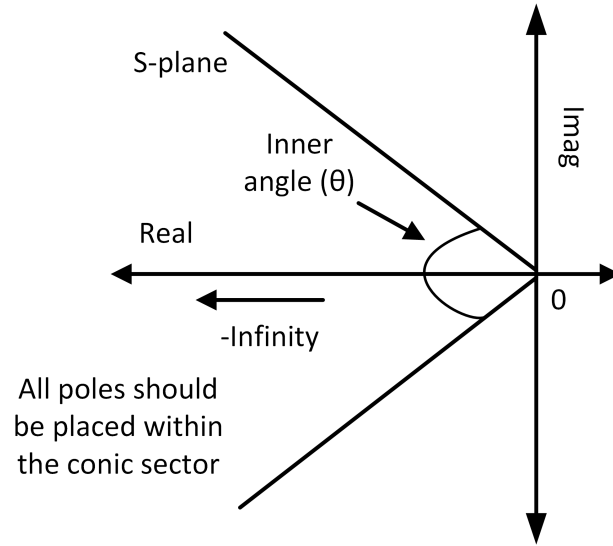

Figure A.1. Conic sector for pole placement constraint